Department of Experimental Physics
Faculty of Science
Palacký University Olomouc

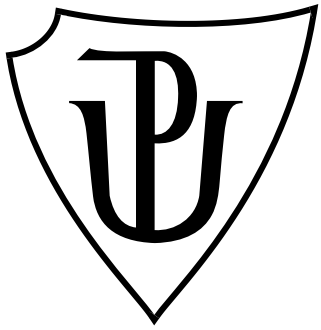

Doctoral thesis

Nuclear resonant methods applied to inhomogeneous systems with texture

Author	Vlastimil Vrba
Supervisor	prof. RNDr. Miroslav Mašláň, CSc.
Study field	Applied Physics
Study form	full-time
Year	2019

Bibliographic identification

Author	Vlastimil Vrba
Title	Nuclear resonant methods applied to inhomogeneous systems with texture
Type of thesis	doctoral thesis
Department	Department of Experimental Physics
Supervisor	prof. RNDr. Miroslav Mašláň, CSc.
Advisor	Mgr. Vít Procházka, Ph.D.
Year	2019
Number of pages	84
Supplements	1 CD/DVD
Language	English
Keywords	NRS; hyperfine interactions; nuclear forward scattering; Mössbauer spectroscopy; rotational invariance; texture

Bibliografická identifikace

Autor	Vlastimil Vrba
Název práce	Jaderné rezonanční metody aplikované na nehomogenní systémy s texturou
Typ práce	dizertační práce
Pracoviště	Katedra experimentální fyziky
Vedoucí práce	prof. RNDr. Miroslav Mašláň, CSc.
Konzultant	Mgr. Vít Procházka, Ph.D.
Rok	2019
Počet stran	84
Přílohy	1 CD/DVD
Jazyk práce	anglický
Klíčová slova	NRS; hyperjemné interakce; jaderný dopředný rozptyl; Mössbauerova spektroskopie; rotační invariance; textura

Abstract

The experimental techniques based on the nuclear resonant scattering provide a unique information on solid systems via modified energy levels of nuclei caused by their hyperfine interactions. Namely, the coherent elastic nuclear resonant scattering in the forward direction can be experimentally realized either in the energy domain as a transmission Mössbauer spectroscopy or in the time domain as a nuclear forward scattering of synchrotron radiation. Despite finding many applications in various research fields, the potential of these methods has not been fully explored. The aim of this work is to provide a theoretical description of the nuclear resonant scattering applied to complex materials exhibiting spatial inhomogeneities of hyperfine interactions along the direction of the incident radiation. Such situation has been observed, for example, in iron-based metallic glasses which have been subject to special treatment. The thickness effects, polarization mixing and preferential orientations of present hyperfine fields (i.e. texture) play a crucial role in the scattering process, so a general theoretical formalism is required for a proper description and interpretation of measured data. A significant part of the work is also devoted to the texture description for thick samples measured in both the energy and the time domain. The theory was successfully applied for the analysis and interpretation of nuclear forward scattering experiments conducted on $Fe_{81}Mo_8Cu_1B_{10}$ metallic glass during the crystallization process. The work also includes a description of the developed software package.

Abstrakt

Experimentální techniky založené na jevu jaderného rezonančního rozptylu poskytují informace o pevných látkách prostřednictvím modifikovaných energetických hladin jader v důsledku hyperjemných interakcí. Koherentní elastický jaderný rezonanční rozptyl v dopředném směru může být experimentálně realizován v energetické doméně jako transmisní Mössbauerova spektroskopie nebo v časové doméně jako jaderný dopředný rozptyl synchrotronového záření. Přestože tyto metody nalézají mnohá využití v rozličných výzkumných odvětvích, jejich potenciál doposud nebyl plně využit. Cílem této práce je teoreticky popsat jaderný rezonanční rozptyl na materiálech vykazujících nehomogenní rozložení hyperjemných interakcí ve směru dopadajícího záření. Takový případ byl pozorován například u speciálně upravených železo-obsahujících kovových skel. Zásadní vliv na rozptyl má v tomto případě tloušťka vzorku, změny v polarizaci záření a preferenční orientace přítomných hyperjemných polí (textura). Pro správný popis a interpretaci naměřených dat je pak potřeba použít obecný teoretický formalismus zahrnující uvedené jevy. Významná část práce je vyhrazena právě popisu textury v tlustých vzorcích pro měření v energetické i časové doméně. Popsaná teorie byla úspěšně použita k interpretaci experimentů jaderného dopředného rozptylu provedených na kovovém skle o složení $Fe_{81}Mo_8Cu_1B_{10}$ v průběhu krystalizace. Součástí práce je také popis vyvíjeného softwaru.

I declare that I have written this thesis by myself using the cited sources and that the thesis has not been submitted, in whole or in part, in any previous application for an academic degree.

In Olomouc, ...
signature

I would like to thank my supervisor Miroslav Mašláň for his guidance. Many thanks belong to my advisor Vít Procházka for providing inspiring advices and encouraging my research over the years. I also thank all my colleagues for their help and valuable discussions.

I especially want to thank my family and my girlfriend. This work could not be completed without their immense support and patience.

Lastly, I acknowledge the financial support by internal IGA grant of Palacký University (IGA_PrF_2019_002).

Contents

Introduction

Nuclear resonant methods utilize an interaction of the electromagnetic radiation with atomic nuclei in a solid. The nuclei serve as a probe to explore their local surroundings and offer information on the structural and magnetic ordering, electron configurations of atoms, etc. This information is coded in the nuclei energy levels, which are modified by so called hyperfine interactions between the nuclei and their surroundings.

If the energy of the incident photons is in resonance with the energy corresponding to a transition between the nuclei energy levels, the photons can be absorbed and subsequently reemitted. In a special case the directions of the incident and the emitted photons are the same, i.e. the nuclear resonant scattering proceeds in the forward direction. Experiments of the nuclear resonant forward scattering can be conducted either in energy domain as a transmission (absorption) spectroscopy or in time domain, where the intensity of the reemitted radiation is detected as a function of a time delay after its absorption. The former is realized as the Mössbauer spectroscopy method, which uses a radioactive material as a source of the incident radiation. The latter utilizes a synchrotron radiation source and is referred to as the nuclear forward scattering.

Both experimental techniques provide a unique insight into the local electric and magnetic properties in a solid state. However, the crucial part of nuclear resonant measurements is the evaluation of the experimental data, which is generally not an easy task. It is based on a comparison of the measured data with theoretical curves, that can be based on rather complex models of the studied samples. During the long-term existence of the nuclear resonant methods a universally applicable and automatic data evaluation procedure has not yet been invented.

It is important to continuously improve the data analysis as novel (often very complex) materials are being invented and more detailed information on studied samples is required to further improve their properties and performance. For example, iron-based metallic glasses exposed to an ion irradiation have recently been studied for their potential applications in accelerator devices. In addition to relatively complex hyperfine interactions, these materials may comprise spatially inhomogeneous regions, i.e. different hyperfine interactions in different parts of the system.

The interaction of photons with a scattering system exhibiting inhomogeneities along the direction of the incident radiation may result in interesting phenomena, arising from thickness effects, polarization changes and directional preferences of hyperfine interactions referred to as texture. Therefore, to explore the inhomogeneities by the nuclear resonant methods, a general scattering formalism must be utilized for a proper analysis and interpretation of the measurements.

The aim of this thesis is to theoretically describe the nuclear resonant scattering in the forward direction for materials with the spatial inhomogeneities of their hyperfine interactions. This work focuses on the nuclear resonance of ^{57}Fe nuclide. The description includes the analysis of the scattering effects that occur as a result of the inhomogeneities. Namely, a rotational invariance of the scattering and its relation to the inhomogeneities are studied. From a practical point of view, information on the spatial distributions of hyperfine interactions can be obtained from an experimentally observable violation of the rotational invariance. The described theory based on the model of a multilayered scattering system is applied to nuclear forward scattering experiments which were conducted on $Fe_{81}Mo_8Cu_1B_{10}$ metallic glass exposed to an irradiation by nitrogen ions. The differen-

ces between the measured data obtained under different geometrical arrangements of the sample allowed to identify the magnetic origin of the inhomogeneities.

The theoretically described and experimentally observed phenomena are strongly connected to the texture. The Mössbauer samples exhibiting a preferential orientation of local electric or magnetic fields have been described in detail for the case of Mössbauer spectroscopy applied to very thin samples, so the thickness effects can be negligible. However, the thickness effects play a significant role in the inhomogeneities identification using the nuclear resonant methods. This work introduces a generalized texture description for both Mössbauer spectroscopy and nuclear forward scattering. It is based on the approach conventionally used in the Mössbauer spectroscopy, which uses spherical harmonics as an orthogonal basis for the directional distributions of electric or magnetic fields. This allows a relatively simple implementation of the texture into calculations of data in energy and time domains. In addition, the results obtained under different considerations regarding the sample thickness and the used experimental technique are directly compared.

Due to new demands on the data evaluation in the nuclear resonant methods a new software package has been developed. Currently, the developed software calculates the energy and time domain data for materials containing ^{57}Fe. It allows the computations for the homogeneous systems as well as for the multilayers, simulating the inhomogeneous systems.

The thesis is divided into four chapters. The first chapter provides an introduction into the nuclear resonant scattering and its utilization in the transmission Mössbauer spectroscopy and nuclear forward scattering methods. The second chapter contains the theoretical description of the scattering on inhomogeneous systems and its relation to the rotational invariance of the scattering and its violation. The analysis and interpretation of the conducted experiments is also included in this chapter. The third chapter describes the texture and its effects in the nuclear resonant scattering. The fourth chapter presents the developed software package.

1 Nuclear Resonant Methods

The experimental techniques based on the resonant absorption and emission of photons by atomic nuclei started to be developed very soon after the discovery of the Mössbauer effect [1]. Today, these techniques find a wide range of applications across many scientific fields [2–5]. One of the main advantages is the possibility to inspect the hyperfine splitting of nuclei energy levels in a solid. The splitting is characteristic for a given surrounding of nuclei and allows to study the interactions of the surrounding with the nuclear system. Thus, the information on the atomic valence and spin states, local structural arrangements and magnetic ordering within the studied systems can be obtained [6].

This chapter provides a basic theoretical description of the nuclear resonance in a solid state. It focuses mainly on two similar experimental techniqes, transmission Mössbauer spectroscopy (TMS) and nuclear forward scattering (NFS). A utilization of the theory to describe the experimental data in both the energy domain (TMS) and the time domain (NFS) is shown. The techniques are also mutually compared, regarding the corresponding experimental arrangements, used radiation sources and data evaluation procedures.

1.1 Hyperfine Interactions

The interactions of a nuclear system with its surroundings depend on the properties of given nuclei and on the local fields acting on the nuclei. In the following part the physical quantities that describe both the nuclei and their surroundings are introduced. These quantities can be used as parameters describing the hyperfine splitting of the nuclei energy levels. Assuming the nuclei properties are known by selecting a particular nuclide the information on the energy levels is directly related to the studied surroundings described by corresponding hyperfine parameters. As the main field of interest of this work is the resonance of ^{57}Fe the theory will be demonstrated using this particular nuclide.

1.1.1 Nuclear System

A single nucleus can be treated as a quantum mechanical system of Z_n protons and N_n neutrons with a total angular momentum described by the j and m quantum numbers according to the eigenvalue equations [7, 8]

$$\hat{J}_z \left|j,m\right\rangle = m\hbar \left|j,m\right\rangle , \tag{1.1}$$

$$\hat{J}^2 \left|j,m\right\rangle = j(j+1)\hbar^2 \left|j,m\right\rangle , \tag{1.2}$$

where $\hbar = 1.055 \cdot 10^{-34}\,\mathrm{J\cdot s}$ is the reduced Planck's constant. The operator $\hat{J}_z$ is the projection of the angular momentum into the quantization z-axis and $\hat{J}$ is the angular momentum magnitude. The quantum numbers j, m can take the values of $j = 0, \frac{1}{2}, 1, \frac{3}{2}, \ldots$ and $m = -j, -j+1, \ldots, j-1, j$.

Nuclei with a non-zero angular momentum in their ground state will be further considered. Such nuclei also have a magnetic dipole moment, where [9]

$$\hat{\mu}_z \left|j,m\right\rangle = \gamma_\mathrm{G}\, m\hbar \left|j,m\right\rangle , \tag{1.3}$$

$$\hat{\mu}^2 \left|j,m\right\rangle = \gamma_\mathrm{G}^2\, j(j+1)\hbar^2 \left|j,m\right\rangle . \tag{1.4}$$

The operators $\hat{\mu}_z$ and $\hat{\mu}$ are the z-axis component and the magnitude of the magnetic dipole moment, respectively. The gyromagnetic ratio γ_G, which relates the magnetic dipole moment to the angular momentum, can also be expressed using the nuclear magneton μ_N and the g-factor of a nucleus as

$$\gamma_\mathrm{G} = \frac{g\mu_\mathrm{N}}{\hbar}\,. \tag{1.5}$$

The electric properties of a nucleus can be described by its total electric charge q_n and electric quadrupole moment[1] [10]. The electric charge is given by the number of protons forming the nucleus

$$q_\mathrm{n} = Z_\mathrm{n} q_0, \tag{1.6}$$

where $q_0 = 1.602 \cdot 10^{-19}\,\mathrm{C}$ is the elementary electric charge. The electric quadrupole moment gives a deviation of the nuclear electric charge distribution from the spherical symmetry. It is a 2nd-order tensor generally described by five independent values. Similarly to the magnetic dipole moment, the quadrupole moment is related to the nuclear angular momentum. If $j < 1$ it is equal to zero. For $j \geq 1$ the nucleus exhibits an axially symmetric charge distribution with respect to the quantization z-axis. Therefore, in the coordinate system coinciding with the tensor main axes, the quadrupole moment can be described by a single value. This value can be assigned to the eigenvalue of the $\hat{Q}_{zz}$ (diagonal tensor element) operator according to the formula

$$\hat{Q}_{zz}\,|j,m\rangle = \frac{3m^2 - j(j+1)}{j(2j-1)}\,q_0 Q\,|j,m\rangle\,. \tag{1.7}$$

For given j and m values the quantity Q fully defines the quadrupole moment.

For a nucleus in an excited quantum state the electric and magnetic properties may be different from those in its ground state. For example, the nuclide of ^{57}Fe has a ground state described by the quantum number $j_\mathrm{g} = 1/2$ and so its electric quadrupole moment is zero. In the first excited state the nuclide has the quantum number $j_\mathrm{e} = 3/2$ and exhibits a non-zero quadrupole moment. A list of parameters describing the ground and the first excited state of ^{57}Fe is shown in Table 1.1.

^{57}Fe	j	g	$\gamma_\mathrm{G}\,[\mathrm{rad}\cdot\mathrm{s}^{-1}\cdot\mathrm{T}^{-1}]$	$Q\,[\mathrm{barn}]$
ground state	1/2	0.1812	$8.675 \cdot 10^6$	0
1st excited state	3/2	−0.1035	$-4.955 \cdot 10^6$	0.16

Table 1.1: Values of g-factor, gyromagnetic ratio and electric quadrupole moment corresponding to the ground and the first excited state of ^{57}Fe. The quadrupole moment and g-factor values were taken/calculated from [11]. The gyromagnetic ratios were calculated using formula (1.5).

1.1.2 Interaction Hamiltonian

The real solid state samples are many-body systems of mutually interacting nuclei and electrons. The following description focuses on the nuclear system and introduces the interaction Hamiltonian, from which the nuclei energy levels in a solid could be obtained. For the sake of simplicity the time dependences of the interactions and the related relaxation

[1] The electric dipole moment of a nucleus is equal to zero, which results from a definite parity of the nuclear quantum state. The electric multipole terms which are of higher order than the quadrupole moment are usually neglected.

phenomena will be neglected [2, 12, 13]. The interactions can be described by the effective magnetic and electric fields interacting with the nuclear magnetic dipole moment, electric charge and electric quadrupole moment. The individual contributions to the interaction Hamiltonian will be now discussed in more detail.

The magnetic interaction Hamiltonian $\hat{H}_{\mathrm{M}}$ can be written as

$$\hat{H}_{\mathrm{M}} = -\hat{\vec{\mu}} \cdot \vec{B} = -\hat{\mu}_x B_x - \hat{\mu}_y B_y - \hat{\mu}_z B_z, \tag{1.8}$$

where $\vec{B}$ is the effective magnetic field. The Hamiltonian $\hat{H}_{\mathrm{M}}$ includes the interactions of the magnetic dipole moment with the orbital and spin angular momenta of the electrons around a nucleus, interactions with other electrons and nuclei in the solid and also the interaction with an external magnetic field. The former plays a dominant role in magnetic materials and the corresponding magnetic field contribution is referred to as the hyperfine magnetic field $\vec{B}^{\mathrm{hf}}$. A detailed description of the individual contributions to the effective magnetic field can be found in [14].

Using the properties of the angular momentum operators, the magnetic interaction Hamiltonian can be expressed in the $\{|j, m\rangle\}$ basis for individual values of j [7]. For the ground and the first excited state of ^{57}Fe the corresponding Hamiltonians are given as [15]

$$\hat{H}_{\mathrm{M,g}} = -\frac{1}{2}\,\gamma_{\mathrm{G,g}}\,\hbar B \begin{pmatrix} \cos\theta & e^{-i\phi}\sin\theta \\ e^{i\phi}\sin\theta & -\cos\theta \end{pmatrix}, \tag{1.9}$$

$$\hat{H}_{\mathrm{M,e}} = -\frac{3}{2}\,\gamma_{\mathrm{G,e}}\,\hbar B \begin{pmatrix} \cos\theta & \frac{\sqrt{3}}{3}e^{-i\phi}\sin\theta & 0 & 0 \\ \frac{\sqrt{3}}{3}e^{i\phi}\sin\theta & \frac{1}{3}\cos\theta & \frac{2}{3}e^{-i\phi}\sin\theta & 0 \\ 0 & \frac{2}{3}e^{i\phi}\sin\theta & -\frac{1}{3}\cos\theta & \frac{\sqrt{3}}{3}e^{-i\phi}\sin\theta \\ 0 & 0 & \frac{\sqrt{3}}{3}e^{i\phi}\sin\theta & -\cos\theta \end{pmatrix}. \tag{1.10}$$

The magnetic field is expressed in a spherical basis by its magnitude B, polar angle θ and azimuth angle ϕ (Fig. 1.1). The Hamiltonians are diagonal only if the field is oriented in the direction of the quantization z-axis, i.e. $\theta = 0$.

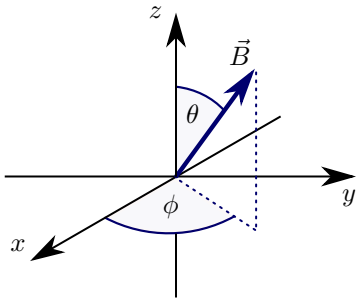

Figure 1.1: The effective magnetic field $\vec{B}$ in the laboratory reference frame.

The electric interactions can be obtained from basic considerations of a classical energy of an electrically charged system in the effective electric field, which is described by a scalar potential $\varphi(\vec{r})$ [16]. Using the multipole expansion of $\varphi(\vec{r})$ three main contributions can be distinguished. The first contribution gives the electrostatic energy of a point charge q_{n} at the position of a nucleus $E_0 = \varphi(0)q_{\mathrm{n}}$. This energy is the same for all nuclei quantum

states and is usually omitted as it does not affect the energy transitions within the nuclear system. The second contribution depends on the root-mean-square radius of a nucleus $\langle r_{\mathrm{n}}^2 \rangle$ and on the charge density at the nuclear position, which is related to the probability density of electrons being at this position $|\psi_{\mathrm{el}}(0)|^2$ [14]. The Hamiltonian $\hat{H}_{\mathrm{I}}$ corresponding to this contribution reflects the finite size of a nucleus, which generally differs for different j values. Analogously to (1.9) and (1.10) the matrix forms of $\hat{H}_{\mathrm{I}}$ for the ground and excited states of ^{57}Fe are

$$\hat{H}_{\mathrm{I,g}} = \frac{Zq_0^2}{6\,\varepsilon_0} \langle r_{\mathrm{n}}^2 \rangle_{\mathrm{g}} |\psi_{\mathrm{el}}(0)|^2 \begin{pmatrix} 1 & 0 \\ 0 & 1 \end{pmatrix}, \tag{1.11}$$

$$\hat{H}_{\mathrm{I,e}} = \frac{Zq_0^2}{6\,\varepsilon_0} \langle r_{\mathrm{n}}^2 \rangle_{\mathrm{e}} |\psi_{\mathrm{el}}(0)|^2 \begin{pmatrix} 1 & 0 & 0 & 0 \\ 0 & 1 & 0 & 0 \\ 0 & 0 & 1 & 0 \\ 0 & 0 & 0 & 1 \end{pmatrix}, \tag{1.12}$$

where $\varepsilon_0 = 8.854 \cdot 10^{-12}\,\mathrm{F \cdot m^{-1}}$ is the vacuum permittivity. The scalar values in (1.11) and (1.12) can be used to derive the isomer shift parameter, which is one of the main quantities obtainable from the nuclear resonant measurements. Its relation to the electrons probability density is widely used in chemical and materials applications where its determination allows to distinguish between compounds with different atomic valence states in studied samples [17].

The last contribution to the electric interactions reflects the deviation of the electric field from the cubic symmetry. It is given by the quadrupole interaction Hamiltonian $\hat{H}_{\mathrm{Q}}$ in the form [14]

$$\hat{H}_{\mathrm{Q}} = \frac{1}{6} \left(V_{xx}\hat{Q}_{xx} + V_{yy}\hat{Q}_{yy} + V_{zz}\hat{Q}_{zz} \right), \tag{1.13}$$

where V_{ii} are the diagonal elements of the electric field gradient (EFG) tensor

$$V_{ij} = \frac{\partial^2 \varphi}{\partial x_i \partial x_j}(0), \quad i,j = x,y,z. \tag{1.14}$$

In (1.13) a simplified form of the Hamiltonian is given, where the coordinate system with the axes identical with the EFG main axes have been chosen. From the V_{xx}, V_{yy} and V_{zz} only two values are independent because the EFG tensor has a zero trace. The coordinate system is conventionally chosen so the $|V_{zz}| \geq |V_{yy}| \geq |V_{xx}|$ and the two independent parameters describing the EFG tensor are the V_{zz} component and so called asymmetry parameter η given as

$$\eta = \frac{V_{xx} - V_{yy}}{V_{zz}}. \tag{1.15}$$

The quadrupole interaction Hamiltonian can be further simplified using formulas (1.7) and (1.15) and the properties of the diagonal quadrupole moment elements $\hat{Q}_{xx}, \hat{Q}_{yy}, \hat{Q}_{zz}$ with respect to the angular momentum operators [10]. $\hat{H}_{\mathrm{Q,g}}$ corresponding to the ground state of ^{57}Fe is equal to zero because of its zero quadrupole moment ($j_{\mathrm{g}} < 1$). For the excited state the Hamiltonian is given by the formula [15]

$$\hat{H}_{\mathrm{Q,e}} = \frac{1}{4} q_0 Q_\mathrm{e} V_{zz} \begin{pmatrix} 1 & 0 & \frac{\eta}{\sqrt{3}} & 0 \\ 0 & -1 & 0 & \frac{\eta}{\sqrt{3}} \\ \frac{\eta}{\sqrt{3}} & 0 & -1 & 0 \\ 0 & \frac{\eta}{\sqrt{3}} & 0 & 1 \end{pmatrix}. \tag{1.16}$$

$\hat{H}_{\mathrm{Q,e}}$ is diagonal only for an axially symmetrical electric field, where $V_{xx} = V_{yy}$ and $\eta = 0$. The quadrupole interaction reflects the spatial charge distribution of electrons and atoms around a nucleus and thus it can be used for studying a local structural ordering.

The total interaction Hamiltonian $\hat{H}$ is the sum of the individual magnetic and electric contributions

$$\hat{H} = \hat{H}_\mathrm{I} + \hat{H}_\mathrm{Q} + \hat{H}_\mathrm{M}. \tag{1.17}$$

The eigenvalues and eigenstates (eigenvectors) of $\hat{H}$ are essential to obtain the transition energies and the probability amplitudes for the transitions between the ground and the excited states energy levels. In general, the interaction Hamiltonian is not diagonal. In the coordinate system coinciding with the EFG main axes the quadrupole interaction Hamiltonian would be diagonal for $\eta = 0$. However, even in such case the general direction of the effective magnetic field with respect to the EFG main axes would result in a non-diagonal $\hat{H}$. Therefore, the eigenvalues and eigenstates of $\hat{H}$ generally differ from those of the $\hat{J}_z$ and $\hat{J}^2$ operators and need to be obtained using a diagonalization procedure [7].

The formula (1.17) can be analogously used in the individual j-value subspaces with dimensions of $2j+1$. For the ^{57}Fe nuclide, using the formulas (1.9–1.12) and (1.16), we get $\hat{H}_\mathrm{g} = \hat{H}_\mathrm{I,g} + \hat{H}_\mathrm{M,g}$ in the 2-dimensional subspace with $j_\mathrm{g} = 1/2$ and $\hat{H}_\mathrm{e} = \hat{H}_\mathrm{I,e} + \hat{H}_\mathrm{Q,e} + \hat{H}_\mathrm{M,e}$ in the 4-dimensional subspace with $j_\mathrm{e} = 3/2$.

1.1.3 Rotation of EFG

To properly describe the absorption and emission of photons by the nuclear system the eigenvalues and eigenstates of the interaction Hamiltonian with an arbitrary EFG and $\vec{B}$ orientations in the laboratory reference frame are needed. In the following description the orientation of the magnetic field $\vec{B}$ will be given in the EFG coordinate system. The EFG will exhibit an arbitrary orientation with respect to the laboratory coordinate system (Fig. 1.2).

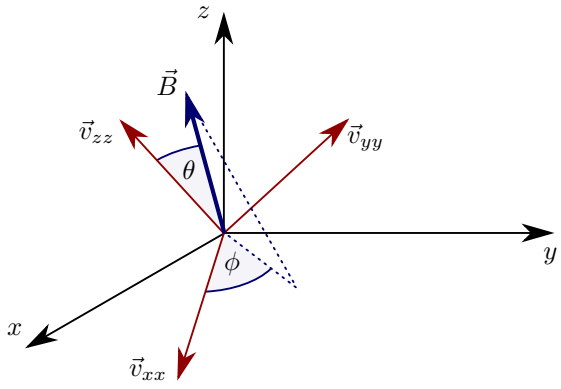

Figure 1.2: The EFG main axes given by the $\vec{v}_{xx}, \vec{v}_{yy}$ and $\vec{v}_{zz}$ vectors in the laboratory reference frame and the effective magnetic field $\vec{B}$ with angles θ and ϕ in the EFG coordinate system.

A rotation of the EFG coordinate system in the 3-dimensional space can be described by a real orthogonal 3×3 matrix, which is conventionally parametrized by three Euler angles α, β, γ. In the Hilbert space of the physical system the rotation is represented by a rotation operator $\hat{\mathcal{D}}(\alpha, \beta, \gamma)$ given as [18]

$$\hat{\mathcal{D}}(\alpha, \beta, \gamma) = \exp\left(-i\frac{\hat{J}_z\alpha}{\hbar}\right)\exp\left(-i\frac{\hat{J}_y\beta}{\hbar}\right)\exp\left(-i\frac{\hat{J}_z\gamma}{\hbar}\right). \tag{1.18}$$

For the system in a quantum state $|\psi\rangle$ before the rotation, the corresponding "rotated" quantum state $|\psi\rangle_{\mathrm{r}}$ is

$$|\psi\rangle_{\mathrm{r}} = \hat{\mathcal{D}}(\alpha, \beta, \gamma)\,|\psi\rangle\,. \tag{1.19}$$

Matrix representation of the rotation operator in a given j-value subspace is given by the Wigner matrix elements [19]

$$\mathcal{D}^{(j)}_{m'm}(\alpha, \beta, \gamma) = \left\langle j, m'\middle|\hat{\mathcal{D}}(\alpha, \beta, \gamma)\middle|j, m\right\rangle. \tag{1.20}$$

It could be found out that for $|\psi\rangle = |j, \psi\rangle$ being the eigenstate of the $\hat{J}^2$ operator with the eigenvalue of $\hbar^2 j(j+1)$, the rotated quantum state $\hat{\mathcal{D}}(\alpha, \beta, \gamma)\,|j, \psi\rangle$ is still an eigenstate $|\psi\rangle_{\mathrm{r}} = |j, \psi\rangle_{\mathrm{r}}$ of $\hat{J}^2$ with the same eigenvalue, i.e. the rotation does not affect the j quantum number [7].

Diagonalization of the interaction Hamiltonian (1.17) for individual j-value subspaces would lead to eigenvalues $E^{(j)}_n$ and eigenstates $|j, \psi_n\rangle$. The index n takes $2j+1$ different values. The eigenstates $|j, \psi_n\rangle$ can be defined by their coefficients $\psi^{(j)}_{m,n}$ (m-th coefficient of the n-th eigenstate) according to formula

$$|j, \psi_n\rangle = \sum_{m=-j}^{j} |j, m\rangle\langle j, m|j, \psi_n\rangle = \sum_{m=-j}^{j} \psi^{(j)}_{m,n}\,|j, m\rangle. \tag{1.21}$$

The next step is to determine the eigenvalues and eigenstates of the Hamiltonian in the laboratory reference frame with a general orientation of EFG (Fig. 1.2). As the application of the rotation operator is a unitary transform with respect to $\hat{H}$, the eigenvalues of the Hamiltonian remain unchanged after the rotation [7]. However, the eigenstates generally change according to (1.19). The coefficients of the rotated eigenstates $\varphi^{(j)}_{m',n} = \langle j, m'|j, \psi_n\rangle_{\mathrm{r}}$ ($m' = -j, -j+1, \ldots, j-1, j$) can be written as

$$\varphi^{(j)}_{m',n} = \langle j, m'|\,\mathcal{D}(\alpha, \beta, \gamma)\sum_{m=-j}^{j} \psi^{(j)}_{m,n}\,|j, m\rangle = \sum_{m=-j}^{j} \psi^{(j)}_{m,n}\mathcal{D}^{(j)}_{m'm}(\alpha, \beta, \gamma). \tag{1.22}$$

The values of $E^{(j)}_n$ and $\varphi^{(j)}_{m',n}$ could be obtained according to the previously described procedure for an arbitrary combination of the hyperfine interactions. A simplified results can be obtained in the special cases of (i) zero magnetic hyperfine interaction and axially symmetrical electric field, (ii) zero quadrupole hyperfine interaction and (iii) combined electric and magnetic interactions with $\vec{B}$ parallel to the EFG main axes. For such cases the laboratory coordinate system can be chosen in such way so that $\hat{H}$ commutes with $\hat{J}_z$ and $\hat{J}^2$ operators and all these operators have a common set of eigenstates. The coefficients $\psi^{(j)}_{m,n}$ then reduce to a Kronecker delta $\delta_{m,n}$, where n now labels a given $|j, n\rangle$ angular

momentum eigenstate ($n = -j, -j+1, \ldots, j-1, j$). Using the formula (1.22) we get the eigenstates in a general coordinate system

$$\varphi^{(j)}_{m',n} = \langle j, m'|j, n\rangle_{\mathrm{r}} = \sum_{m=-j}^{j} \delta_{m,n} \mathcal{D}^{(j)}_{m'm}(\alpha, \beta, \gamma) = \mathcal{D}^{(j)}_{m'n}(\alpha, \beta, \gamma). \tag{1.23}$$

1.1.4 Hyperfine Splitting

The eigenvalues of the interaction Hamiltonian $E^{(j)}_n$ represent changes in the energies corresponding to the individual quantum states of nuclei. In the absence of the hyperfine interactions the nuclear system exhibits degeneracy, i.e. for given j there are $2j+1$ different stationary states of nuclei with the same energy $\mathcal{E}^{(j)}$. Thanks to the hyperfine interactions the degeneracy is lifted and a hyperfine splitting of the energy levels occurs. The splitting contains information on the hyperfine interactions and may provide a unique insight into the local nuclei surroundings. In the following part the hyperfine splitting of ^{57}Fe energy levels is demonstrated for individual types of interactions.

Although the interaction $\hat{H}_{\mathrm{I}}$ does not remove the degeneracy, it causes the energy levels $\mathcal{E}^{(j_{\mathrm{g}})}$ and $\mathcal{E}^{(j_{\mathrm{e}})}$ to be shifted into $\mathcal{E}^{(j_{\mathrm{g}})} + \frac{Z_{\mathrm{n}} q_0^2}{6\,\varepsilon_0} \langle r^2_{\mathrm{n}}\rangle_{\mathrm{g}} |\psi_{\mathrm{el}}(0)|^2$ and $\mathcal{E}^{(j_{\mathrm{e}})} + \frac{Z_{\mathrm{n}} q_0^2}{6\,\varepsilon_0} \langle r^2_{\mathrm{n}}\rangle_{\mathrm{e}} |\psi_{\mathrm{el}}(0)|^2$ for the ground and the excited state, respectively. The original difference between the energies $\mathcal{E}^{(j_{\mathrm{e}})} - \mathcal{E}^{(j_{\mathrm{g}})}$ is therefore increased by the value of $\frac{Z_{\mathrm{n}} q_0^2}{6\,\varepsilon_0} \left(\langle r^2_{\mathrm{n}}\rangle_{\mathrm{e}} - \langle r^2_{\mathrm{n}}\rangle_{\mathrm{g}}\right) |\psi_{\mathrm{el}}(0)|^2$. Different electronic surroundings of nuclei result in a different shift of the energy difference. However, this cannot be directly measured as an absolute value. It can be determined only as a relative value with respect to a reference material. This relative change defines the isomer shift parameter δ as [14, 17]

$$\delta = \frac{Z_{\mathrm{n}} q_0^2}{6\,\varepsilon_0} \left(\langle r^2_{\mathrm{n}}\rangle_{\mathrm{e}} - \langle r^2_{\mathrm{n}}\rangle_{\mathrm{g}}\right) \left(|\psi_{\mathrm{el}}(0)|^2 - |\psi_{\mathrm{ref}}(0)|^2\right), \tag{1.24}$$

where $|\psi_{\mathrm{ref}}(\vec{r})|^2$ is the electronic probability density in the reference system.

In the absence of the magnetic interactions, the electric quadrupole interaction $\hat{H}_{\mathrm{Q}}$ splits only the excited state energy levels (the ground state exhibits a zero quadrupole moment). The degeneracy is lifted partially, where for an axially symmetrical electric field the energies are shifted by $+\frac{1}{4} q_0 Q_{\mathrm{e}} V_{zz}$ for $|j_{\mathrm{e}}, \pm 3/2\rangle$ states and by $-\frac{1}{4} q_0 Q_{\mathrm{e}} V_{zz}$ for $|j_{\mathrm{e}}, \pm 1/2\rangle$ states (Fig. 1.3a). Depending on the sign of V_{zz} one excited energy level is increased and one decreased by the value of $\frac{1}{4} q_0 Q_{\mathrm{e}} |V_{zz}|$. The difference between these two levels can be written as $|\Delta|$, where [14]

$$\Delta = \frac{1}{2} q_0 Q V_{zz} \tag{1.25}$$

is the quadrupole splitting parameter. The degeneracy can be completely broken in the presence of the magnetic hyperfine interaction. For example, if $\hat{H}_{\mathrm{Q}} = 0$ the energy shifts are $-m_{\mathrm{g}} \gamma_{\mathrm{G,g}} \hbar B$ for $|j_{\mathrm{g}}, m_{\mathrm{g}}\rangle$ and $-m_{\mathrm{e}} \gamma_{\mathrm{G,e}} \hbar B$ for $|j_{\mathrm{e}}, m_{\mathrm{e}}\rangle$ states (Fig. 1.3b).

To extract the information on the hyperfine splitting, nuclear resonant methods based on the transitions between the individual nuclear energy levels have been developed. These methods include nuclear magnetic and nuclear quadrupole resonance, Mössbauer spectroscopy in the transmission (emission) or reflection geometry and NRS techniques using the synchrotron radiation source.

The principle of the listed methods is the application of an electromagnetic radiation of a proper energy (wavelength). The absorption and consequent reemission of photons

by nuclei is accompanied by the excitation-deexcitation of the nuclear energy levels. This process exhibits a sharp resonant behaviour that allows to reconstruct the information on the transition energies, from which the parameters of the hyperfine interactions can be obtained. The list of the hyperfine parameters that provide information on a given nuclear surrounding is given in Table 1.2.

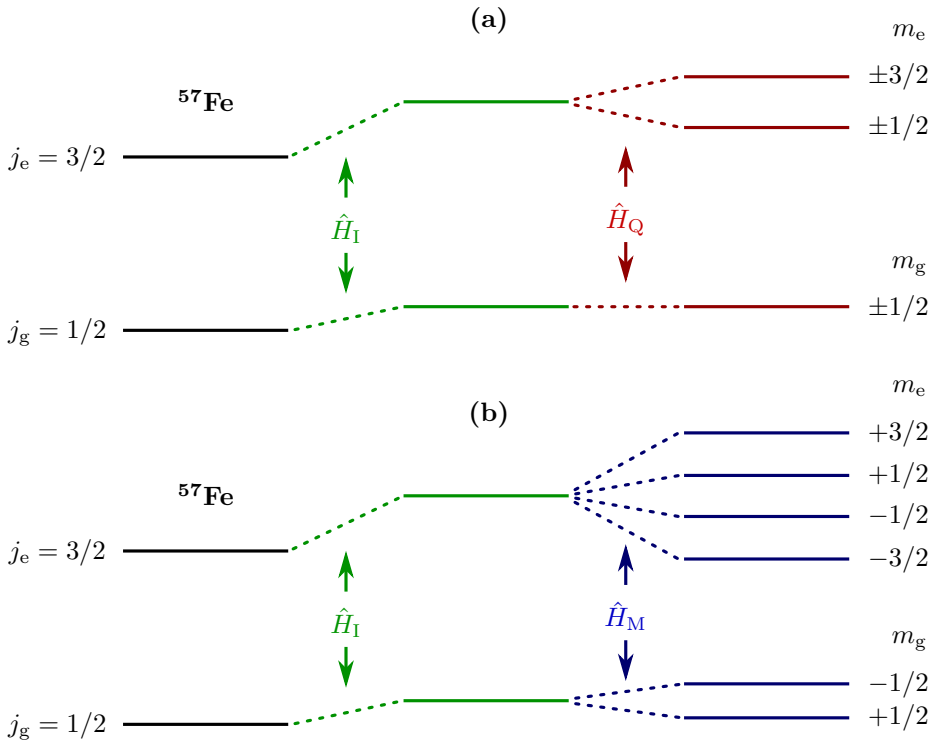

Figure 1.3: A schematic illustration of the ^{57}Fe nuclear hyperfine splitting caused by the hyperfine interactions. (a) A combination of $\hat{H}_I$ and $\hat{H}_Q$ interactions, which partially remove the degeneracy. (b) A completely broken degeneracy by $\hat{H}_I$ and $\hat{H}_M$ interactions.

Magnetic interactions	**Electric interactions**
eff. mag. field magnitude B	isomer shift δ
polar angle θ	quadrupole splitting Δ
azimuth angle ϕ	asymmetry parameter η
	EFG orientation (Euler angles) α, β, γ

Table 1.2: List of hyperfine parameters conventionally used for describing interactions of nuclei with their surrounding and the related hyperfine splitting of the nuclear energy levels.

1.2 Nuclear Resonant Scattering

For a given nuclear resonant method a suitable energy of the electromagnetic radiation is chosen to excite the nuclear energy levels. The nuclear magnetic resonance and nuclear quadrupole resonance methods are based on the transitions between the individual ground state energy levels. They use the radiation in the frequency range 0.1–1000 MHz. For details regarding these methods the readers are referred to the designated literature [20, 21]. Here we focus on the conventional Mössbauer spectroscopy and the synchrotron radiation nuclear resonant scattering (NRS) methods, that utilize electromagnetic radiation in the 1–100 keV energy range. These energies belong to the hard X-ray and gamma radiation domain and are suitable for transitions between the ground and excited state energy levels. An example of the energy transitions is given in Fig. 1.4.

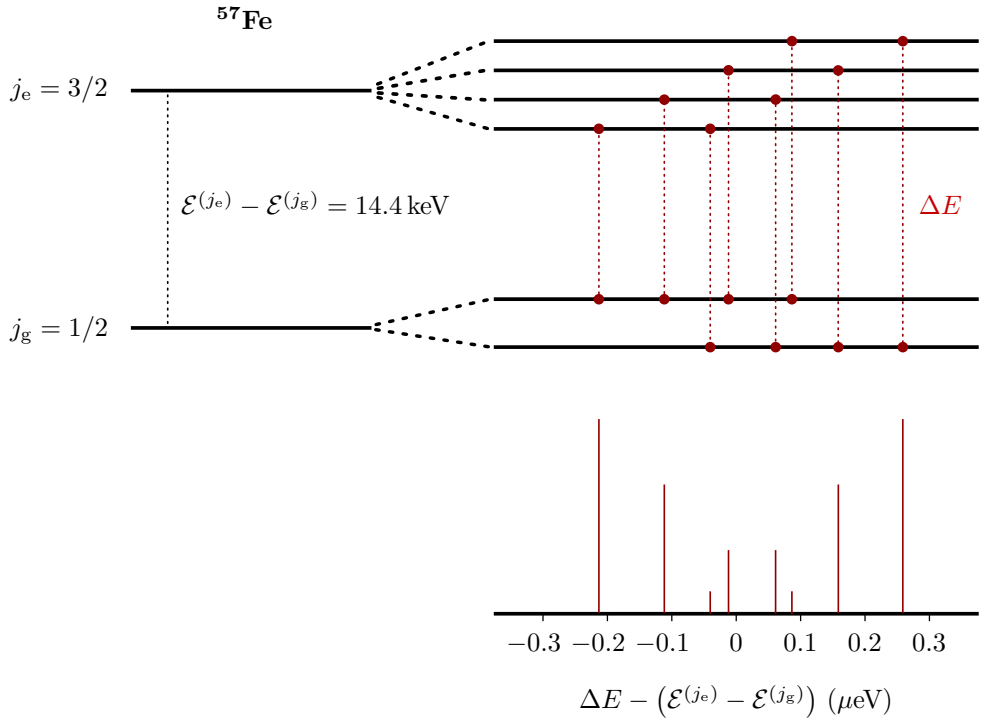

Figure 1.4: Scheme of the ^{57}Fe nuclear transitions between the ground and excited state energy levels. Thanks to the hyperfine splitting the individual transition energies are slightly shifted from the $\mathcal{E}^{(j_\mathrm{e})} - \mathcal{E}^{(j_\mathrm{g})}$ transition energy between the unsplit levels.

1.2.1 Mössbauer Effect

The transitions between the ground and excited state energy levels ($j_g \leftrightarrow j_\mathrm{e}$) of ^{57}Fe nuclei exhibit an energy of 14.4 keV. On the other hand, the hyperfine splitting of the individual levels goes typically below 1 μeV (see Fig. 1.4). That is more than 10 orders of magnitude less. Considering measurements in energy domain, an outstanding energy resolution is required for observing the energy shifts of individual nuclear transitions.

The interaction of the electromagnetic radiation with nuclei proceeds in agreement with energy and momentum conservation laws [10]. The momentum conservation results in absorption and emission of photons with recoil. Part of the photon energy is transferred

to the energy of atomic motion. As a result, the energy of the absorbed or emitted photons is not equal to the transition energy between the ground and excited states, but is shifted by the recoil energy (Fig. 1.5).

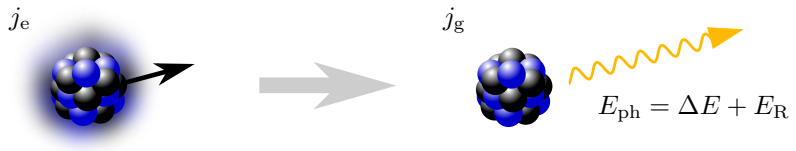

Figure 1.5: A schematic example of the photon emission with recoil. The transition of a nucleus from an excited to a ground energy level is accompanied by the lost of the atomic motion energy (energy of the recoil, illustrated by the black arrow on the left). The energy of the emitted photon E_{ph} is then equal to the transition energy ΔE, increased by the recoil energy E_R.

Quantum mechanically, the recoil proceeds via the creation or annihilation of phonon modes in a solid lattice. The energy transferred between photons and the phonon system is in the range of meV. This has been utilized in the synchrotron radiation based nuclear resonant inelastic X-ray scattering (NRIXS) where tuning of the photon energy in the meV range using X-ray optics equipment can be realized [22]. By scanning the energy of the incident radiation and measuring the intensities of resonantly scattered photons a phonon energy spectrum can be obtained, which provides the information on the lattice dynamics [23, 24].

An example of the phonon spectrum is given in Fig. 1.6. The centre of the energy axis corresponds to the transition energy between the ground and excited state energy levels. The right side of the spectrum describes the absorption of photons with energy, which is higher than the transition energy. Therefore, part of the photon energy was transferred to the lattice via creation of phonon quanta. Analogously, the left side of the spectrum describes the absorption of lower-energy photons, which is accompanied by annihilation of phonons.

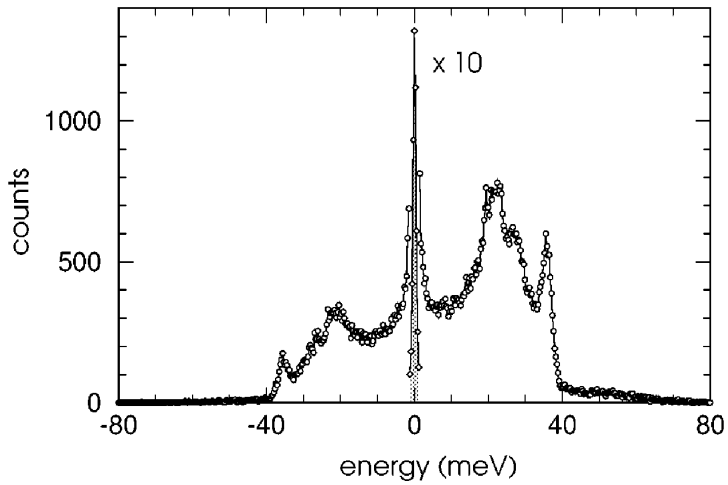

Figure 1.6: An example of a phonon energy spectrum measured by NRIXS. The data were taken from [25].

Despite being very useful in various scientific fields, the photon absorption and emission with recoil significantly complicates observation of the hyperfine splitting. The information on the nuclear transition energies is lost in the energy exchange with the lattice. New possibilities came with a recoilless absorption and emission of photons discovered by Rudolph Mössbauer in 1958 [26]. The conducted experiment showed that absorption and emission of photons in a solid may occur without the creation or annihilation of phonon quanta. Instead, the whole lattice may exhibit the recoil. Considering the total mass of a solid system, the energy taken by this recoil is negligible with respect to a given transition energy. This has two significant consequences. First, the photons absorbed and emitted without recoil can be used to obtain the information on the split nuclear energy levels and the related hyperfine interactions. Second, the linewidth of the recoilless emission is close to the natural linewidth of the nuclear excited state energy level ($\sim 10^{-8}\,\mathrm{eV}$). This allows to realize a gamma radiation source with energy resolution of 10^{-12}, which is sufficient for the observation of hyperfine splitting. The Mössbauer spectroscopy methods, which utilize such radiation sources, are described in section 1.3.1.

The relative number of recoilless events is expressed by the Lamb-Mössbauer factor f_{LM} (also known as the f-factor or the recoilless fraction) [14]

$$f_{\mathrm{LM}} = \exp\left(-\frac{4\pi^2 \langle x^2 \rangle}{\lambda^2}\right), \tag{1.26}$$

where λ is the radiation wavelength and $\langle x^2 \rangle$ is the atomic mean square vibrational amplitude. Greater radiation energy (lower wavelength) results in lower probability for the absorption and emission of photons without recoil. For a given nuclide the radiation energy is fixed (e.g. 14.4 keV for ^{57}Fe) and f_{LM} depends solely on $\langle x^2 \rangle$, which is related to the properties of the crystal lattice and the temperature. The Lamb-Mössbauer factor plays an important role in the recoilless absorption and emission measurements and in the experimental data analysis. Moreover, measurements of f_{LM} and its temperature dependence can be also used to explore the lattice dynamics [27–29].

1.2.2 Scattering Length

Generally, the electromagnetic radiation may interact with a solid in many different ways. For example, the interaction with electrons can take place via coherent scattering, photoelectric effect, Compton scattering or electron-positron pair production [30]. The resonant scattering on atomic nuclei, described as a photon absorption-reemission process, could occur with or without recoil. Furthermore, when a photon is absorbed the excited nucleus may deexcite not only by emitting a photon but also by emitting a conversion electron instead [30]. This is also accompanied by secondary effects such as the emission of conversion X-rays and Auger electrons. The scattering via conversion process is used in the conversion electron Mössbauer spectroscopy (CEMS) and conversion X-ray Mössbauer spectroscopy (CXMS) techniques. The cross-sections of individual types of interaction depend on the properties of the scattering system and on the radiation energy.

The TMS and NFS methods are based on the recoilless absorption and reemission of photons which satisfies two basic conditions. First, the state of the solid system after the scattering is identical to its initial state. Second, the energy of the system is not changed by the scattering, thus the energy of the emitted and the absorbed photon is the same. In other words, the scattering of the radiation on the nuclear system is coherent and elastic [31]. Another common characteristics of TMS and NFS is that the radiation is

detected in the forward direction. Denoting the wave vector of the incident (absorbed) photon as $\vec{k}_{\mathrm{in}}$ and the wave vector of the scattered (emitted) photon as $\vec{k}$ the forward scattering follows the relation $\vec{k} = \vec{k}_{\mathrm{in}}$.

The semi-classical theoretical formalism developed for the nuclear resonant coherent elastic scattering considers the solid system as a continuous optical medium described by an energy dependent index of refraction [11, 32]. Generally, the index of refraction is a multidimensional matrix that includes all possible scattering routes of electronic and nuclear origin. To simplify the description, the non-resonant scattering routes including the electronic contributions can be omitted. The nuclear resonant contribution given by the scattering length N reflects probability amplitudes for absorption-emission processes between individual ground and excited nuclear quantum states. The scattering length can be written as [32]

$$N_{\vec{\varepsilon},\vec{\varepsilon}_{\mathrm{in}}} \propto \sum_{n_{\mathrm{g}},n_{\mathrm{e}}} \frac{\left\langle j_{\mathrm{g}}, n_{\mathrm{g}}; \vec{k}, \vec{\varepsilon}_{\mathrm{in}} | \hat{\mathcal{H}} | j_{\mathrm{e}}, n_{\mathrm{e}} \right\rangle \left\langle j_{\mathrm{e}}, n_{\mathrm{e}} | \hat{\mathcal{H}} | j_{\mathrm{g}}, n_{\mathrm{g}}; \vec{k}, \vec{\varepsilon} \right\rangle}{E - \Delta E_{n_{\mathrm{g}},n_{\mathrm{e}}} + i\,\Gamma/2}, \tag{1.27}$$

where the sum runs over all possible ground and excited states. The vectors $\vec{\varepsilon}_{\mathrm{in}}, \vec{\varepsilon}$ define the polarizations of the absorbed and the emitted photon. The operator $\hat{\mathcal{H}}$ is the Hamiltonian of the interaction between the nuclear system and the electromagnetic radiation [33]. The resonant character is given by Lorentzian functions $L^{n_{\mathrm{e}}}_{n_{\mathrm{g}}}(E)$ in the form

$$L^{n_{\mathrm{e}}}_{n_{\mathrm{g}}}(E) = \frac{1}{E - \Delta E_{n_{\mathrm{g}},n_{\mathrm{e}}} + i\Gamma/2}, \tag{1.28}$$

where E is the photon energy, $\Delta E_{n_{\mathrm{g}},n_{\mathrm{e}}}$ is the transition energy between the ground and excited state and Γ is the natural linewidth of the excited energy level.

Formula (1.27) can be simplified depending on a given resonant nuclide and the corresponding transition properties. In the case of ^{57}Fe the magnetic dipole transition (M1) dominates [34] and the scattering length is explicitly given as[2] [11, 35]

$$N_{\vec{\varepsilon},\vec{\varepsilon}_{\mathrm{in}}} = \sum_{n_{\mathrm{g}},n_{\mathrm{e}}} L^{n_{\mathrm{e}}}_{n_{\mathrm{g}}}(E) \sum_{M',M=-1}^{1} \left[\vec{\varepsilon}^{\,*} \cdot \vec{Y}_{M'}(\vec{k})\right] \left[\vec{Y}^{\,*}_{M}(\vec{k}) \cdot \vec{\varepsilon}_{\mathrm{in}}\right] G^{n_{\mathrm{g}},n_{\mathrm{e}}}_{M'} \left(G^{n_{\mathrm{g}},n_{\mathrm{e}}}_{M}\right)^{*}, \tag{1.29}$$

where $\vec{Y}_M$ are vector spherical harmonics corresponding to the M1 transition [35, 36]. The first dependence of the scattering on the hyperfine parameters is hidden in the resonant energies $\Delta E_{n_{\mathrm{g}},n_{\mathrm{e}}}$, which depend on the eigenvalues of the interaction Hamiltonian (see section 1.1). The second dependence is hidden in the $G^{n_{\mathrm{g}},n_{\mathrm{e}}}_{M}$ factors, which depend on the components of the Hamiltonian eigenstates according to formula

$$G^{n_{\mathrm{g}},n_{\mathrm{e}}}_{M} = \sum_{m_{\mathrm{g}}=-j_{\mathrm{g}}}^{j_{\mathrm{g}}} \left(\varphi^{(j_{\mathrm{g}})}_{m_{\mathrm{g}},n_{\mathrm{g}}}\right)^{*} \varphi^{(j_{\mathrm{e}})}_{m_{\mathrm{g}}+M,n_{\mathrm{e}}} C(j_{\mathrm{g}} 1 j_{\mathrm{e}}; m_{\mathrm{g}} M). \tag{1.30}$$

The formula respects the rules of angular momenta addition, where for the dipole transition of ^{57}Fe the $j = j_{\mathrm{g}} = 1/2$ and $j = 1$ angular momenta are being coupled [19]. Therefore, the non-zero contributions for $m_{\mathrm{e}} = m_{\mathrm{g}} + M$ are included and multiplied by corresponding Clebsch-Gordan coefficients $C(j_{\mathrm{g}} 1 j_{\mathrm{e}}; m_{\mathrm{g}} M)$.

[2] In contrast to the conventionally defined scattering length the introduced quantity has different units. To simplify the description, certain constants were excluded from the formula. They will be included into a common constant introduced later.

In general, the polarization $\vec{\varepsilon}_{\mathrm{in}}$ of the absorbed photon may not be the same as the polarization $\vec{\varepsilon}$ of the emitted photon. It is convenient to introduce a matrix formalism to consider possible polarization changes and describe the scattering for arbitrary polarization states of the incident radiation [37,38]. In the linear polarization basis given by orthogonal unit vectors $\vec{\varepsilon}_\sigma$, $\vec{\varepsilon}_\pi$ the scattering length N is a 2-dimensional matrix, which can be written as a sum (compare with formula (1.29))

$$N = \sum_{n_{\mathrm{g}},n_{\mathrm{e}}} L_{n_{\mathrm{g}}}^{n_{\mathrm{e}}}(E)\, n^{n_{\mathrm{g}},n_{\mathrm{e}}}, \tag{1.31}$$

i.e.

$$\begin{pmatrix} N_{\sigma\sigma} & N_{\sigma\pi} \\ N_{\pi\sigma} & N_{\pi\pi} \end{pmatrix} = \sum_{n_{\mathrm{g}},n_{\mathrm{e}}} L_{n_{\mathrm{g}}}^{n_{\mathrm{e}}}(E) \begin{pmatrix} n_{\sigma\sigma}^{n_{\mathrm{g}},n_{\mathrm{e}}} & n_{\sigma\pi}^{n_{\mathrm{g}},n_{\mathrm{e}}} \\ n_{\pi\sigma}^{n_{\mathrm{g}},n_{\mathrm{e}}} & n_{\pi\pi}^{n_{\mathrm{g}},n_{\mathrm{e}}} \end{pmatrix}, \tag{1.32}$$

where the elements of the $n^{n_{\mathrm{g}},n_{\mathrm{e}}}$ matrices are

$$n_{\nu\mu}^{n_{\mathrm{g}},n_{\mathrm{e}}} = \sum_{M'=-1}^{1} \sum_{M=-1}^{1} \left[\vec{\varepsilon}_\nu^{\,*} \cdot \vec{Y}_{M'}(\vec{k})\right] \left[\vec{Y}_M^{\,*}(\vec{k}) \cdot \vec{\varepsilon}_\mu\right] G_{M'}^{n_{\mathrm{g}},n_{\mathrm{e}}} \left(G_M^{n_{\mathrm{g}},n_{\mathrm{e}}}\right)^*, \quad \mu,\nu \in \{\sigma,\pi\}\,. \tag{1.33}$$

Application of the scattering length to the incident radiation wave field $\vec{A}_{\mathrm{in}}$ to obtain the resulting scattered field $\vec{A}_{\mathrm{sc}} = N\vec{A}_{\mathrm{in}}$ is a good approximation for very thin scattering systems (kinematical approximation), where only the single scattering process occurs [39]. For a scattering system of an arbitrary thickness the multiple scattering effects must be included into the description.

To quantitatively evaluate the rate of the multiple scattering in real solids the effective thickness d_{eff} is conventionally used. It is a dimensionless quantity defined by formula [40]

$$d_{\mathrm{eff}} = \sigma_0 f_{\mathrm{LM}} \varrho d, \tag{1.34}$$

where f_{LM} is the Lamb-Mössbauer factor, ϱ is the density of the resonant nuclei in the units of m^{-3}, d is the thickness of the scattering system and σ_0 is the nuclear resonant effective cross-section. Strictly speaking, a studied sample may be classified as ideally thin if the condition $d_{\mathrm{eff}} \ll 1$ is satisfied. However, the measurements are often conducted on much thicker samples and whether the multiple scattering significantly influences the measurements or not depends on particular sample properties, experimental conditions and the quantities that are being extracted from the measurements [41].

All possible scattering paths (single scattering, double scattering, ...) including the case of no resonant interaction with the nuclear system are included in the resulting scattering matrix (transmission matrix) T, which takes the exponential form [11]

$$T = \mathrm{e}^{i\xi N}. \tag{1.35}$$

The constant ξ reflects the effective thickness of the system and for the ^{57}Fe transition it is given as

$$\xi = -\frac{\pi\Gamma d_{\mathrm{eff}}}{2}\,. \tag{1.36}$$

The application of the scattering matrix to the incident radiation field gives the transmitted radiation field in the forward direction

$$\vec{A}_{\mathrm{tr}} = T\vec{A}_{\mathrm{in}}. \tag{1.37}$$

The transmitted field can be understood as a superposition of the field $\vec{A}_{\mathrm{in}}$ (no resonant interaction with nuclei) and the scattered field [42]

$$\vec{A}_{\mathrm{tr}} = \vec{A}_{\mathrm{sc}} + \vec{A}_{\mathrm{in}}, \tag{1.38}$$

from which the scattered field could be written analogously to (1.37) as

$$\vec{A}_{\mathrm{sc}} = (T - \mathbf{I})\,\vec{A}_{\mathrm{in}}, \tag{1.39}$$

where $\mathbf{I}$ is the unit matrix. The outlined scattering matrix formalism could be used for arbitrary sample thickness and allows to include important physical phenomena such as the polarization mixing into considerations.

1.2.3 Nuclear Sites

The scattering length given by formulas (1.31–1.33) describes a homogeneous scattering system containing one nuclear site (Mössbauer site, spectral component). This means that all the resonant nuclei in the system have exactly the same surrounding described by a common set of hyperfine parameters. However, in the real samples a discrete or a continuous distribution of different nuclear sites (nuclei with different local surroundings) can occur. Each nuclear site may exhibit a different hyperfine splitting, which contributes to the resulting final form of the experimental data.

Discrete nuclear sites are common for various types of multiphase materials in either compact or powder form. Multiple nuclear sites also appear in single crystalline phases with non-equivalent crystallographic sites (Fig. 1.7). Retrieving the information on the individual phases and crystallographic positions is one of the main goals of the nuclear resonant methods applied in chemistry, solid state physics and materials science [43–45].

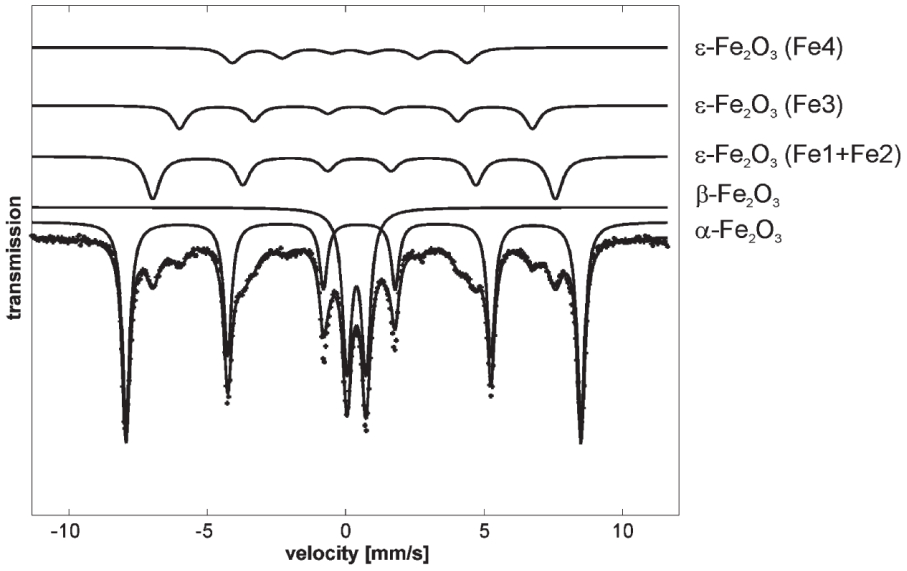

Figure 1.7: Example of a transmission Mössbauer spectrum measured on a sample containing different iron oxide phases. The spectrum contains five distinguishable contributions ascribed to individual nuclear sites. These are α-Fe_2O_3 and β-Fe_2O_3 with single crystallographic sites and ε-Fe_2O_3 with three distinguishable crystallographic sites. The data were taken from [44].

The presence of more nuclear sites gives more possibilities for the interaction of photons with the nuclear system. The total scattering length is then given as a finite sum

$$N = \sum_i w_i N_i, \tag{1.40}$$

where the weight factors w_i give the relative ratio of the i-th nuclear site in the material ($\sum_i w_i = 1$) and the corresponding scattering lengths N_i are calculated from (1.31–1.33). Formula (1.35) can still be used for arbitrary homogeneous material if the scattering length in the exponent is taken as the total scattering length.

The case of continuous distributions needs to be included if the studied solid system exhibits a sufficiently significant disorder of chemical, structural or magnetic nature. This can be demonstrated on the example of metallic glasses, i.e. materials with a high degree of disorder related to their amorphous structure [46,47]. Thanks to this disorder each nucleus may exhibit slightly different hyperfine interactions. Distribution functions for corresponding hyperfine parameters are then used instead of discrete sharp values (Fig. 1.8). The interpretation of the nuclear surroundings is then quite different from the discrete case. Rather than a system consisting of a high number of distinguishable nuclear sites, it is more properly described as a single nuclear site system, where the values of hyperfine parameters follow a given statistical distribution.

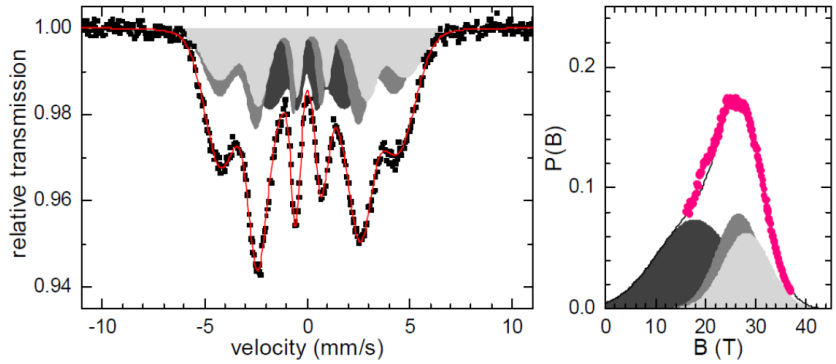

Figure 1.8: Example of a transmission Mössbauer spectrum measured on $Fe_{90}Zr_7B_3$ metallic glass (on the left). The sample contains three nuclear sites exhibiting distributions of hyperfine magnetic field magnitudes (on the right). The data were taken from [46].

A generalisation of the total scattering length for the continuous case can be done by replacing the discrete sum with an integral

$$N = \int N(p) f(p)\, \mathrm{d}p, \tag{1.41}$$

where p stands for a hyperfine parameter or a set of hyperfine parameters whose values are distributed. $N(p)$ is again the partial scattering length given by (1.31–1.33) with explicitly written dependence on the hyperfine parameters. The distribution (weight) function $f(p)$ is a continuous non-negative function satisfying the normalisation condition $\int f(p)\, \mathrm{d}p = 1$.

It is appropriate to distinguish between magnitude distributions and directional distributions as each of these two types influences the sample measurements and their results differently. The term "distribution of hyperfine parameters" then usually refers to the magnitude distributions. These are often ascribed to the quadrupole splitting parameter

Δ and to the magnitude of the effective magnetic field B. The directional distributions (distributions of electric and magnetic field orientations) are closely related to the texture problem, which will be closely discussed in chapter 3.

1.3 Coherent Elastic Forward Scattering

The information on the nuclear hyperfine splitting is coded in the scattering length N and can be potentially extracted from the measured intensities of the transmitted or the scattered radiation fields. The theoretical formalism outlined in the previous sections can be applied in both energy and time domain measurements. The differences between the energy domain TMS and the time domain NFS are related mainly to their experimental arrangements and the used radiation sources.

1.3.1 Transmission Mössbauer Spectroscopy

The transmission Mössbauer spectroscopy utilizes a suitable radioactive material as a source of gamma photons. For example, the ^{57}Co radioactive nuclide built in a solid matrix is used as a source for excitation of ^{57}Fe energy levels [48]. During the decay process the ^{57}Co nuclei transform into ^{57}Fe nuclei, which are in excited quantum states and can subsequently deexcite by emitting the 14.4 keV photons (Fig. 1.9). Depending on the Lamb-Mössbauer factor of the source, part of the radiation is emitted without recoil and the source exhibits an extremely narrow emission line.

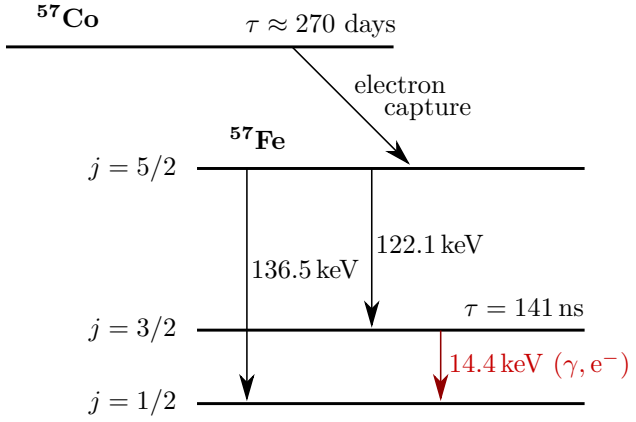

Figure 1.9: Scheme of the ^{57}Co radioactive decay. The deexcitation into the ground state of ^{57}Fe may proceed via emission of 14.4 keV gamma photons. Conversion electrons could also be emitted during the process. The lifetimes of corresponding nuclei states are given by τ.

Principle of the Mössbauer measurement in the transmission geometry is demonstrated in Fig. 1.10. Mössbauer transmission spectrum, measured as the transmitted radiation intensity $I_{\mathrm{tr}}(E)$, is obtained by modulating of the source emission energy and simultaneous detection of the transmitted photons. The modulation of the emission line is realized by changing the relative velocity v of the source with respect to the measured sample [2, 49]. According to the Doppler effect the energy of the emitted radiation is equal to

$$E = \Delta E_{\mathrm{s}} \left(1 + \frac{v}{c}\right), \tag{1.42}$$

where $c = 299\,792\,458\,\mathrm{m/s}$ is the speed of light and ΔE_s is the source transition energy. When the source is at rest with respect to the sample the emitted photons have energy equal to ΔE_s. When the source moves towards the sample the energy is increased and vice versa. The velocity change of $1\,\mathrm{mm/s}$ causes the energy of $14.4\,\mathrm{keV}$ to be shifted approximately by $48\,\mathrm{neV}$. Therefore, in ^{57}Fe Mössbauer spectroscopy the scanning range of less than $20\,\mathrm{mm/s}$ is usually enough to cover all the sample transition energies. As the radiation energy is directly related to the source velocity by (1.42) the energy axis of measured spectra is conventionally displayed in the mm/s velocity units.

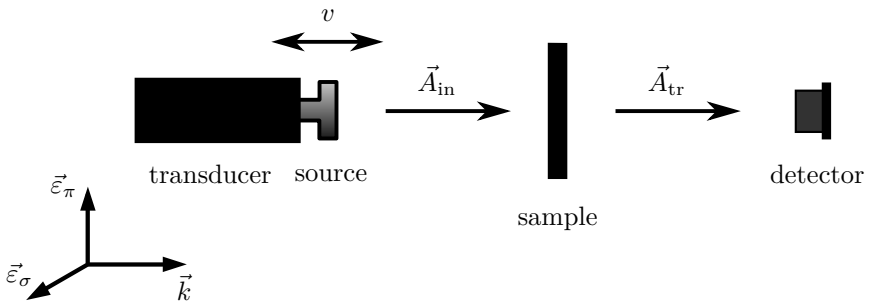

Figure 1.10: Demonstration of TMS experimental arrangement. The radioactive source is moved by the velocity transducer unit and the transmitted radiation intensity is detected for each velocity (energy) point.

If the incident radiation is in a pure polarization state (linear, circular or elliptical polarization) the transmission intensity is simply a magnitude squared of the transmitted radiation field given by (1.37). Although Mössbauer spectrometers with a polarized gamma source can be realized [50, 51], the radiation coming from a radioactive source is generally unpolarized. The density matrix formalism can be used to obtain transmission spectrum for mixed polarization states of the incident radiation [11, 32]. $I_\mathrm{tr}(E)$ can be written in a compact and normalised form

$$I_\mathrm{tr}(E) = \mathrm{Tr}\left\{T\rho T^\dagger\right\}, \tag{1.43}$$

where ρ is the density matrix describing the incident radiation. For the special cases of linearly polarized radiation in the direction of the $\vec{\varepsilon}_\sigma$ vector and unpolarized radiation the corresponding density matrices ρ_σ and ρ_u are given as

$$\rho_\sigma = \begin{pmatrix} 1 & 0 \\ 0 & 0 \end{pmatrix}, \quad \rho_u = \frac{1}{2}\begin{pmatrix} 1 & 0 \\ 0 & 1 \end{pmatrix}. \tag{1.44}$$

If the the radiation energy E is off-resonance with respect to the sample transition energies the coherent elastic nuclear resonant scattering is suppressed. On the other hand, if the radiation is tuned to a resonance then the coherent elastic nuclear resonant scattering becomes significant and the measured spectrum exhibits an intensity attenuation [42] (see Fig. 1.11). This could be interpreted as a resonant absorption (photons are absorbed and reemitted not into the forward direction) resulting in Mössbauer absorption lines in the spectrum. Positions, amplitudes and shapes of the Mössbauer lines are then essential to extract the required information on the sample. Thanks to the linear relation between the source velocity and the radiation energy the measured Mössbauer spectra can be directly

compared to the theory and after a proper data evaluation the information on the nuclear sites in the sample and their hyperfine parameters can be obtained.

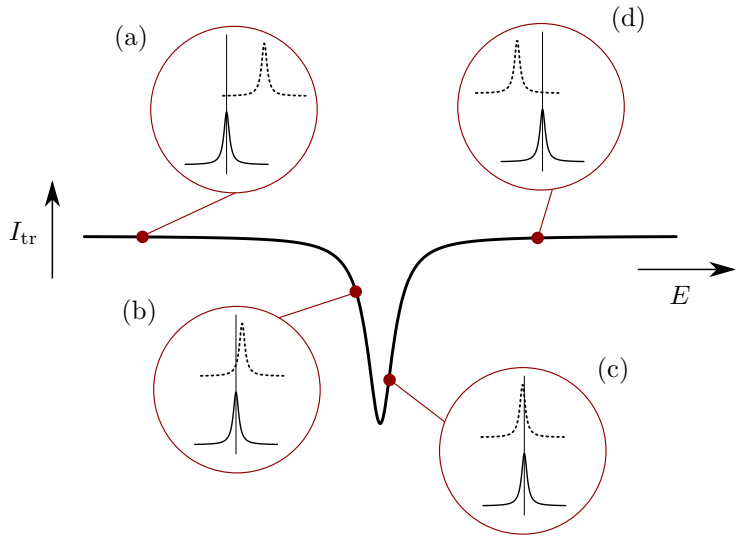

Figure 1.11: Illustration of a selected Mössbauer absorption line. The intensity of the transmitted radiation depends on the relative position of the source emission line (solid lines in the circles) with respect to a given transition energy line (dashed lines). In the resonance (b, c) there is a significant attenuation of the intensity with respect to the off-resonance case (a, d).

Hyperfine splittings caused by electric quadrupole and magnetic hyperfine interactions can be determined, as they are basically given by the relative positions and amplitudes of the corresponding Mössbauer lines, one to each other. On the other hand, the shifts of the nuclear energy levels caused by the $\hat{H}_{\mathrm{I}}$ interaction are related to the lines absolute positions and so they cannot be experimentally obtained. Instead of absolute values, the relative values of the transition energies for each nuclear site are determined with respect to a reference. This is done by a calibration procedure [2], where the Mössbauer spectrum of a reference material is measured and a selected energy point of the spectrum is taken as a reference (zero) point. All measured spectra are then given in a relative energy axis with the origin 0 mm/s corresponding to the reference point. A calibration foil of α-Fe is typically used, where the reference point is the center of the sextet spectrum. The shift of the lines corresponding to a given nuclear site in the sample then determines the isomer shift parameter given by formula (1.24).

There are several practical aspects of the Mössbauer measurements which generally need to be taken into considerations for a correct analysis and interpretation of the results. One of them is a finite width of the source emission line, where the transmitted intensity contributions from different parts of the emission line overlapping with the transition energy lines are simultaneously detected. The theoretical spectrum from (1.43) is then convoluted with the emission line [30], which results in a minimum Mössbauer linewidth of $\sim 2\Gamma$, where $\Gamma = 0.097\,\mathrm{mm/s}$. Another important aspect is the detection of background, where $I_{\mathrm{tr}}(E)$ is increased by a non-resonant contribution arising mainly from higher-energy photons emitted by the source [30]. Finally, the emission of both higher-energy photons and resonant 14.4 keV photons by the radioactive source as well as the nuclear resonant scattering exhibit a statistical character. A sufficiently high intensity (number of counts)

is then required for a proper data evaluation. The time needed for Mössbauer spectra accumulation depends on the source activity, sample effective thickness and properties of the experimental setup. Commonly, the measurements take from several hours up to several days.

1.3.2 Nuclear Forward Scattering

NFS belongs to the group of experimental techniques that utilize modern synchrotron radiation sources. These sources are based on the radiation properties of charged particles (usually electrons) when their speed approaches the speed of light [52]. A schematic illustration of a synchrotron radiation source is shown in Fig. 1.12. First, the particles are accelerated using the linear accelerator and the booster synchrotron. After their acceleration the particles are injected into the accelerator storage ring containing specially designed magnetic structures (undulators are used in NFS). When passing through the generated magnetic field the particles trajectory is being appropriately curved, causing the generation of the resulting coherent radiation with unique energy, time and spatial properties [53].

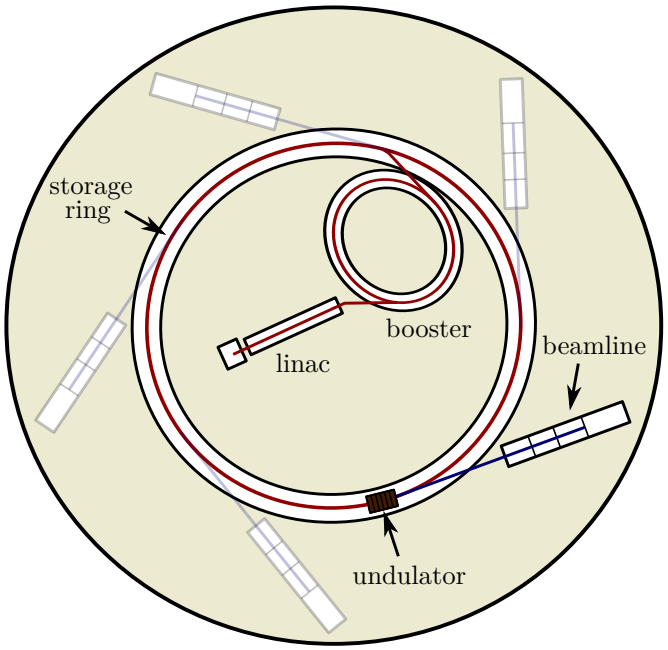

Figure 1.12: Scheme of a modern synchrotron radiation source showing the charged particles accelerated in the linear accelerator (linac) and booster synchrotron, then injected into the storage ring and emitting the radiation when passing through the undulator.

In contrast to "single-line" radioactive sources the synchrotron radiation coming from the undulator exhibits a broad energy distribution of the emitted radiation. Thanks to the wide range of usable energies the nuclear resonance can be observed for a large number of different resonant nuclides [54]. This can be an advantage over TMS where the usable nuclides are limited by the existence of radioactive sources with appropriate nuclear gamma transitions. Another difference from the radioactive sources is that the synchrotron sources generate the radiation which exhibits a high degree of polarization. The radiation is linearly

polarized in the plane of the accelerator storage ring (in NFS the $\vec{\varepsilon}_\sigma$ vector is conventionally chosen to lie in this plane, so the radiation is $\vec{\varepsilon}_\sigma$-polarized).

Time properties of the emitted radiation are crucial for the performance of the NRS experiments. The movement of the charged particles in the storage ring can be realized in a bunch mode. The particles are grouped in several discrete bunches with a specific time separation between them. When passing through the undulator, each bunch generates a separate synchrotron radiation pulse of $\sim 100\,\mathrm{ps}$ time duration. The time separation between individual pulses depends on a given bunch mode and is usually $\sim 10^1$–$10^2\,\mathrm{ns}$.

The principle of NFS is shown in Fig. 1.13. The system of monochromators [11], based on the single-crystal diffraction, is used to select the radiation energy suitable for a given Mössbauer nuclide. The energy bandwidth of the radiation is in the order of eV when coming from the heat-load monochromator and in the meV or sub-meV range when leaving the high-resolution monochromator. However, this is still several orders more than the range of the nuclear transition energies (see Fig. 1.4).

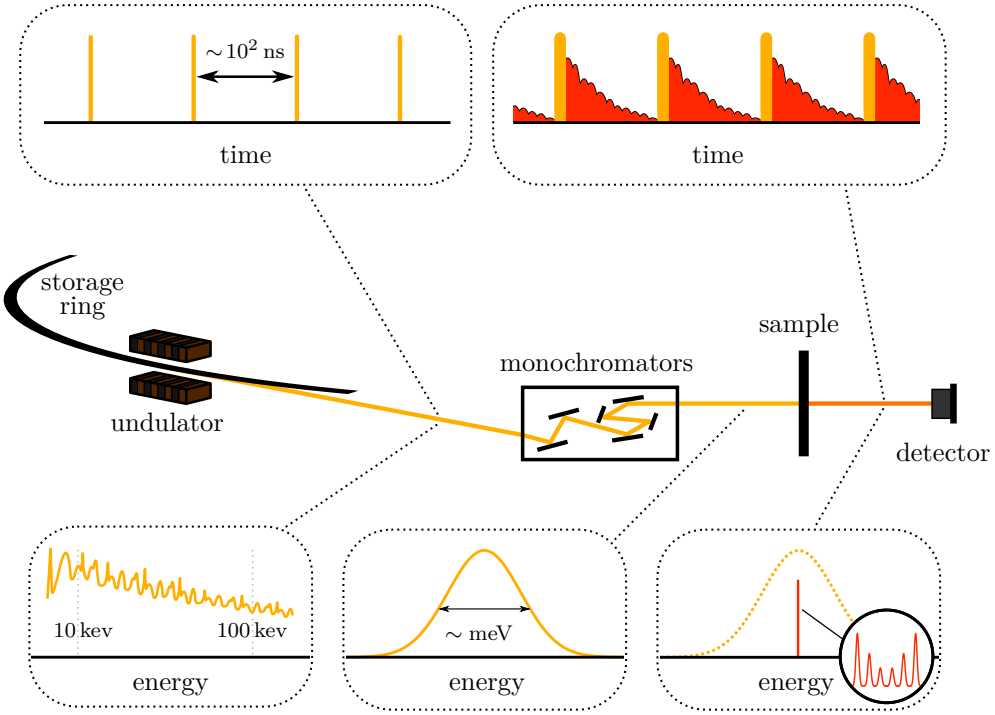

Figure 1.13: NFS experimental arrangement with the energy and time properties of the synchrotron radiation before/after monochromatization and after the scattering.

Instead of separate excitations of the individual nuclear energy levels as in the TMS, the synchrotron radiation pulses cause simultaneous coherent excitations of all the energy levels. During the subsequent deexcitation the radiation fields are emitted, with energies corresponding to differences between the individual ground and excited state energy levels (Fig. 1.14). The superposition of these radiation fields gives the resulting scattered field whose intensity exhibits typical time interference patterns known as quantum beats [55,56].

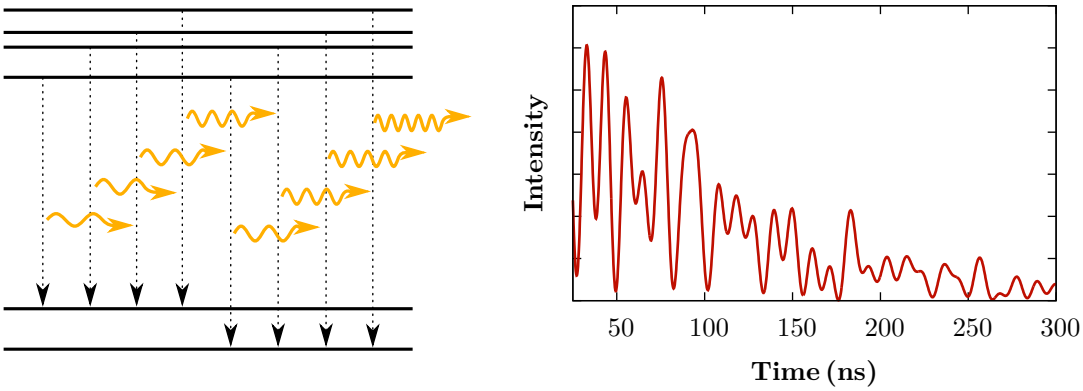

Figure 1.14: Radiation fields corresponding to individual transitions between the nuclear energy levels (on the left). Their superposition results in quantum beats of the detected signal in time domain (on the right).

For the incident radiation in a pure polarization state the transmitted radiation field in the time domain $\vec{A}_{\mathrm{tr}}(t)$ can be obtained by a Fourier transform [34]

$$\vec{A}_{\mathrm{tr}}(t) = \mathcal{F}\left[\vec{A}_{\mathrm{tr}}(E)\right], \tag{1.45}$$

where $\vec{A}_{\mathrm{tr}}(E)$ is the energy-dependent transmitted radiation field from formula (1.37). The energy and time dependence is explicitly written in the brackets to distinguish between the quantities in these two domains. From the linearity of the Fourier transform and formula (1.38) we get

$$\vec{A}_{\mathrm{tr}}(t) = \mathcal{F}\left[\vec{A}_{\mathrm{sc}}(E)\right] + \mathcal{F}\left[\vec{A}_{\mathrm{in}}\right]. \tag{1.46}$$

The first term in (1.46) gives the scattered radiation field in the time domain $\vec{A}_{\mathrm{sc}}(t)$. The second term represents that part of the radiation which does not interact resonantly with the nuclear system. In comparison to the resonant interaction, which takes typically from 10^1 ns to 10^2 ns ($\sim$ lifetime of the nuclei excited state), the non-resonant interaction is significantly faster and represents an initial prompt peak. By gating the prompt peak its time separation from the "delayed" radiation can be realized. Therefore, the detected signal is formed by the resonantly scattered photons only and is described by the scattered radiation intensity $I_{\mathrm{sc}}(t)$ [42]

$$I_{\mathrm{sc}}(t) = \left|\vec{A}_{\mathrm{sc}}(t)\right|^2. \tag{1.47}$$

Analogously to energy-domain measurements, the theory could be generalized for mixed polarization states of the incident radiation described by a density matrix ρ. In agreement with (1.39) and (1.45) the normalised scattered radiation intensity is given by the general formula

$$I_{\mathrm{sc}}(t) = \mathrm{Tr}\left\{\mathcal{F}\left[T - \mathbf{1}\right]\rho\,\mathcal{F}^{\dagger}[T - \mathbf{1}]\right\}. \tag{1.48}$$

Although the experimental data are measured in time domain as time interference patterns (i.e. quantum beats) and do not provide a direct spectral information, a less accurate term "time spectrum" has been established for $I_{\mathrm{sc}}(t)$.

In many aspects, the transmission Mössbauer spectra with absorption lines and the NFS time spectra featuring quantum beats provide equivalent information on the solid systems. However, there are also some differences. This can be demonstrated on the example of the isomer shift determination. It can be found out that time spectra depend only

on the differences $\Delta E_{n_\mathrm{g},n_\mathrm{e}} - \Delta E_{n'_\mathrm{g},n'_\mathrm{e}}$ between different transition energies and not on their absolute values. The same problem was discussed in TMS, where the relative values of the transition energies with respect to a reference (i.e. isomer shift) could be obtained for each nuclear site from a single measurement using the calibration. To perform similar approach in the time domain, the reference time spectrum would have to be measured not once, but for each NFS measurement separately [57]. This is usually not done and for a sample with a single nuclear site the information on its isomer shift is lost. For multiple nuclear sites one of them can be chosen as an inner reference and the isomer shifts of the rest can be determined with respect to it. Other differences between TMS and NFS, related mainly to the thickness effects, will be discussed later in this work.

The synchrotron radiation sources bring a big advantage over conventional Mössbauer sources regarding the intensity. The accumulated NFS time spectra consist of a very high number of contributions from individual synchrotron radiation pulses (coming with $\sim 10^2$ ns period). To highlight the benefits of the synchrotron radiation, the physical quantities of spectral photon flux and brilliance are usually used [11, 58]. The spectral flux is defined as the number of emitted photons per second, normalised to 0.1 % of the radiation energy bandwidth. The brilliance is then given as the spectral flux normalised to a solid angle of 1 mrad^2 and to a source area of 1 mm^2. Basically, higher values of these quantities mean either better statistics within the same measuring time or faster measurement with the same statistics. High brilliance is especially important when studying very small samples requiring high concentration of photons in a small area [59]. The brilliance of the synchrotron radiation is significantly higher (by more than 10 orders) when compared to the radioactive sources.

The usage of synchrotron radiation has opened entirely new possibilities of hyperfine methods. An example is the use of NFS for the investigation of fast processes, including solid-state chemical reactions, structural re-ordering, diffusion or magnetic transformations [60–62]. Such studies are of a high importance from both the basic research perspective (exploring transformation kinetics and mechanisms, discovering temporary inter-phases, etc.) and the possible applications (altering transformation conditions to modify material properties). With the current radiation intensity one time spectrum could be accumulated in less than one minute. Further decrease of the measuring time can be expected with the development of free-electron lasers [58].

1.3.3 Solutions for Simple Cases

The described theory can be significantly simplified when the electric and magnetic hyperfine interactions are not generally combined but follow one of the special cases given in section 1.1.3. In these cases the interaction Hamiltonian (1.17) takes a simple diagonal form. The scattering length $N_{\vec{\varepsilon},\vec{\varepsilon}_\mathrm{in}}$ from (1.29) could be rewritten into the form given for example in [11, 35]

$$N_{\vec{\varepsilon},\vec{\varepsilon}_\mathrm{in}} = \frac{3}{16\pi}\Big[(F_{+1}+F_{-1})(\vec{b}^{\,*}\cdot\vec{b}_\mathrm{in}) - i(F_{+1}-F_{-1})(\vec{b}^{\,*}\times\vec{b}_\mathrm{in})\cdot\vec{z}_0 + \\ + (2F_0 - F_{+1} - F_{-1})(\vec{b}^{\,*}\cdot\vec{m})(\vec{b}_\mathrm{in}\cdot\vec{z}_0)\Big]. \tag{1.49}$$

It depends on the relative directions between the $\vec{\varepsilon}_\mathrm{in}, \vec{\varepsilon}$ and $\vec{k}_0$ unit vectors and the $\vec{z}_0$ unit vector, whose direction corresponds to the quantization axis in which the interaction Hamiltonian is diagonal. For the pure magnetic interactions $\vec{z}_0$ coincides with the direction

of the effective magnetic field. For the electric interactions it coincides with the unit vector $\vec{v}_{zz}$ of the EFG main axis. Considering the M1 transition, $\vec{b}_{\mathrm{in}} = \vec{k_0} \times \vec{\varepsilon}_{\mathrm{in}}$ and $\vec{b} = \vec{k_0} \times \vec{\varepsilon}$. The F_M factors include the scattering dependence on the energy

$$F_M = \sum_{m_{\mathrm{g}}=-j_{\mathrm{g}}}^{j_{\mathrm{g}}} \frac{C^2\left(j_{\mathrm{g}} 1 j_{\mathrm{e}}; m_{\mathrm{g}} M\right)}{E - \Delta E_{m_{\mathrm{g}},\, m_{\mathrm{g}}+M} + i\frac{\Gamma}{2}}\,, \quad M = -1, 0, +1\,. \tag{1.50}$$

Note that the scattering length includes only six possible transitions between the nuclei ground and excited state energy levels. The other two transitions $m_{\mathrm{g}} = 1/2 \leftrightarrow m_{\mathrm{e}} = -3/2$ and $m_{\mathrm{g}} = -1/2 \leftrightarrow m_{\mathrm{e}} = 3/2$ do not satisfy the selection rule for the angular momenta addition $m_{\mathrm{e}} = m_{\mathrm{g}} + M$. Depending on the type of the hyperfine splitting (see Fig. 1.3) for a given nuclear site, the Mössbauer spectra can be divided into those of a single transition ($\hat{H}_{\mathrm{I}}$ interaction, singlet), two transitions ($\hat{H}_{\mathrm{I}} + \hat{H}_{\mathrm{Q}}$ interaction, doublet) and six transitions ($\hat{H}_{\mathrm{I}} + \hat{H}_{\mathrm{M}}$ interaction, sextet). Examples of Mössbauer spectra and corresponding NFS time spectra for the individual transition types is shown in Fig. 1.15. Even for the general combined case ($\hat{H}_{\mathrm{I}} + \hat{H}_{\mathrm{Q}} + \hat{H}_{\mathrm{M}}$ interaction) the two additional transitions are usually suppressed over the other six. They can be measured only under special conditions with comparable quadrupole and magnetic interactions [14].

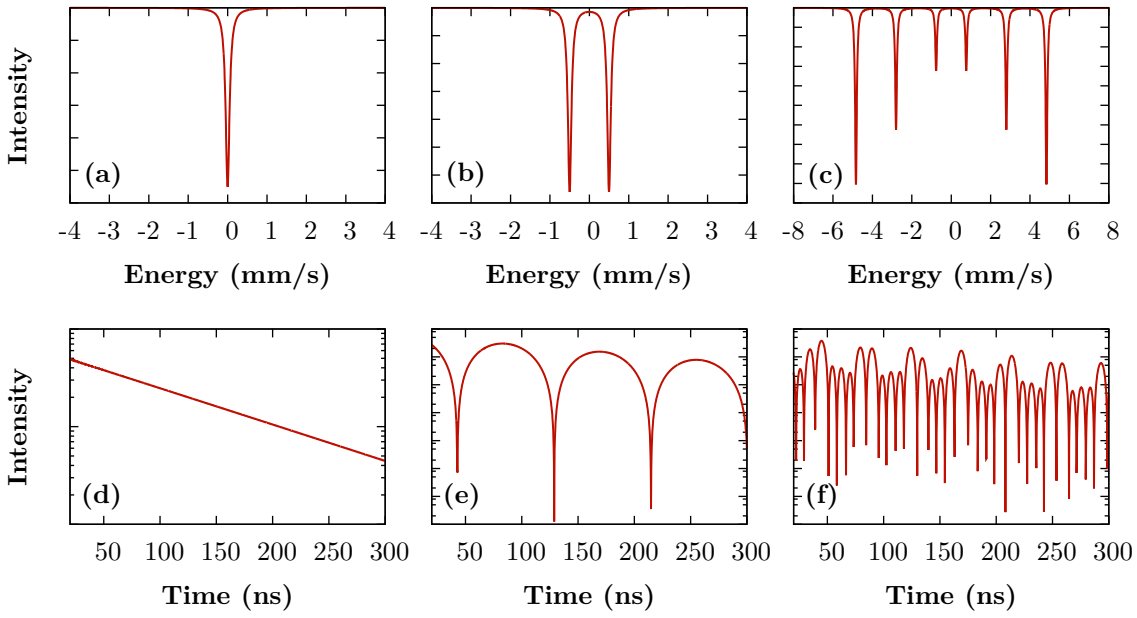

Figure 1.15: Examples of the transmission Mössbauer spectra and the NFS time spectra of singlet (a, d), doublet (b, e) and sextet (c, f). The time spectra are shown in a logarithmic scale.

Another important case is the random orientation of the effective electric and magnetic fields in measured samples. The scattering length matrix can be obtained from (1.41) by integrating over all possible directions

$$N = \int_{\Omega} N(\Omega)\, \mathrm{d}\Omega \tag{1.51}$$

with $N(\Omega)$ given by (1.31) and Ω indicating the orientation dependence. The simplest approach is integration over orientations of the radiation coordinate system with a fixed

sample orientation. Similarly to the rotation of the EFG coordinate system described in section 1.1.3, the radiation coordinate system ($\vec{\varepsilon}_\sigma$, $\vec{\varepsilon}_\pi$ and $\vec{k}$ vectors) can be rotated by Euler angles Φ, Θ, Ψ. Integration over these angles leads to a diagonal form of the scattering length

$$N = \pi \sum_{n_\mathrm{g},n_\mathrm{e}} L_{n_\mathrm{g}}^{n_\mathrm{e}}(E) \sum_{M',M} G_{M'}^{n_\mathrm{g},n_\mathrm{e}} \left(G_M^{n_\mathrm{g},n_\mathrm{e}}\right)^* \begin{pmatrix} 1 & 0 \\ 0 & 1 \end{pmatrix}. \tag{1.52}$$

Let us use the symbol $\mathrm{sc}(N)$ for the scalar value in (1.52). The scattering matrix T is then given as

$$T = \exp\Big[i\,\xi\,\mathrm{sc}(N)\Big] \begin{pmatrix} 1 & 0 \\ 0 & 1 \end{pmatrix}. \tag{1.53}$$

The effect of the random orientation can be demonstrated using an incident radiation in a pure polarization state $\vec{A}_\mathrm{in} = A_{\mathrm{in},\sigma}\vec{\varepsilon}_\sigma + A_{\mathrm{in},\pi}\vec{\varepsilon}_\pi$. The transmitted radiation field $\vec{A}_\mathrm{tr}(E)$ can be calculated as

$$\vec{A}_\mathrm{tr}(E) = T\vec{A}_\mathrm{in} = \exp\Big[i\,\xi\,\mathrm{sc}(N)\Big] \begin{pmatrix} 1 & 0 \\ 0 & 1 \end{pmatrix} \begin{pmatrix} A_{\mathrm{in},\sigma} \\ A_{\mathrm{in},\pi} \end{pmatrix} = \exp\Big[i\,\xi\,\mathrm{sc}(N)\Big]\vec{A}_\mathrm{in} \tag{1.54}$$

and the radiation intensity is

$$I_\mathrm{tr}(E) = \left|\vec{A}_\mathrm{in}\right|^2 \exp\Big[i\,\xi\,\mathrm{sc}(N) - i\,\xi\,\mathrm{sc}^*(N)\Big] = \left|\vec{A}_\mathrm{in}\right|^2 \exp\Big[-2\,\xi\,\mathrm{Im}\big\{\mathrm{sc}(N)\big\}\Big]. \tag{1.55}$$

Clearly, the scattering does not affect the polarization of the incident radiation. Essentially the formula for the transmitted radiation intensity follows the general absorption law with the absorption coefficient proportional to the imaginary part of the scattering length scalar.

In summary, there are many situations where certain symmetries within the scattering system may simplify the scattering problem. Generally, the polarization effects could be omitted from the description and simplified theoretical formalisms could be used [15]. This applies mainly for the Mössbauer spectroscopy with upolarized radiation sources and scattering systems which could be considered as ideally thin ($d_\mathrm{eff} \ll 1$). For significantly thick samples and possible polarization mixing, the usage of more general descriptions should be considered.

1.3.4 Thickness Effects

The impact of the finite (effective) thickness of the scattering system on the measured Mössbauer and time spectra can be demonstrated by expanding the scattering matrix T of the system in a Taylor series

$$T = \mathrm{e}^{i\xi N} = \sum_{l=0}^{\infty} \frac{(i\xi N)^l}{l!} = \mathbf{1} + i\xi N + \frac{(i\xi N)^2}{2} + \frac{(i\xi N)^3}{6} + \dots\,. \tag{1.56}$$

The individual terms in the Taylor expansion correspond respectively to the non-resonant interaction, single scattering, double scattering, etc.

In TMS the transmitted intensity is given by formula (1.43). Using the properties of the matrix trace and the Taylor series we may write

$$\begin{aligned} I_\mathrm{tr}(E) = \mathrm{Tr}\Bigg\{\rho\Big[\mathbf{1} - i\xi N^\dagger + \frac{\left(i\xi N^\dagger\right)^2}{2} - \frac{\left(i\xi N^\dagger\right)^3}{6} + \dots\Big] \\ \times\Big[\mathbf{1} + i\xi N + \frac{(i\xi N)^2}{2} + \frac{(i\xi N)^3}{6} + \dots\Big]\Bigg\}. \end{aligned} \tag{1.57}$$

The individual intensity terms in (1.57) after the expansion can be divided according to the orders of the powers of ξ. The 0-th order consists only of $\mathbf{1}$, the first order terms are $i\xi N - i\xi N^\dagger$, the second order includes $(1/2)\,(i\xi N)^2 - (i\xi)^2\,N^\dagger N + (1/2)(i\xi N^\dagger)^2$, etc. The thin-sample approximation of the intensity is realized by taking only the terms up to the lowest present power of ξ, which in this case is the first order ξ^1. The second-order approximation would be realized by including the second-order terms, third-order approximation by including the third-order terms, etc. More detailed evaluation of the expanded transmitted intensity and its terms will be provided in the next chapters.

In the first-order approximation the energy dependence is basically given by the real Lorentzian functions taken as the imaginary part of $L^{n_\mathrm{e}}_{n_\mathrm{g}}(E)$. These Lorentzian dependences form the basic form of the Mössbauer lines. As the effective thickness (see formula (1.36)) increases the higher orders of $I_\mathrm{tr}(E)$ start to significantly influence the Mössbauer lines so they can no longer be considered as Lorentzian. Instead, there is an increasing contribution from the "higher-order Lorentzian" functions, which results in the broadening of the Mössbauer lines (Fig. 1.16a).

In simplified cases the line broadening due to the thickness can be approximately modelled by distributions of hyperfine parameters. However, the thickness effects generally do not alter only the line-shapes. This can be illustrated on an example of the Mössbauer lines ratios [63]. Considering a system of polycrystalline α-Fe foil with the well-distinguished magnetic hyperfine splitting, the corresponding Mössbauer spectrum could be calculated, for example, using the simplified formulas (1.49) and (1.55). In the thin-sample approximation the amplitudes of the absorption lines follow the 3:2:1:1:2:3 ratios, which are typical for the randomly oriented magnetic fields in the system. Deviations from these ratios may usually be ascribed to additional nuclear sites in the sample or to preferentially oriented magnetic fields, which will be described in chapter 3. However, for thicker samples the amplitudes of the outer lines decrease with respect to the inner lines. This can be seen in Fig. 1.16a, where the decrease is apparent for the effective thickness of ~ 10, which corresponds to $30\,\mu$m thick α-Fe foil at room temperature with natural ^{57}Fe abundance.

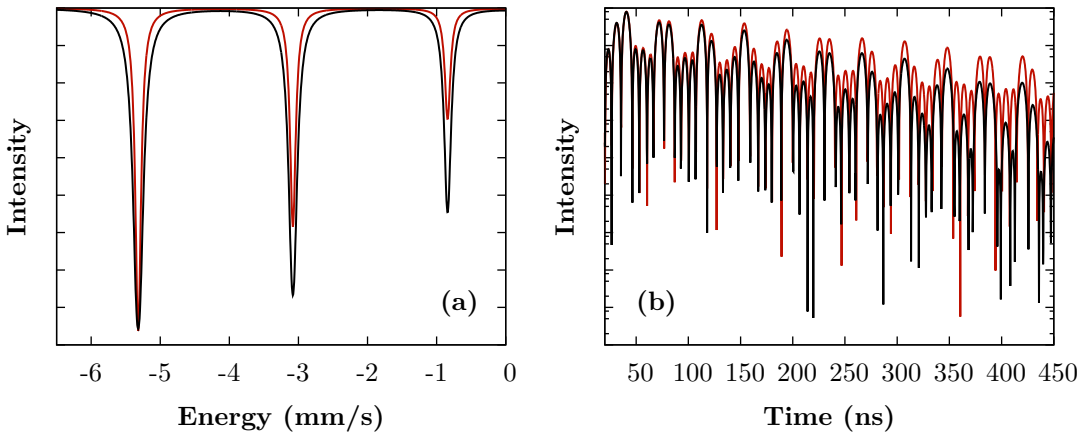

Figure 1.16: (a) First three absorption lines of a Mössbauer spectrum of polycrystalline α–Fe with the natural ^{57}Fe abundance and the thickness of $1\,\mu$m (red line) and $30\,\mu$m (black line). (b) Corresponding NFS time spectra in a logarithmic scale. The $30\,\mu$m sample exhibits a speed-up effect, which can be seen as a steeper slope of the time decay. The presented data were simulated for linearly polarized incident radiation.

Thickness effects in time domain are strongly connected to the coherence of the scattering process [64, 65]. Rather than scattering on a single nucleus the whole nuclear system is coherently excited. The following deexcitation then exhibits a speed-up effect, where the increasing effective thickness results in shorter deexcitation times (Fig. 1.16b). Even for the unsplit nuclear energy levels the photon emission does not follow the exponential decay with the lifetime of the excited state, as would be the case for the excitation of a single nucleus. The emission proceeds faster, the exponential time dependence is being pushed towards the lower times and exhibits beating patterns. These patterns are similar to the quantum beats, but arise from the multiple scattering and are referred to as dynamical beats. For the split energy levels the superposition of the dynamical beats with the quantum beats may occur, which results in a more complex time dependence described as the hybrid beats [66].

The Taylor expansion of the scattering matrix could also be used for the time spectra description. Using formula (1.48) and linearity of the Fourier transform the scattered radiation intensity could be written as

$$\begin{aligned} I_{\mathrm{sc}}(t) = \mathrm{Tr}\Bigg\{ \rho \Bigg[-i\xi \mathcal{F}^{\dagger}[N] + \frac{(i\xi)^2 \mathcal{F}^{\dagger}[N^2]}{2} - \frac{(i\xi)^3 \mathcal{F}^{\dagger}[N^3]}{6} + \dots \Bigg] \\ \times \Bigg[i\xi \mathcal{F}[N] + \frac{(i\xi)^2 \mathcal{F}[N^2]}{2} + \frac{(i\xi)^3 \mathcal{F}[N^3]}{6} + \dots \Bigg] \Bigg\}. \end{aligned} \tag{1.58}$$

The thin-sample approximation is again described by terms with the lowest order of ξ. In NFS it is the second-order term $-(i\xi)^2 \rho \mathcal{F}^{\dagger}[N] \mathcal{F}[N]$. Consequently, NFS exhibits a different sensitivity to the effective thickness than TMS.

1.3.5 Data Evaluation

For obtaining quantitative information on nuclear sites in a sample and their hyperfine parameters the experimental data are compared to a theoretical curve, which is calculated for a selected model of the sample. The most widespread approach is the least squares fitting, where the best statistical agreement between the measurement and the theory is achieved by minimizing the χ^2 parameter given as [67]

$$\chi^2 = \sum_{l=1}^{L} \frac{\left(I_l^{\mathrm{ex}} - I_l^{\mathrm{th}} \right)^2}{\sigma_l^2}, \tag{1.59}$$

where I_l^{ex} are the intensities detected at individual energy/time points (experimental data) and I_l^{th} are the calculated intensities at the corresponding points (theoretical data). The squared differences of the experimental and theoretical data are weighted by the standard deviation squared σ_l^2, which is usually estimated as I_l^{ex}. The χ^2 parameter is often given in a normalized form obtained by dividing (1.59) by a degree of freedom, which is the total number of data points L decreased by the number of fitted parameters.

One of the drawbacks of the least squares fitting is the requirement for a good initial estimate of the fitted parameters. If the initial theoretical curve differs too much from a measured spectrum the optimization procedure may not converge or converges only to a local minimum. This represents a relatively smaller problem in TMS, where the estimation is based (to a large extent) on the positions of measured Mössbauer lines, which reflect

the nuclear transition energies very well. Nevertheless, the Mössbauer spectra fitting is generally not an easy task as individual nuclear sites may significantly overlap, distributions and thickness effects may cause additional line broadening, etc. The fitting becomes more difficult as the complexity of the sample and the number of fitted parameters increase. The fitting is significantly more complicated in the time domain. Thanks to the coherent superposition of the radiation fields coming from individual nuclear transitions and also the superposition of the quantum and dynamical beats the estimation of individual nuclear sites and their hyperfine splitting from the measured time spectra is extremely difficult [66].

There have been demands for novel optimisation approaches to simplify the evaluation of TMS and NFS experimental data. Initial estimations of parameters using the Monte Carlo methods, selection of sample models based on the Fourier transform of experimental data, implementation of artificial neural networks and genetic algorithms are few options worth mentioning [67–70]. The further improvements of the data analysis show to be very important for both the Mössbauer and the synchrotron radiation NRS community.

Many efforts have also been given to the automation and fastening of the data evaluation. This becomes crucial in the NFS studies of fast processes, where one experiment may consist of hundreds of measured time spectra (even larger data sets are to be expected in the future) [71]. A sequential fitting procedure, based on connecting the neighbouring time spectra via their input and output parameter values, has been presented as a usable approach [72]. By connecting the conventional fitting software CONUSS with a specially developed package Hubert the efficiency of the experimental data evaluation was considerably increased [73, 74].

A separate description could be dedicated to special methodologies created for specific requirements depending on the type of information that is being extracted from the carried experiments, e.g. measurements of Lamb-Mössbauer factors, magnetic responses to external fields or texture [28, 41, 75].

2 Violation of Rotational Invariance by Inhomogeneous Systems

A novel methodology for investigating the material inhomogeneities by nuclear resonant scattering techniques is presented in this chapter. The introduced approach is based on the rotational invariance and its violation, which was experimentally observed in the NFS experiments conducted for two different geometrical arrangements. Comparison of the obtained results allows to extract a unique information on the spatial distribution of nuclei featuring different hyperfine interactions, along the direction of the incident radiation.

Differences in the measured time spectra were observed upon a specific sample rotation. Similar phenomena were observed in the past within the studies of fundamental properties of scattering, such as "polarization rotation" (Faraday rotation), time-reversal invariance or reciprocity [32,76]. These properties and conditions for their observation/violation could be explored by ensuring well-conceived experimental conditions (e.g. combination of two absorbers, application of external magnetic fields). This work focuses on the phenomenon of rotational invariance, whose violation was observed without any artificially introduced experimental conditions, solely as a result of the inner properties of the studied sample.

As an outcome, a simple method for identifying the presence of inhomogeneities in the bulk of a solid has been described. It is noteworthy that possibilities to experimentally observe bulk inhomogeneities of hyperfine interactions are limited [77–79]. To the author's knowledge, such a similar observation on the real samples interpreted on the basis of rotational properties of NRS has not been reported in the literature. Despite exhibiting certain limitations regarding specific conditions imposed on the samples, the presented approach could be an inspiration for further developments. This might potentially lead to even more complex reconstruction of material inhomogeneities via an imaging technique.

The first section of this chapter is devoted to the theoretical description of rotational invariance and its connection to spatial distribution of hyperfine interactions. Conditions for observing the inhomogeneities are also determined and interpreted from the physical point of view. The second section provides an experimental demonstration of the described approach. NFS experiments conducted on a metallic glass sample provided information on the magnetic inhomogeneities. This information became accessible by comparing two sets of time spectra, measured at room temperature and during an isothermal annealing. The chapter is concluded by a general discussion of the achieved results.

2.1 Theoretical Description

2.1.1 Rotational Invariance and Homogeneous Systems

The concept of rotational invariance generally refers to situations in which the radiation intensity is not influenced by rotating the scattering system with respect to the radiation coordinate system[3]. This work is specifically focused on the 180 ° rotation around one of the polarization axes defined by the unit vectors $\vec{\varepsilon}_\sigma$ and $\vec{\varepsilon}_\pi$ (see Fig. 2.1). We also assume that the incident radiation is either unpolarized or fully linearly polarized along one of the polarization axes.

[3]More accurately, we use the concept of magnitude rotational invariance, which does not reflect changes in the phase of the radiation. However, the term "magnitude" will be omitted in the following description.

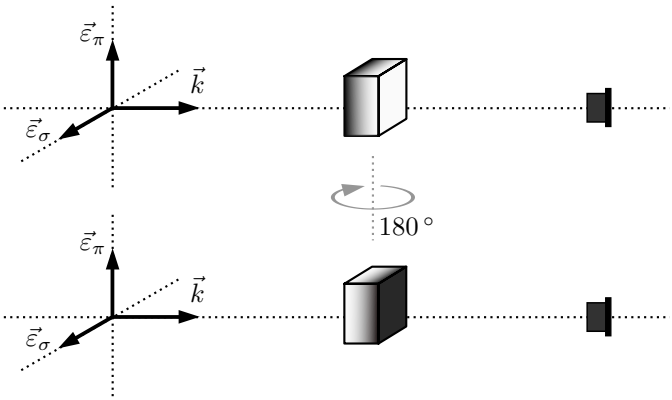

Figure 2.1: Geometrical arrangements used for the study of rotational invariance. The scattering system is rotated around one of the polarization axes (rotation around $\vec{\varepsilon}_\pi$-axis is illustrated in the figure) and experimental data obtained before and after the rotation are compared.

First, let us examine the rotational invariance for a scattering system with nuclear sites homogeneously distributed along the direction of the incident radiation[4]. The scattering length of the system is given by formulas (1.31–1.33) and (1.40). It is convenient to extract the radiation-dependent term from the sum over all present nuclear sites

$$N_{\nu\mu} = \sum_{M,M'} \left[\vec{\varepsilon}_\nu^{\,*} \cdot \vec{Y}_{M'}(\vec{k})\right] \left[\vec{Y}_M^{\,*}(\vec{k}) \cdot \vec{\varepsilon}_\mu\right] \sum_i w_i \, F^{(i)}_{M',\,M}, \tag{2.1}$$

where $F^{(i)}_{M',\,M}$ includes the energy dependences and $G_M^{n_\mathrm{g},n_\mathrm{e}}$ factors of the i-th nuclear site. The radiation coordinate system can be rotated instead of the scattering system. For example, rotating around the original $\vec{\varepsilon}_\pi$-axis by 180 ° causes substitutions in (2.1) according to Fig. 2.2. It can be found that the vector spherical harmonics $\vec{Y}_M$ transform to $-\vec{Y}_M$ and the "rotated" scattering length N^rot can be expressed using the elements of the original scattering length N as

$$N^\mathrm{rot} = \begin{pmatrix} N_{\sigma\sigma} & -N_{\sigma\pi} \\ -N_{\pi\sigma} & N_{\pi\pi} \end{pmatrix}. \tag{2.2}$$

Moreover, the relation between N and N^rot defined by formula (2.2) holds for arbitrary powers of N and N^rot. Therefore, the scattering matrix T^rot transforms in the same way with respect to T and the 180 ° rotation changes only the sign of the off-diagonal scattering matrix elements. The identical results could be obtained for the rotation around $\vec{\varepsilon}_\sigma$-axis. These two rotations around individual polarization axes are equivalent. They differ only by additional 180 ° rotation around $\vec{k}$-axis, which does not affect the scattering length.

For the considered polarization states of the incident radiation the intensity of the transmitted (scattered) radiation depends only on the magnitudes of the scattering matrix elements. The changes in the phase of the off-diagonal matrix elements do not influence the intensity, which means that the rotational invariance is always satisfied for the case of homogeneous scattering systems. Consequently, measuring the violation of rotational invariance (VRI) may potentially provide information on the system inhomogeneities. For example, it may reveal that the studied system is not fully homogeneous. In the following

[4]Spatial distribution of nuclear sites in the plane perpendicular to the direction of the incident radiation is related to the transverse coherence effects and will not be treated in this work [80].

part the connection between VRI and the inhomogeneities, as well as the conditions for its observation, will be examined.

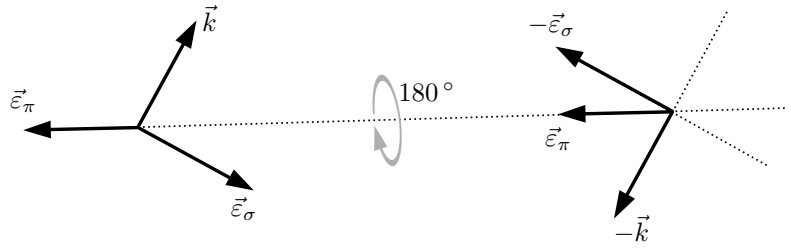

Figure 2.2: Rotation of the radiation coordinate system around $\vec{\varepsilon}_\pi$-axis causing transformations $\vec{\varepsilon}_\sigma \to -\vec{\varepsilon}_\sigma$, $\vec{\varepsilon}_\pi \to \vec{\varepsilon}_\pi$ and $\vec{k} \to -\vec{k}$ in the scattering length N.

2.1.2 Scattering on Multilayers

The inhomogeneous spatial distribution of nuclear sites in a sample causes the total scattering length to be a general function of the sample depth along the radiation direction. For being able to demonstrate the role of inhomogeneities a system consisting of n separately homogeneous layers will be considered [11]. The spatial separation of the nuclear sites into individual layers described by ξ_i and N_i $(i = 1, 2, \ldots, n)$ allows to generalize the scattering matrix of the system and discuss the effects of rotation.

The construction of the scattering matrix can be demonstrated for an incident radiation $\vec{A}_{\text{in}}$ in a pure polarization state. When the radiation passes through the first layer the transmitted radiation field is given as $\vec{A}_1 = T_1\vec{A}_{\text{in}}$, where $T_1 = \mathrm{e}^{i\,\xi_1 N_1}$ is the scattering matrix of the first layer. In general, each layer is described by its own scattering matrix $T_i = \mathrm{e}^{i\,\xi_i N_i}$. As the radiation $\vec{A}_1$ passes through the second layer it acts as an incident radiation on this layer and therefore $\vec{A}_2 = T_2\vec{A}_1 = T_2T_1\vec{A}_{\text{in}}$. The same procedure can be applied analogously for all remaining layers. After passing through the whole system, the transmitted radiation field is given as

$$\vec{A}_{\text{tr}} = T_nT_{n-1}\ldots T_2T_1\vec{A}_{\text{in}}. \tag{2.3}$$

Comparison of formula (2.3) with (1.37) shows that the same theoretical description that was used for the homogeneous samples can be applied here, if the total scattering length T is taken as a multiplication of individual partial scattering matrices (Fig. 2.3).

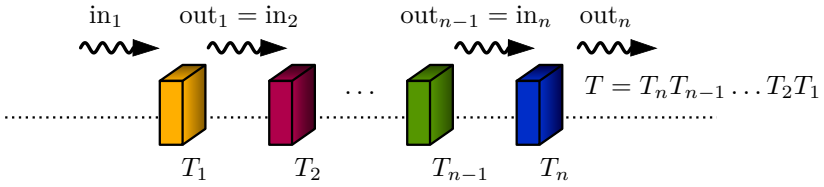

Figure 2.3: An illustration of a scattering system consisting of n layers. The radiation field, which is transmitted through the jth layer described by T_j, is the incident radiation field for the following layer, i.e. $\text{out}_j = \text{in}_{j+1}$.

Mathematically, the rotation of the multilayered system by 180 ° is equivalent to mutual interchanges of the layers followed by a separate rotation of each layer (Fig. 2.4). The total scattering matrix of the rotated system takes the form

$$T^{\mathrm{rot}} = (T_n T_{n-1} \dots T_2 T_1)^{\mathrm{rot}} = T_1^{\mathrm{rot}} T_2^{\mathrm{rot}} \dots T_{n-1}^{\mathrm{rot}} T_n^{\mathrm{rot}}, \tag{2.4}$$

where the T_i^{rot} matrices follow the same relation with respect to T_i which was given for homogeneous samples, see formula (2.2). Whether the system exhibits VRI or not depends on the relation between T and T^{rot}, which is, however, determined by relations between the scattering lengths of individual layers N_i, N_j $(i, j = 1, 2, \dots, n$ and $i \neq j)$. Various criteria may be chosen to examine the properties of N_i and their connection to rotational properties of the scattering system. In this work the commutativity of the scattering lengths is analysed. The reasons for choosing this criterion will be clarified later in this chapter.

We shall consider an illustrative example of a two-layered scattering system. If N_1 and N_2 satisfy the commutation relation $N_1 N_2 = N_2 N_1$ than the scattering matrices T_1 and T_2 follow the same relation, as their exponents commute. Therefore, the total scattering matrix can be written as a single exponential

$$T = \mathrm{e}^{i(\xi_1 N_1 + \xi_2 N_2)}, \tag{2.5}$$

which is analogous to the scattering matrix of a system consisting of two homogeneously distributed nuclear sites, see formulas (1.35) and (1.40). Furthermore, it could be found that the rotated scattering matrices T_1^{rot} and T_2^{rot} also commute and

$$T^{\mathrm{rot}} = \mathrm{e}^{i\left(\xi_1 N_1^{\mathrm{rot}} + \xi_2 N_2^{\mathrm{rot}}\right)}. \tag{2.6}$$

The exponents in (2.5) and (2.6) differ only in the signs of their off-diagonal elements and so the same relation between T and T^{rot} as in the case of a homogeneous scattering system is obtained. Consequently, VRI cannot be observed if the individual scattering lengths mutually commute. In other words, noncommutativity of the scattering lengths is a necessary condition for VRI.

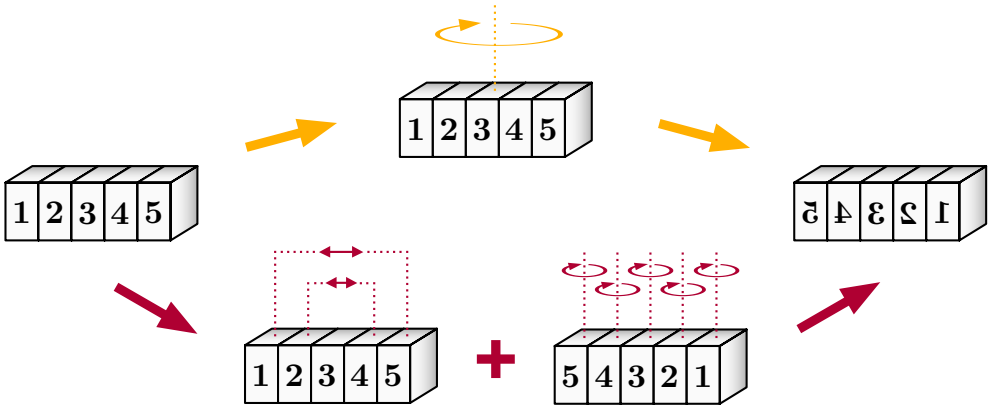

Figure 2.4: A scheme showing the equivalence between the rotation of the multilayered system (upper part) and the interchange of individual layers with respect to the system center, followed by a separate rotation of each layer (lower part).

2.1.3 Texture and Multiple Scattering Effects

The physical meaning of the noncommutativity condition is closely related to rotational distributions of hyperfine parameters. A special case of random electric or magnetic field orientations was treated in section 1.3.3, where the scattering length could be simplified into a unit matrix multiplied by a constant. Therefore, for a multilayered system with all its layers exhibiting randomly oriented fields, the scattering lengths N_i would be proportional to unit matrices. Clearly, in such a case all the scattering lengths would commute and so the magnetically and electrically random layers cannot contribute to VRI. This brings up another physical condition on the scattering system, along with the inhomogeneous spatial distribution of nuclear sites. The observation of VRI is possible only if the inhomogeneous system exhibits a preferential orientation of the electric and/or magnetic field, i.e. texture. Presumably, the condition on the presence of texture in samples can be applicable not only to multilayers but to arbitrary inhomogeneous materials.

Based on the previous statements, the inhomogeneities of hyperfine interactions that allow the observation of VRI can be classified into three basic cases. The first one includes inhomogeneities of the magnitudes of corresponding hyperfine parameters (e.g. magnitude of hyperfine magnetic field) in the presence of homogeneous texture. The second case are the inhomogeneities of texture with homogeneous magnitudes. The last case is the combination of the previous two, where both magnitudes and orientations are inhomogeneously distributed along the direction of the incident radiation. Illustrative examples of all the three cases are shown in Fig. 2.5. For simplicity, the directional inhomogeneities (Fig. 2.5b) will be used as a model example for the next part.

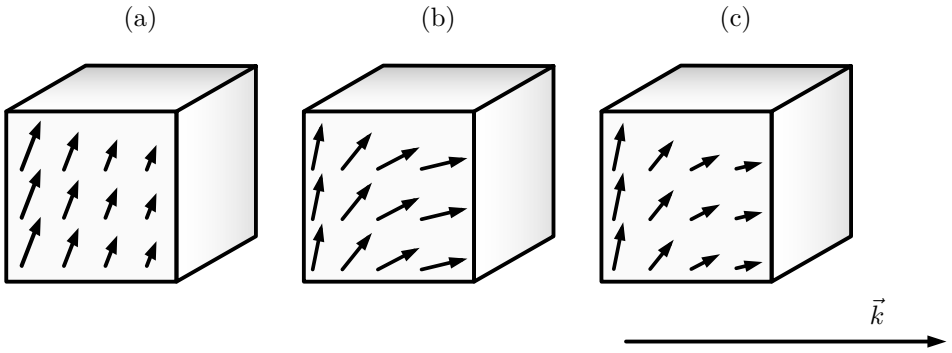

Figure 2.5: Examples of inhomogeneously distributed hyperfine interactions, e.g. magnitudes and directions of hyperfine magnetic fields, along the direction of the incident radiation. Inhomogeneities in (a) magnitudes, (b) orientations and (c) magnitudes and orientations simultaneously may occur in the scattering system.

The observation of VRI shows to be strongly related to thickness effects. This can be demonstrated using a two-layered magnetic system with specific orientations of the magnetic fields (Fig. 2.6). All the resonant nuclei in both layers, denoted as A and B, exhibit hyperfine magnetic fields of the same magnitude. The field directions for nuclei in layers A and B are given by unit vectors $\vec{m}_{\mathrm{A}}$ and $\vec{m}_{\mathrm{B}}$, respectively. Except for the field directions, the two layers are identical.

As the electric interactions are not considered for the given example, the scattering lengths N_{A} and N_{B} of layers before the rotation (Fig. 2.6a) can be calculated using the simplified formulas (1.49) and (1.50)

$$N_{\mathrm{A}} = \frac{3}{16\pi}\begin{pmatrix} F_{+1}+F_{-1} & i(F_{+1}-F_{-1}) \\ -i(F_{+1}-F_{-1}) & F_{+1}+F_{-1} \end{pmatrix}, \tag{2.7}$$

$$N_{\mathrm{B}} = \frac{3}{16\pi}\begin{pmatrix} 2F_0 & 0 \\ 0 & F_{+1}+F_{-1} \end{pmatrix}. \tag{2.8}$$

It could be found out that the scattering lengths do not commute. This is ensured by the off-diagonal matrix elements of N_{A}. If the two matrices were both diagonal than the commutativity would be satisfied and VRI could not be observed. From the physical perspective this is related to polarization mixing phenomena. A demonstration can be shown, for example, for an incident radiation linearly polarized along the $\vec{\varepsilon}_\sigma$ axis. When the radiation passes first through layer B (Fig. 2.6b) the resulting radiation hitting layer A is still $\vec{\varepsilon}_\sigma$-polarized. In the second geometrical arrangement (Fig. 2.6a) the radiation transmitted through layer A exhibits an orthogonal scattering which results in a non-zero $\vec{\varepsilon}_\pi$-component of the radiation field. Put simply, the polarization felt by layer B after passing through layer A is not the same as the polarization felt by layer A after passing through layer B. Consequently, the resulting polarization state after passing through the whole system is not the same for the two arrangements. Generally, it could be stated that VRI is always accompanied by the polarization effects during the scattering.

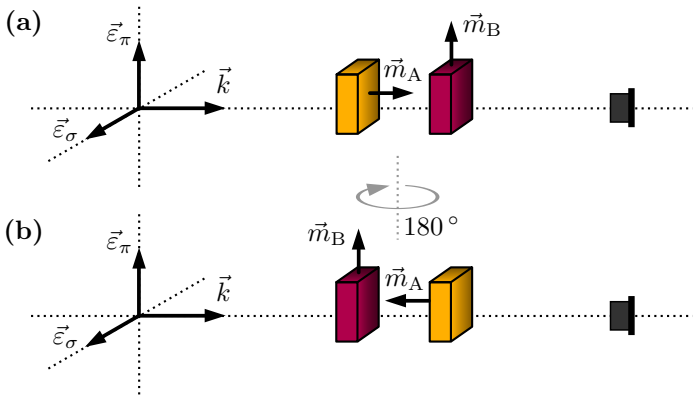

Figure 2.6: A two-layered scattering system with magnetic inhomogeneities introduced as different directions of the hyperfine magnetic field, given by unit vectors $\vec{m}_{\mathrm{A}}$ in layer A and $\vec{m}_{\mathrm{B}}$ in layer B.

The exponentials of N_{A} and N_{B} can be calculated analytically and the resulting scattering matrices of the layers are

$$T_{\mathrm{A}} = \mathrm{e}^{iK(F_{+1}+F_{-1})}\begin{pmatrix} C & -S \\ S & C \end{pmatrix}, \tag{2.9}$$

$$T_{\mathrm{B}} = \begin{pmatrix} \mathrm{e}^{i\,2KF_0} & 0 \\ 0 & \mathrm{e}^{iK(F_{+1}+F_{-1})} \end{pmatrix}, \tag{2.10}$$

where $C = \cos\left[K(F_{+1}-F_{-1})\right]$, $S = \sin\left[K(F_{+1}-F_{-1})\right]$ and $K = (3\xi)/(16\pi)$. The total scattering matrix of the system is then

$$T = T_{\mathrm{B}}T_{\mathrm{A}} = \begin{pmatrix} C\mathrm{e}^{iK(F_{+1}+2F_0+F_{-1})} & -S\mathrm{e}^{iK(F_{+1}+2F_0+F_{-1})} \\ S\mathrm{e}^{i2K(F_{+1}+F_{-1})} & C\mathrm{e}^{i2K(F_{+1}+F_{-1})} \end{pmatrix}. \tag{2.11}$$

From the relation between rotated and non-rotated scattering lengths (and scattering matrices) given by formula (2.2), one can find out that $T_{\mathrm{A}}^{\mathrm{rot}}$ and $T_{\mathrm{B}}^{\mathrm{rot}}$ after the rotation (Fig. 2.6b) are given as a transpose of T_{A} and T_{B}, respectively. The rotated scattering matrix $T^{\mathrm{rot}} = T_{\mathrm{A}}^{\mathrm{rot}} T_{\mathrm{B}}^{\mathrm{rot}}$ is then also a transpose of T. As a result, there is a significant difference between T and T^{rot} which makes the measuring of VRI for such a two-layered system possible.

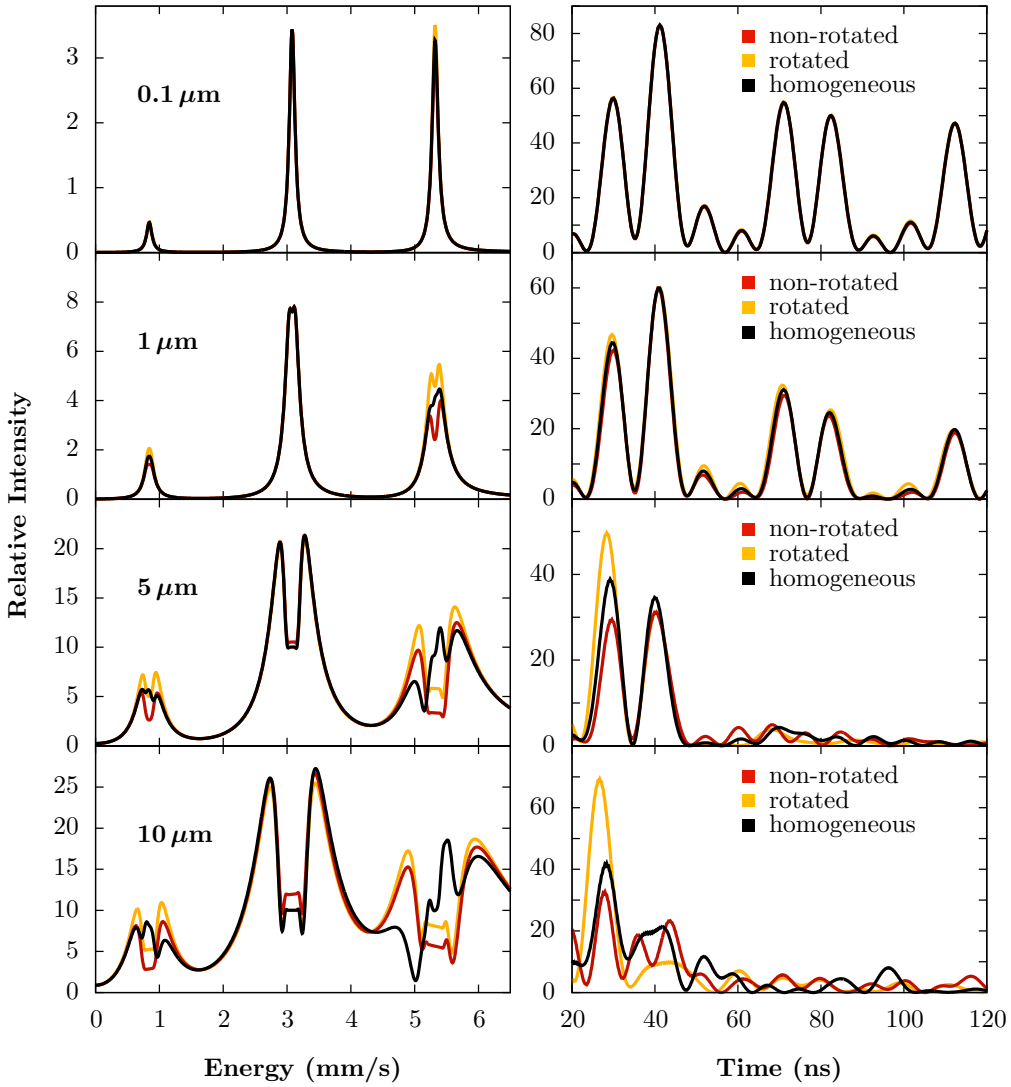

Figure 2.7: Simulated time spectra (on the right) and corresponding scattered radiation intensities in energy domain (on the left), corresponding to the three different arrangements of the considered two-layered system. The differences among the data increase with increasing thickness as a result of multiple scattering.

Fig. (2.7) shows the calculated intensities of the scattered radiation for the two-layered system. The data were simulated for fully $\vec{\varepsilon}_\sigma$-polarized incident radiation and they are presented in both the energy[5] and the time domain. In addition to the two geometrical

[5]In contrast to transmission Mössbauer spectra the curves presented in the figure describe the energy dependence of the scattered radiation field intensity.

arrangements from Fig. 2.6, the third case representing a mixture of A and B into one homogeneous layer is shown for comparison. The parameters of α-Fe (with all nuclei being ^{57}Fe) at room temperature were used for the data simulations [29, 81]. The intensities are compared for different total thicknesses ranging from $0.1\,\mu$m to $10\,\mu$m.

The simulations clearly demonstrate the role of thickness effects. The differences among the spectra become more significant as the thickness of the layers increases. On the other hand, for very thin samples the three described cases give basically identical results and VRI is suppressed. This observation can be explained as a consequence of the multiple scattering. The exact mathematical description of this effect for the considered experimental arrangement is provided in appendix A. The differences between the radiation intensities before and after the $180\,^\circ$ rotation arise from the multiple-scattering terms which include the scattering on both system layers. Contributions from the single scattering or from the multiple scattering in only one of the layers are invariant under the given rotation of the system. For samples with a high effective thickness the non-invariant contributions are considerable. As the effective thickness decreases these contributions become negligible with respect to the invariant ones. Consequently, those contributions to spectra which reflect the system inhomogeneities vanish in the thin-sample limit and the rotational invariance is satisfied.

Observation of VRI depends not only on the scattering system properties but also on given experimental arrangement. This can be demonstrated by using unpolarized radiation for the interaction with the described two-layered system and by measuring the Mössbauer transmission. In contrast to the linearly polarized radiation, where VRI is clearly visible for relatively thick samples (see Fig. 2.7), the unpolarized radiation prevents its observation regardless of the thickness. The calculation based on (1.43) gives the transmitted radiation intensity in the form $\sum_{\mu\nu} |T_{\mu\nu}|^2$ where $\mu, \nu \in \{\sigma, \pi\}$. The sum runs over all matrix elements of T and for the scattering matrix (2.11) the resulting intensity is the same as for its transpose, which is equal to T^{rot} in the given example.

2.2 Experiments of Nuclear Forward Scattering

The following part reports on the observation of VRI by NFS of synchrotron radiation. The experiments were conducted on an iron-based metallic glass, specially treated via a process of ion irradiation [82]. Investigation of such materials is of a high interest, for example, due to their possible use in radiofrequency cavities of accelerators. The knowledge on their influence by an irradiation exposure is important for a proper performance of these complex instruments. Exploring the mechanisms of the ion interactions in a solid is also interesting from the fundamental research perspective.

Investigations of the ion-treated solid materials can be realized for various irradiation conditions, including the selected types of accelerated ions, their energy and also fluency (number of incident ions per unit area). A series of experiments were conducted on the investigated metallic glass to study the effect of ion irradiation on the subsequent crystallization process. For this work, selected experiments from the series were chosen to demonstrate the previously described effects and their experimental feasibility.

2.2.1 Metallic Glass Sample and Experimental Arrangement

The composition of the studied metallic glass was $Fe_{81}Mo_8Cu_1B_{10}$ with around 50 % of the iron atoms being in the form of ^{57}Fe. The sample was prepared by a melt-spinning

technique as approximately 20 μm thick and 1 mm wide ribbons [83]. The preparation conditions resulted in two physically and chemically different ribbon surfaces, also denoted as "wheel side" and "air side". The wheel side was in contact with the spinning wheel during the cooling of the melt, whereas the air side was in contact with the surrounding atmosphere [84].

The prepared ribbons in as-quenched state were irradiated by N^+ ions with the energy of 130 keV. In all the cases the sample was exposed to the N^+ ions from the air side. The experiments presented in this work were conducted on the ribbons which exhibited the ion irradiation fluency of $2.5 \cdot 10^{17}$ ions/cm^2. Despite the relatively low energy of ions the irradiation was sufficient for affecting the bulk magnetic properties of the sample [82].

The experiments were carried out at ID18 beamline in ESRF (European Synchrotron Radiation Facility). Synchrotron radiation beam with the mean energy of 14.4 keV and bandwidth of 1 meV was used. The radiation was linearly polarized in the plane of the storage ring ($\vec{\varepsilon}_\sigma$-polarized). During the NFS measurements the sample was fixed on a stable vertical holder placed inside a vacuum furnace. For selecting the sample orientations with respect to the radiation coordinate system, distinguishing between the two sides of ribbons was important. The measurements were carried out for two orientations (air-side and wheel-side orientations) differing by the 180 ° rotation of the sample with respect to the $\vec{\varepsilon}_\pi$-axis (Fig. 2.8).

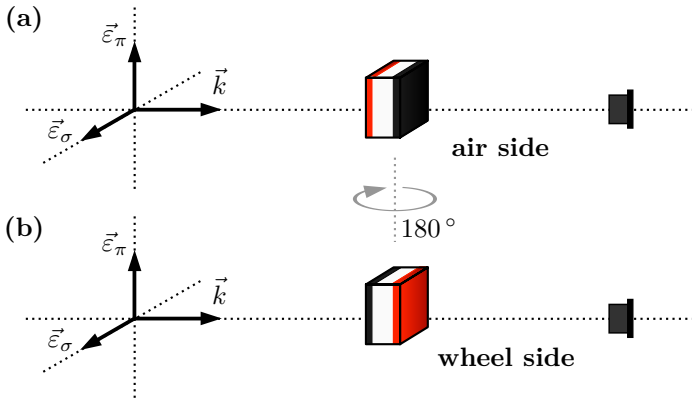

Figure 2.8: Two geometrical arrangements used for the NFS experiments. (a) Air-side orientation with the air side of the ribbon facing the detector. (b) Wheel-side orientation with the wheel side facing the detector and the air side oriented towards the incident radiation.

Each experiment consisted of three basic parts. First, one NFS time spectrum of the sample was measured for 5 minutes at room temperature, prior to any thermal treatment. After the room-temperature measurement the sample was heated within three minutes up to 300 °C. This temperature was kept for about one hour and during the isothermal annealing the time spectra were acquired for each three minutes. The sample was then spontaneously cooled to room temperature and another time spectrum was measured. Fig. 2.9 shows a scheme of the NFS experiments and a typical evolution of measured time spectra. The time spectra presented in the figure correspond to the air-side orientation of the sample.

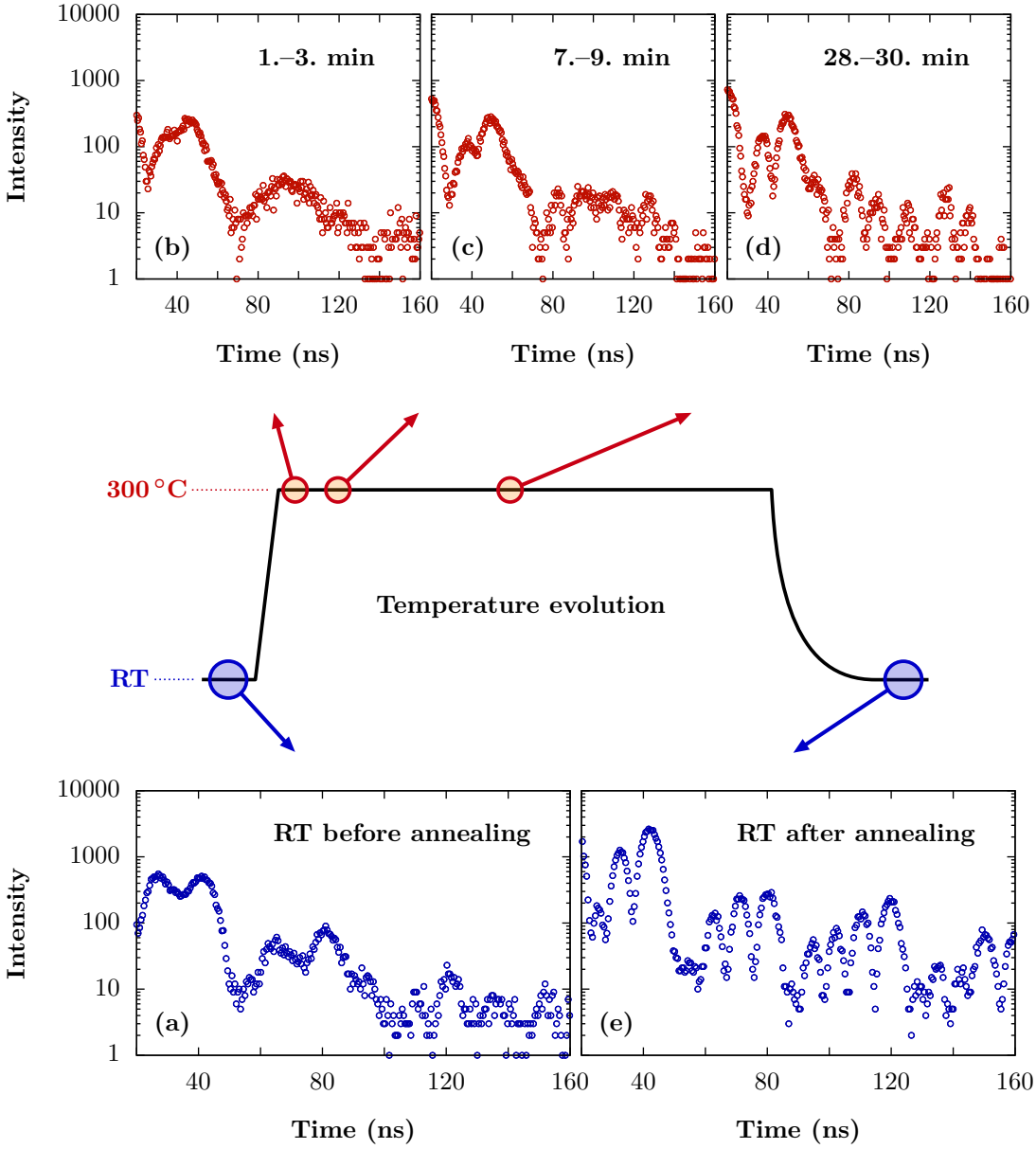

Figure 2.9: A scheme of NFS experiments conducted on $Fe_{81}Mo_8Cu_1B_{10}$ sample after its exposure to the N^+ ions irradiation. (a) A room-temperature time spectrum accumulated before the thermal treatment. (b–d) Time spectra measured under the elevated temperature during the corresponding times of annealing. (e) A room-temperature time spectrum of the sample after the annealing.

2.2.2 Formation of Nanocrystalline Grains

The multi-element metallic glasses and the related nanocrystalline alloys are typically very complex materials, regarding their elemental composition, structural properties and magnetic ordering at different regions in the material. This results in a complicated hyperfine structure (number of nuclear sites and their hyperfine splitting), commonly with broad distributions of hyperfine parameters [47, 61, 83, 85].

For the studied NANOPERM-type system the structural arrangement is related to the magnetic ordering, which allows to distinguish two basic contributions to the measured

time spectra. The first contribution originates from the original amorphous matrix, which is paramagnetic and exhibits only electric hyperfine interactions. It is typical by a broad distribution of the quadrupole splitting resulting in a distinctive doublet in the energy domain. The second contribution is given by nuclear sites in the sample which exhibit magnetic hyperfine interactions. These are connected to the formation of nanocrystalline grains in the amorphous matrix. The grains naturally take the structure and ferromagnetic ordering of α-Fe and exhibit hyperfine magnetic field of more than 30 T [74]. In addition to the crystalline magnetic phase, the ferromagnetic exchange interactions among the grains might influence the amorphous regions in the vicinity of the crystals, causing a magnetic splitting of ^{57}Fe energy levels at these regions [86]. Consequently, the magnetic contributions could be ascribed to both the crystalline and the amorphous magnetic phases in the sample.

Although the transitions between the magnetically and electrically split energy levels could be generally coupled in the time domain into complex quantum beats, the measured time spectra of $Fe_{81}Mo_8Cu_1B_{10}$ allow to distinguish between the magnetic and the electric contributions. The electric contribution results in the "envelope" time patterns occurring with the period of around 40 ns at room temperature (see for example Fig. 2.9e), whereas the energy splitting of the magnetic contribution gives the low-periodic (high-frequency) beating with the room-temperature period of around 10–15 ns. In the following part, they will be referred to as the low-frequency and the high-frequency (magnetic) quantum beats.

In the room-temperature time spectrum measured before the sample heating (Fig. 2.9a) the low-frequency as well as the high-frequency quantum beats can be recognised. The magnetic part is present because of very small magnetic grains, that were formed in the sample during its preparation and could also be modified by the subsequent ion irradiation.

Fig. 2.9(b–d) demonstrate the evolution of time spectra during the sample annealing. The time spectrum measured immediately after the temperature raise to 300 °C exhibits dominantly contribution from the amorphous matrix and partially from the small amount of the nanocrystalline grains (Fig. 2.9b). Few minutes later, new nanocrystalline grains start to form. This is accompanied by the appearance and evolution of the high-frequency quantum beats (Fig. 2.9b, c). Finally, a significant contribution of the magnetic phases can be seen as the well-developed high-frequency quantum beats in Fig. 2.9e, i.e. after the crystallization process has ended.

The next section compares the time spectra measured under both geometrical arrangements and discusses the results on the basis of the rotational invariance and its violation.

2.2.3 Identification of Magnetic Inhomogeneities

Fig. 2.10 shows the pair of time spectra measured at room temperature before the sample annealing, i.e. the time spectra measured under the same conditions for the air-side and the wheel-side orientation of the sample are compared. Both time spectra were normalized to unity area. Despite being qualitatively very similar, the time spectra exhibit differences which are significantly higher than the uncertainties of the experimental points. VRI is clearly visible mainly between 20 ns and 50 ns (Fig. 2.10b) in the form of different ratios between the high-frequency quantum beats. On the basis of the theoretical analysis in section 2.1, it can be concluded that the measured metallic glass sample exhibits inhomogeneities. These inhomogeneities are of a magnetic (high-frequency) nature and can be therefore ascribed to the magnetic nuclear sites in the sample. In addition, the hyperfine magnetic field directions are not randomly distributed but exhibit texture.

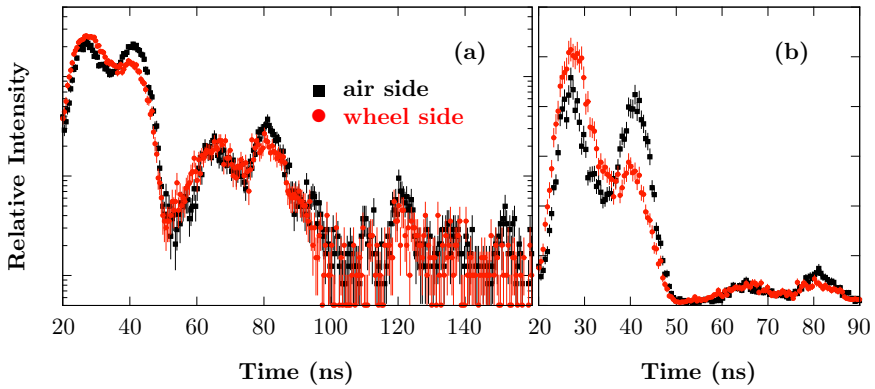

Figure 2.10: NFS time spectra of $Fe_{81}Mo_8Cu_1B_{10}$ measured at room temperature for the air-side (black squares) and the wheel-side (red-circles) orientation of the sample. The data are shown (a) on a conventional logarithmic scale in full time range and (b) on a linear scale between 20 ns and 90 ns to emphasize the measured VRI.

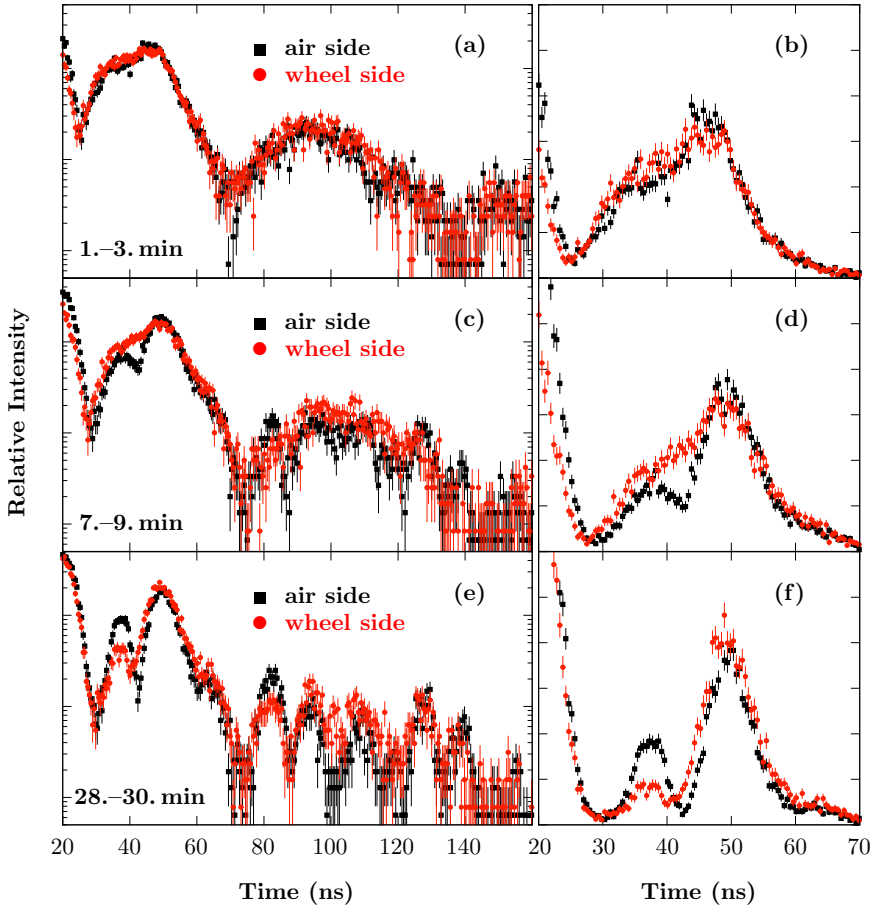

Figure 2.11: Time spectra of $Fe_{81}Mo_8Cu_1B_{10}$ measured at different times during the isothermal annealing at 300 °C. Differences in the time spectra develop and VRI becomes more significant with the increasing amount of nanocrystalline grains during the crystallization.

Selected pairs of time spectra measured during the isothermal annealing of the sample are shown in Fig. 2.11. The time spectra acquired before the onset of crystallization show no significant difference (Fig. 2.11a, b). So the increase in temperature to 300 °C, which resulted in the suppression of high-frequency quantum beats, also caused the rotational invariance to be satisfied. This observation might be explained as a suppression of magnetic interactions in the amorphous regions which, at room temperature, were influenced by the exchange interactions among the nanocrystalline grains.

As new nanocrystalline grains began to form in the sample, VRI became visible again (Fig. 2.11c, d). The differences in the ratios between the high-frequency quantum beats further evolved with time up to around 30 minutes of annealing (Fig. 2.11e, f). After that the time spectra did not exhibit any significant qualitative changes. It can be therefore presumed that the crystallization took place mainly during this time period.

The development of differences between the ratios of high-frequency quantum beats can be explained as a result of increasing amount of the crystalline magnetic phase in the sample. This is analogous to the example given in Fig. 2.7. VRI becomes more significant during the crystallization, where the amount of crystallites (and therefore the number of ^{57}Fe nuclei that contribute to magnetic inhomogeneities) increases and enhances the role of multiple scattering. At this state, the magnetic inhomogeneities and texture can be ascribed to the newly formed nanocrystalline grains. The rotational invariance remained violated when the sample cooled down to room temperature (Fig. 2.12).

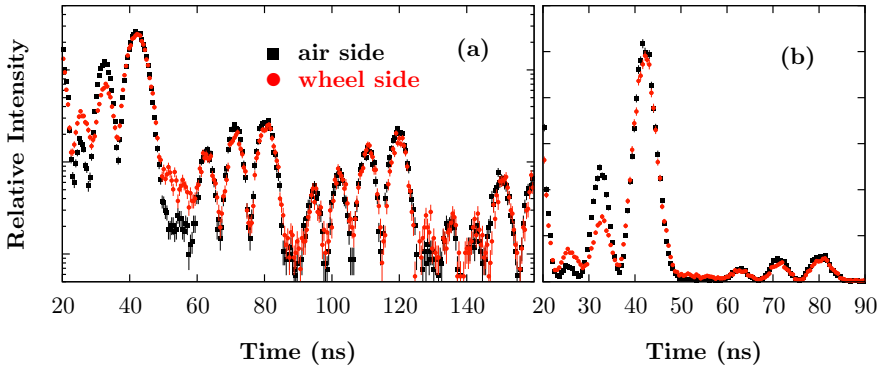

Figure 2.12: Comparison of time spectra measured at room temperature after the annealing.

2.3 Discussion

The conducted experiments demonstrated a utilization of NFS for the investigation of materials exhibiting an inhomogeneous spatial distribution of hyperfine parameters. The presence of magnetic inhomogeneities along the direction of the incoming radiation was revealed in the $Fe_{81}Mo_8Cu_1B_{10}$ sample. This was achieved solely by the analysis based on considering the VRI effect. Additional information could also be obtained by observing the evolution of VRI during the crystallization process.

To emphasize the uniqueness of the obtained information, the experimental techniques which are commonly used in solid-state studies do not allow any investigations of this type. For example, CEMS can be used to obtain a surface-selective information (e.g. from the air side and the wheel side of the ribbons separately) on the hyperfine interactions. However, it allows measurements only to about 200 nm sample depths so the information on the sample volume is unavailable by this technique. On the other hand, the conventional techniques

that allow to explore the bulk sample modifications (e.g. magnetization measurements) provide only an integral property over the whole measured system.

The information on the sample provided so far did not require any fitting of the time spectra. Nevertheless, for obtaining more information on the inhomogeneous regions (their thickness, hyperfine parameters, type of inhomogeneities, etc.) a detailed quantitative evaluation of the experimental data would be required. Creating such a complex fitting model solely on the basis of the conducted experiments is a challenging task. In addition to the inhomogeneities, the model would also need to reflect the time evolution of nuclear sites and their hyperfine parameters during the crystallization. Finally, a proper representation of the texture needs to be implemented for a correct evaluation of experimental data. The texture problem in NRS for a general case of thick samples will be described in the following chapter. To the author's knowledge, such a general implementation of the inhomogeneities and texture has not been realized in any currently available fitting software.

In measurements of thick Mössbauer samples a possible influence of inhomogeneities is worth considering. If a less accurate homogeneous system model is used for the spectra fitting, incorrect results might be obtained. In the presented measurements it was possible to fit the time spectra, to a certain degree, by a homogeneous model similar to those conventionally used for this type of material [74]. However, this model could not be used to fit the pairs of time spectra (air-side and wheel-side time spectra) simultaneously as VRI could not be reflected in the model. This shows that (at least for certain special cases) it is appropriate to evaluate thick-sample measurements carefully.

The approach of comparing two measurements differing by the 180 ° rotation of a sample with respect to one of the polarization axes can be a useful method to provide fundamental information on the inhomogeneities. Moreover, it could serve as a first step towards the more advanced methods of the inhomogeneous samples investigation. Some examples are mentioned very briefly as suggestions for possible future developments. (i) Regarding the individual types of inhomogeneities from Fig. 2.5, different polarizations of the incident radiation together with an external magnetic field could be utilized to identify a dominant inhomogeneity type, magnitude or directional. (ii) The external field may also be useful if a sample exhibits the magnitude magnetic inhomogeneities, but with random orientations of hyperfine fields. For observing VRI the texture can be induced by applying the external field in a chosen direction (see Fig. 2.5a). Advantageously, for sufficiently strong field the texture can take a simple unidirectional form with all magnetic moments oriented in the same chosen direction. (iii) Usage of polarization filtering could be considered for increasing the sensitivity to non-invariant scattering contributions. This was successfully used in the reciprocity studies. (iv) The previous ideas might be completed by conducting sets of measurements under different sample orientations, leading to more precise determination of the nuclear sites spatial distribution.

3 Texture Analysis

3.1 Introduction to Texture

As already discussed in previous chapters, Mössbauer samples may exhibit a preferential orientation of their effective electric and magnetic fields, usually referred to as texture (Fig. 3.1). In other words, the directional distributions of hyperfine interactions in the solid system may deviate from the random case described in section 1.3.3. The deviation may arise from the structure and atomic interactions within the system and it might also be altered by a specific preparation/modification treatment [87]. Nuclear resonant scattering shows to be highly sensitive to the local fields orientations and can be used for reconstructing the information on the texture.

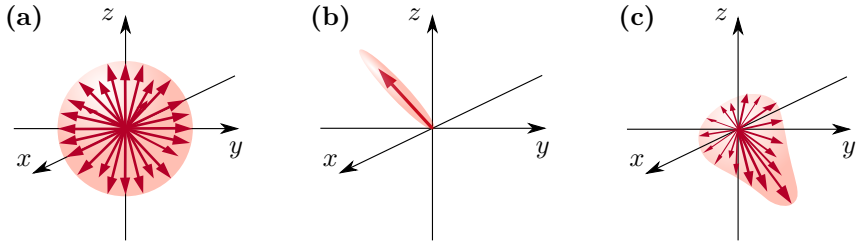

Figure 3.1: Illustration of the effective (e.g. magnetic) fields directional distributions, where more frequent orientations (more nuclei with a given magnetic field direction) are represented by bigger arrows. (a) A random case with equally distributed field directions. (b) An extreme example of the texture, where all the nuclei feel the magnetic field oriented in the same direction. (c) A general case of texture with some field directions being preferred over others.

The general integral (1.41) can be used to include all the directional contributions and obtain the total scattering length. The integration goes over all directions

$$N = \int_{\Omega} N(\Omega)\, D(\Omega)\, \mathrm{d}\Omega, \tag{3.1}$$

where the partial scattering lengths $N(\Omega)$ from (1.31) are weighted by the distribution function $D(\Omega)$ which is called the texture function. Essentially, the main goal of the texture determination by the TMS and NFS methods is to reconstruct the maximum possible information on the texture function.

In contrast to the (magnitude) distributions of hyperfine interactions, which may cause a significant broadening of Mössbauer lines in the energy domain, the texture can affect the relative probability amplitudes for individual transitions between the energy levels. This can be measured as modified ratios of the amplitudes of individual Mössbauer lines. These relative amplitudes can be considered as functions of the texture and the sample orientation. The texture determination is then based on running a series of measurements differing by appropriately chosen orientations of the sample with respect to the radiation coordinate system. The information on the texture function can be extracted either by a simultaneous fitting of the experimental data set with a proper fitting model or by applying specifically developed mathematical procedures for evaluating directly the relative lines amplitudes [11]. In the case of NFS the second option is complicated by the fact that the amplitudes of individual time-spread "frequency contributions" instead of localized lines are affected by the texture.

To evaluate experimental data measured on samples with texture a parametrization of the texture function is needed. Actually, the parametrization comes naturally from the symmetries of the nuclear scattering process. This has been treated only for the special cases of (i) pure magnetic hyperfine interactions, (ii) pure axially symmetrical electric interactions or (iii) a collinear combination of the first two cases (see the section 1.3.3). A conventional approach is to expand the texture function in the basis of real spherical harmonics [19]

$$D(\theta,\phi) = \sum_{l=0}^{\infty} \sum_{m=-l}^{l} D_{l,m} Y_{l,m}(\theta,\phi). \tag{3.2}$$

The angles θ, ϕ of the effective magnetic field in (3.2) could be equivalently exchanged with the angles β, α of the EFG main axes orientation. For simplicity, the notation using θ, ϕ will be used. The continuous texture function can be equivalently described by the discrete coefficients $D_{l,m}$.

The description of the texture has been treated for TMS using the thin-sample approximation [75]. For M1 transition, the symmetries of the magnetic dipole radiation result in the transmitted radiation intensity, which is linearly dependent on the texture coefficients $D_{l,m}$ for $l \leq 2$, but is independent of the higher-order coefficients. Consequently, only a limited information on the texture is obtainable by Mössbauer spectroscopy. A minimum texture $D_{\min}(\theta,\phi)$ defined as

$$D_{\min}(\theta,\phi) = \sum_{l=0}^{2} \sum_{m=-l}^{l} D_{l,m} Y_{l,m}(\theta,\phi) \tag{3.3}$$

is the closest experimentally available approximation of $D(\theta,\phi)$.

The trivial texture coefficient $D_{0,0}$ is equal to $1/\sqrt{4\pi}$, which ensures the normalisation of $D(\theta,\phi)$ to unity. The other eight coefficients are parameters to be determined. Using an unpolarized radiation source the five texture coefficients $D_{2,-2}, D_{2,-1}, D_{2,0}, D_{2,+1}, D_{2,+2}$ can be reconstructed. The other three coefficients $D_{1,-1}, D_{1,0}, D_{1,+1}$ can be obtained using a circularly or elliptically polarized radiation source. The physical interpretation of the texture coefficients can be found in [88]. They are related to the average effective field direction, its projections to individual coordinate axes and also the second moments of the projections.

The problem could be further simplified depending on the properties of studied systems and the used radiation. For example, for the unpolarized radiation the principal axes of a system can be found in which only three of the five $D_{2,m}$ texture coefficients are not equal to zero [89]. The number of non-zero coefficients may further decrease if the system texture exhibits directional symmetries. Moreover, so called texture-free spectra (as measured for randomly oriented fields) can be measured under a specific sample geometry [90].

The high-brilliance synchrotron radiation sources are advantageous over the radioactive sources when magnetic structures of systems with a low effective thickness are investigated [91, 92]. Complex evaluation procedures have been developed for the NFS reconstruction of magnetic field directions in relatively thick samples using a simple model of unidirectional magnetic texture (combination of fully magnetized and fully random cases) [93, 94]. However, the reconstruction of a general texture by analysing the measurements in the time domain is a challenging task.

3.2 Scattering Formalism Applied to Texture

To emphasize the requirements for a general texture analysis covering materials of an arbitrary effective thickness, the complex metallic glass system from chapter 2 could be taken as an example. The possibility to study the spatial inhomogeneities requires a high effective thickness for exhibiting the multiple scattering. In the thin-sample approximation the inhomogeneities would not be reflected in the measurements.

This chapter combines the description of the texture by its $D_{l,m}$ coefficients, which has been conventionally applied in TMS, with the general theoretical formalism of the nuclear resonant coherent elastic scattering in the forward direction. This allows to include the effective thickness into the calculations. The formalism can be applied for the Mössbauer spectroscopy as well as for NFS.

The hyperfine interactions of the type (i–iii) given on the previous page will be considered. The results will be demonstrated for the case (i) of pure magnetic interactions with the six allowed energy transitions. The other two cases could be treated analogously, with the exception of the energy levels degeneracy in the case (ii).

The scattering length $N(\theta, \phi)$ of a given nuclear site with the magnetic field orientation given by the angles θ and ϕ is described by formula (1.31). The general integral (3.1) takes the explicit form

$$N = \int_0^{2\pi} \int_0^{\pi} N(\theta, \phi) D(\theta, \phi) \sin\theta \, \mathrm{d}\theta \mathrm{d}\phi. \tag{3.4}$$

Formula (3.4) can be simplified by expanding both $N(\theta, \phi)$ and $D(\theta, \phi)$ in the real spherical harmonics basis. Unlike the texture coefficients, which depend on a particular texture function, the scattering length coefficients can be explicitly determined. The results of the $N(\theta, \phi)$ evaluation using the real spherical harmonics are given in appendix B. The angular dependence is hidden in the $n^{m_\mathrm{g}, m_\mathrm{e}}$ matrices of the scattering length[6] as given by formulas (1.32) and (1.33). The expansion leads to the coefficients $n_{l,m}^{m_\mathrm{g}, m_\mathrm{e}}$ which are also matrices. By substituting the expansions into (3.4) and using the orthogonality of real spherical harmonics the integral reduces to

$$N = \sum_{l=0}^{2} \sum_{m=-l}^{l} \sum_{m_\mathrm{g}, m_\mathrm{e}} L_{m_\mathrm{g}}^{m_\mathrm{e}}(E) \, n_{l,m}^{m_\mathrm{g}, m_\mathrm{e}} \, D_{l,m}. \tag{3.5}$$

In this notation the summation runs over all allowed transitions between the ground and the excited energy levels. As only six transitions are allowed by the selection rules the two transitions could be explicitly excluded from the summation indexes. However, the established notation will be kept for simplicity.

The generalized scattering length N depends only on the first nine texture coefficients. Consequently, only the minimum texture (3.3) can be extracted from the nuclear resonant scattering, regardless of the applied method, the polarization of the incident radiation or the sample effective thickness. The individual experimental and sample conditions may, however, influence how much information on the texture is accessible and how sensitive the scattering/transmission is to the directional distribution of the magnetic field. This could also lead to various evaluation methods which might be suitable for different cases.

[6] The matrices are indexed by the magnetic quantum numbers $m_{\mathrm{g,e}} = -j_{\mathrm{g,e}}, -j_{\mathrm{g,e}} + 1, \ldots, j_{\mathrm{g,e}} - 1, j_{\mathrm{g,e}}$ as the Hamiltonian (1.17) is diagonal. Although a simplified form of the scattering matrix could be used for calculations we kept the general form (a) to utilize properties of the general matrices that describe the scattering length and (b) for the possible future extensions, where such description would be necessary.

The following sections will treat separately individual cases, differing by the applied experimental method (TMS or NFS) and by the thickness of the scattering system. The results of this work will be demonstrated for unpolarized and linearly polarized radiation.

3.3 Thin Sample by TMS

Although the Mössbauer transmission through ideally thin samples in energy domain has already been treated in the literature its following description using the scattering matrix formalism allows to verify the validity of the obtained results and also their direct comparison with the results derived in the later sections.

The transmitted radiation intensity $I_{\mathrm{tr}}(E)$ can be calculated using the formula (1.43) with the scattering matrix given by (1.35). The derived scattering length from (3.5) will be used for the following calculations. The thin-sample approximation can be obtained by expanding T in a Taylor series and restricting the intensity only to expressions which are at most linear in ξ (see section 1.3.4). The normalized transmitted radiation intensity in the first-order approximation with respect to ξ is then given by formula

$$I_{\mathrm{tr}}^{(1)}(E) = \mathrm{Tr}\left\{\rho\right\} + i\xi\,\mathrm{Tr}\left\{N\rho - \rho N^{\dagger}\right\}, \tag{3.6}$$

where $\mathrm{Tr}\left\{\rho\right\} = 1$.

After substituting the corresponding density matrices from (1.44) to (3.6) the radiation intensities $I_{\mathrm{tr,u}}^{(1)}(E)$ for the unpolarized incident radiation and $I_{\mathrm{tr},\sigma}^{(1)}(E)$ for the linearly polarized radiation along the $\vec{\varepsilon}_{\sigma}$ direction are given as

$$I_{\mathrm{tr},\sigma}^{(1)}(E) = 1 - 2\xi\,\mathrm{Im}\left\{N_{\sigma\sigma}(E)\right\}, \tag{3.7a}$$

$$I_{\mathrm{tr,u}}^{(1)}(E) = 1 - \xi\,\mathrm{Im}\left\{N_{\sigma\sigma}(E) + N_{\pi\pi}(E)\right\}. \tag{3.7b}$$

The intensities depend linearly on the scattering length elements, showing that the multiple scattering is not reflected in the thin sample approximation. Moreover, the off-diagonal matrix elements are not present in the approximated formulas, so the polarization mixing is negligible. This linearised problem can be described as a simple Mössbauer absorption. The intensity (3.6) can be rewritten into a commonly used form which includes a sum of individual absorption Mössbauer lines (Fig. 3.2)

$$I_{\mathrm{tr}}^{(1)}(E) = 1 - \sum_{m_{\mathrm{g}},m_{\mathrm{e}}} I_{m_{\mathrm{g}},m_{\mathrm{e}}}^{(1)}(E). \tag{3.8}$$

The form of the Mössbauer lines for a given polarization is clear from the direct comparison of (3.8) with (3.7a) and (3.7b). Finally, formula (3.5) can be used for substituting the individual scattering length elements and obtaining the dependence of the Mössbauer lines on the texture coefficients

$$I_{m_{\mathrm{g}},m_{\mathrm{e}}}^{(1),\,\sigma}(E) = 2\xi\,\mathrm{Im}\left\{L_{m_{\mathrm{g}}}^{m_{\mathrm{e}}}(E)\right\} \sum_{l=0,2} \sum_{m=-l}^{l} \left(n_{l,m}^{m_{\mathrm{g}},m_{\mathrm{e}}}\right)_{\sigma\sigma} D_{l,m}, \tag{3.9a}$$

$$I_{m_{\mathrm{g}},m_{\mathrm{e}}}^{(1),\,\mathrm{u}}(E) = \xi\,\mathrm{Im}\left\{L_{m_{\mathrm{g}}}^{m_{\mathrm{e}}}(E)\right\} \sum_{l=0,2} \sum_{m=-l}^{l} \left[\left(n_{l,m}^{m_{\mathrm{g}},m_{\mathrm{e}}}\right)_{\sigma\sigma} + \left(n_{l,m}^{m_{\mathrm{g}},m_{\mathrm{e}}}\right)_{\pi\pi}\right] D_{l,m}. \tag{3.9b}$$

The formulas were simplified by using the fact that the diagonal elements of $n_{l,m}^{m_{\mathrm{g}},m_{\mathrm{e}}}$ are real. The imaginary part of $L_{m_{\mathrm{g}}}^{m_{\mathrm{e}}}(E)$ is the conventional Lorentzian dependence of the

absorption on the radiation energy [95]. The lines $I^{(1),\sigma}_{m_\mathrm{g},m_\mathrm{e}}(E)$, $I^{(1),\mathrm{u}}_{m_\mathrm{g},m_\mathrm{e}}(E)$ fully describe the Mössbauer spectra measured on thin samples with the unpolarized or linearly polarized source, respectively.

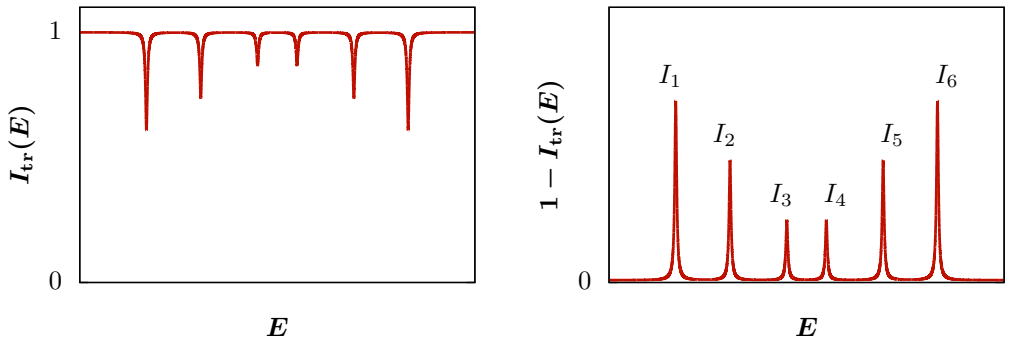

Figure 3.2: Transmission Mössbauer spectrum (on the left) with the intensity attenuation given by the individual Mössbauer absorption lines (on the right). The amplitudes of individual Mössbauer lines $I_{m_\mathrm{g},m_\mathrm{e}}$ can be reindexed by their order $I_{-1/2,-3/2} = I_1$, $I_{-1/2,-1/2} = I_2$, $I_{-1/2,1/2} = I_3$, etc.

The sums in (3.9a) and (3.9b) run only over the l values of 0 and 2. The contributions corresponding to $l = 1$ are zero for the considered polarizations. As a result the Mössbauer lines depend only on the trivial texture coefficient $D_{0,0}$ and the five texture coefficients $D_{2,-2}, D_{2,-1}, D_{2,0}, D_{2,+1}, D_{2,+2}$. Information on $D_{1,-1}, D_{1,0}, D_{1,+1}$ cannot be extracted from Mössbauer spectra under such conditions.

As stated before, determination of the texture coefficients can be realized by evaluating the amplitudes of the Mössbauer lines, given as the values of the transmitted radiation intensities in resonances

$$I^{(1)}_{m_\mathrm{g},m_\mathrm{e}} = I^{(1)}_{m_\mathrm{g},m_\mathrm{e}}(\Delta E_{m_\mathrm{g},m_\mathrm{e}}). \tag{3.10}$$

Assuming a sufficient resolution of the individual lines (i.e. the lines do not overlap), the resonance condition $E = \Delta E_{m_\mathrm{g},m_\mathrm{e}}$ used in (3.10) leads to the following amplitudes

$$I^{(1),\sigma}_{m_\mathrm{g},m_\mathrm{e}} = -\frac{4\xi}{\Gamma} \sum_{l=0,2} \sum_{m=-l}^{l} \left(n^{m_\mathrm{g},m_\mathrm{e}}_{l,m}\right)_{\sigma\sigma} D_{l,m}, \tag{3.11a}$$

$$I^{(1),\mathrm{u}}_{m_\mathrm{g},m_\mathrm{e}} = -\frac{2\xi}{\Gamma} \sum_{l=0,2} \sum_{m=-l}^{l} \left[\left(n^{m_\mathrm{g},m_\mathrm{e}}_{l,m}\right)_{\sigma\sigma} + \left(n^{m_\mathrm{g},m_\mathrm{e}}_{l,m}\right)_{\pi\pi}\right] D_{l,m}. \tag{3.11b}$$

The indexing of Mössbauer lines using the quantum numbers m_g, m_e can be equivalently rewritten by using their order in the energy domain from the lowest to the highest energy instead. So the amplitudes of the lines can be re-indexed as $I^{(1)}_{m_\mathrm{g},m_\mathrm{e}} \to I_k$, $k = 1, 2, \ldots, 6$.

In the conventional transmission arrangement the detection of background prevents the direct comparison of the measured amplitudes of Mössbauer lines with (3.11a) and (3.11b). The texture coefficients have to be taken not from the absolute values, but from the ratios of the individual lines amplitudes. However, one can find that for the considered polarization states the described transmission spectrum is symmetrical, i.e. $I_1 = I_6$, $I_2 = I_5$ and $I_3 = I_4$. In addition, the ratio I_1/I_3 is always equal to 3. One measured Mössbauer spectrum thus provides only one independent ratio of the amplitudes, which is the ratio of the first and the second line amplitude I_1/I_2.

Denoting the measured value of the I_1/I_2 ratio as r, the problem can be essentially understood as a simple linear equation $I_1 - rI_2 = 0$, where I_1 and I_2 are linear functions of $D_{l,m}$ according to (3.11a) and (3.11b), which also depend on the sample orientation. To extract the five texture coefficients, five independent measurements for appropriate orientations are required. In practice, the texture coefficients could be obtained either from a simultaneous fitting of spectra or by fitting the amplitudes ratio as a function $r(\Lambda, D_{l,m})$ of the sample orientation Λ, where $D_{l,m}$ act as the fitting parameters [75, 88].

3.4 Thick Sample by TMS

The transmission through thick samples follows the same general formulas as in the thin-sample approximation. The expansion of the scattering matrix can be performed again. However, for a scattering system of arbitrary effective thickness the problem cannot be linearised, i.e. the exponential form of the matrix should be considered.

The Mössbauer lines of the energy sextet are again assumed to be well resolved. This assumption is basically ensured by a sufficiently strong hyperfine magnetic field, which is very often satisfied. The scattering length (3.5) in resonance with respect to a given transition energy $\Delta E_{m_\mathrm{g},m_\mathrm{e}}$ is then given by formula

$$N(\Delta E_{m_\mathrm{g},m_\mathrm{e}}) = -i\frac{2}{\Gamma}\sum_{l=0}^{2}\sum_{m=-l}^{l} n_{l,m}^{m_\mathrm{g},m_\mathrm{e}}\, D_{l,m}. \tag{3.12}$$

The sum over all energy transitions in (3.5) reduces to only one non-negligible contribution for given $m_\mathrm{g}, m_\mathrm{e}$ because the Lorentzian functions corresponding to other transitions are off-resonance and essentially zero at this energy.

The matrix exponential evaluation using (3.12) for the scattering length gives the scattering matrix in a resonance

$$T(\Delta E_{m_\mathrm{g},m_\mathrm{e}}) = \exp\left[\frac{2\xi}{\Gamma}\sum_{l=0}^{2}\sum_{m=-l}^{l} n_{l,m}^{m_\mathrm{g},m_\mathrm{e}}\, D_{l,m}\right] \tag{3.13}$$

and the resonant value of a Mössbauer spectrum for a given transition is

$$I_\mathrm{tr}(\Delta E_{m_\mathrm{g},m_\mathrm{e}}) = \mathrm{Tr}\left\{T(\Delta E_{m_\mathrm{g},m_\mathrm{e}})\,\rho\,T^\dagger(\Delta E_{m_\mathrm{g},m_\mathrm{e}})\right\}. \tag{3.14}$$

The Hermitian conjugate of the scattering matrix can be written as

$$T^\dagger(\Delta E_{m_\mathrm{g},m_\mathrm{e}}) = \exp\left[\frac{4\xi}{\Gamma}\sum_{l=0}^{2}\sum_{m=-l}^{l}\left(n_{l,m}^{m_\mathrm{g},m_\mathrm{e}}\right)^\dagger D_{l,m}\right]. \tag{3.15}$$

It can be checked that the matrices $n_{l,m}^{m_\mathrm{g},m_\mathrm{e}}$ are Hermitian (see appendix B) and therefore, using the basic properties of the matrix trace, the value of $I_\mathrm{tr}(\Delta E_{m_\mathrm{g},m_\mathrm{e}})$ can be simplified into the following final form

$$I_\mathrm{tr}(\Delta E_{m_\mathrm{g},m_\mathrm{e}}) = \mathrm{Tr}\left\{\rho\,\exp\left[\frac{4\xi}{\Gamma}\sum_{l=0}^{2}\sum_{m=-l}^{l} n_{l,m}^{m_\mathrm{g},m_\mathrm{e}}\, D_{l,m}\right]\right\}. \tag{3.16}$$

The same notation as in the thin sample approximation may be used to obtain the amplitudes of individual Mössbauer lines

$$I_{m_\mathrm{g},m_\mathrm{e}} = 1 - I_\mathrm{tr}(\Delta E_{m_\mathrm{g},m_\mathrm{e}}). \tag{3.17}$$

3.4.1 Non-linear Texture Dependence

The thin-sample approximation of the Mössbauer lines amplitudes $I^{(1)}_{m_\mathrm{g},m_\mathrm{e}}$ given by (3.10) may be also obtained as the linear term of (3.17) after the exponential is expanded in the Taylor series. It is equal to

$$I^{(1)}_{m_\mathrm{g},m_\mathrm{e}} = -\frac{4\xi}{\Gamma}\sum_{l=0}^{2}\sum_{m=-l}^{l}\mathrm{Tr}\left\{\rho\, n_{l,m}^{m_\mathrm{g},m_\mathrm{e}}\right\} D_{l,m}. \tag{3.18}$$

It could be checked that the substitution of the corresponding density matrices into (3.18) gives exactly the formulas (3.11a) and (3.11b). The zero contribution of the $D_{1,m}$ terms can be explained by the fact that the $n_{1,m}^{m_\mathrm{g},m_\mathrm{e}}$ matrices are anti-diagonal (i.e. their diagonal elements equal zero). Multiplication by the ρ_σ and ρ_u density matrices does not change the diagonal elements and therefore the matrix trace in (3.18) gives zero for $l = 1$.

The effect of thickness can be illustrated on the first non-linear approximation $I^{(2)}_{m_\mathrm{g},m_\mathrm{e}}$ of the amplitudes, which is the second-order approximation of (3.17)

$$I^{(2)}_{m_\mathrm{g},m_\mathrm{e}} = I^{(1)}_{m_\mathrm{g},m_\mathrm{e}} - \frac{1}{2}\left(\frac{4\xi}{\Gamma}\right)^2\sum_{l=0}^{2}\sum_{m=-l}^{l}\sum_{l'=0}^{2}\sum_{m'=-l'}^{l'}\mathrm{Tr}\left\{\rho\, n_{l,m}^{m_\mathrm{g},m_\mathrm{e}} n_{l',m'}^{m_\mathrm{g},m_\mathrm{e}}\right\} D_{l,m}D_{l',m'}. \tag{3.19}$$

By analysing the second term in (3.19) the main differences from the linear case can be demonstrated. The first significant difference is that the terms containing $D_{l,m}$ with $l = 1$ are generally not zero. Namely the terms with $D_{1,m}D_{1,m'}$ depend on multiplication of the anti-diagonal matrices $n_{1,m}^{m_\mathrm{g},m_\mathrm{e}} n_{1,m'}^{m_\mathrm{g},m_\mathrm{e}}$. The multiplication of two anti-diagonal matrices gives a diagonal matrix and the trace in (3.19) gives generally a non-zero value for these terms. As a result, the amplitudes and their ratios depend on all the nine texture coefficients.

The spectrum is still symmetric for the considered polarizations, so the number of independent amplitudes ratios is still limited. The information on the texture coefficients can be extracted from two independent ratios, e.g. I_1/I_2 and I_1/I_3. In contrast to the linear case, the I_1/I_3 ratio is no longer a constant. As a consequence we may obtain two independent equations from one measured spectrum. However, the amplitudes ratios now also depend on the effective thickness of the scattering system. Nevertheless, the effective thickness could either be taken as another variable or it could be determined in advance. Therefore, if proper orientations of the sample are selected, then the five measurements are again needed to extract the minimum texture.

With basically the same number of measurements as required for the thin-sample approximation, more information on the texture is available from the Mössbauer measurements when the thickness effects start to influence the spectra. As a drawback, the resulted dependencies on the texture coefficients are now non-linear. Selecting a suitable evaluation approach for extracting the texture coefficients for a general thickness would be an important point.

3.4.2 Role of Effective Thickness

A simple simulation has been performed in order to describe the influence of the increasing effective thickness on the Mössbauer lines amplitudes. The validity of the thin-sample approximation, which is considered for $d_\mathrm{eff} \ll 1$, is also checked for a selected texture example.

For the presented demonstration an example texture function $D^{\mathrm{ex}}(\theta,\phi)$ defined by the formula

$$D^{\mathrm{ex}}(\theta,\phi)=\frac{1+\sin\theta+3\cos^2\theta+\sin\theta\cos\phi+\sin^2\theta\cos 2\phi+\sin\theta\cos\theta\cos\phi}{\pi(8+\pi)} \tag{3.20}$$

has been used. The texture function has a finite integral over the magnetic field directions and is normalised to unity. It could also be checked that $D^{\mathrm{ex}}(\theta,\phi)$ is non-negative for all the argument values $\theta\in\langle 0,\pi\rangle$, $\phi\in\langle 0,2\pi\rangle$ and therefore satisfies the basic properties of a texture function. The list of its corresponding texture coefficients $D^{\mathrm{ex}}_{l,m}$ up to $l=2$ is given in Table 3.1. The visualisation of the function is shown in Fig. 3.3 and Fig. 3.4. $D^{\mathrm{ex}}(\theta,\phi)$ has also non-zero coefficients $D_{l,0}$ for the even values of l which are higher than $l=2$ ($D_{4,0}, D_{6,0}$ etc.). However, these coefficients do not influence Mössbauer spectra and cannot be reconstructed from TMS measurements.

The simulation was realized by the following approach. First, the coefficients $D^{\mathrm{ex}}_{l,m}$ from Table 3.1 were substituted into (3.16) and the lines amplitudes were calculated from (3.17) for the case of the unpolarized radiation. Then, the corresponding ratios I_1/I_2 were calculated for selected orientations of the scattering system. This was done for the effective thicknesses d_{eff} of $0.01, 0.1, 0.5$ and 1. In this way a simulation of the real TMS measurements on the samples with varying effective thickness was performed. In the next step the texture coefficients were reconstructed by solving the corresponding linear equations obtained from the thin-sample approximation as described in section 3.3. The thin-sample approximation was used for obtaining the texture coefficients independently of the used effective thickness.

l	m	$D^{\mathrm{ex}}_{l,m}$	$D^{\mathrm{ex}}_{l,m}$ round.
0	0	$\frac{1}{\sqrt{4\pi}}$	0.282
1	−1	0	0.000
1	0	0	0.000
1	1	$-\frac{2}{\sqrt{3\pi}(8+\pi)}$	−0.058
2	−2	0	0.000
2	−1	0	0.000
2	0	$\frac{64-5\pi}{16\sqrt{5\pi}(8+\pi)}$	0.068
2	1	$-\frac{2}{\sqrt{15\pi}(8+\pi)}$	−0.026
2	2	$\frac{4}{\sqrt{15\pi}(8+\pi)}$	0.052

Table 3.1: Texture coefficients of $D^{\mathrm{ex}}(\theta,\phi)$ in the real spherical harmonics basis up to $l=2$. The third column contains the precise values of the coefficients. The fourth column shows their corresponding numeric values rounded to three decimal places.

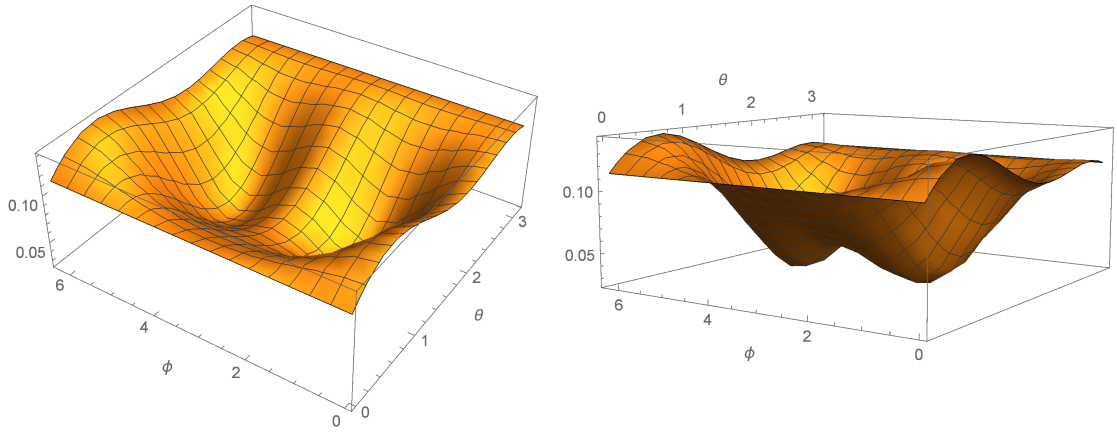

Figure 3.3: Plot of the texture function $D^{\mathrm{ex}}(\theta, \phi)$ from two different views.

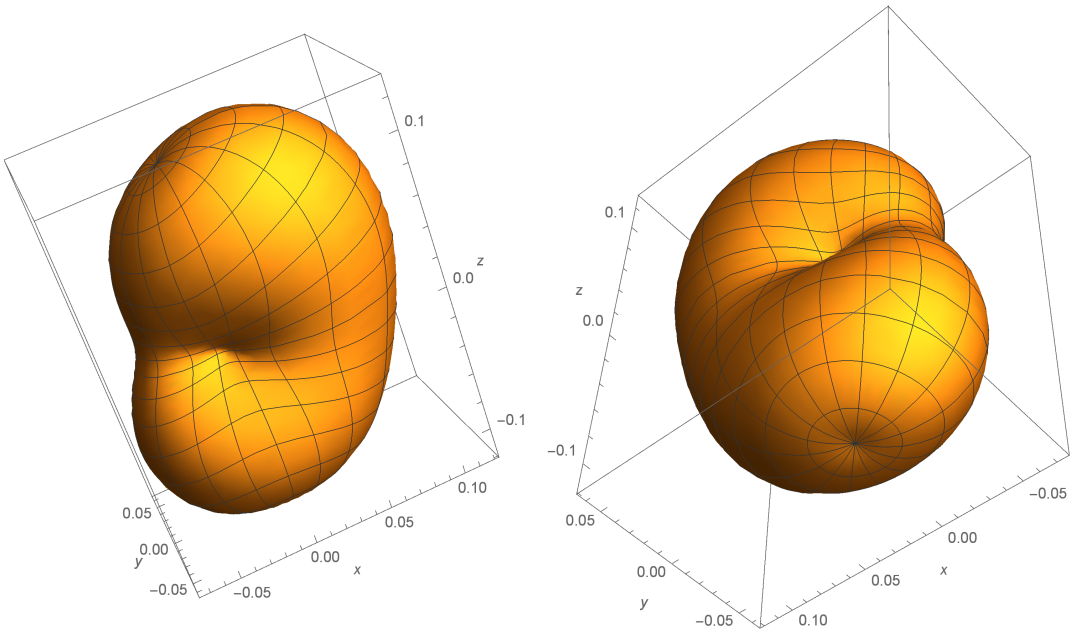

Figure 3.4: Spatial visualization of $D^{\mathrm{ex}}(\theta, \phi)$ in the Cartesian coordinate system.

The obtained results of the $D_{l,m}$ reconstruction are presented in Tab. 3.2. For the lowest effective thickness of 0.01 the reconstructed values are in agreement with the "real" ones. The difference is still relatively small for $d_{\text{eff}} = 0.1$. As the effective thickness increases the amplitudes of the Mössbauer lines start to be highly sensitive to the $D_{1,m}$ coefficients. However, this is not reflected in the thin-sample approximation, leading to the incorrect determination of the $D_{2,m}$ coefficients. Significant deviations can already be seen for the effective thickness values of 0.5 and 1.

texture coefficient	simulated value	$d_{\text{eff}} = 0.01$	$d_{\text{eff}} = 0.1$	$d_{\text{eff}} = 0.5$	$d_{\text{eff}} = 1$
$D_{1,-1}$	0.000	-	-	-	-
$D_{1,0}$	0.000	-	-	-	-
$D_{1,+1}$	-0.058	-	-	-	-
$D_{2,-2}$	0.000	0.000	0.003	0.015	0.029
$D_{2,-1}$	0.000	0.000	0.003	0.015	0.030
$D_{2,0}$	0.068	0.068	0.066	0.057	0.047
$D_{2,+1}$	-0.026	-0.026	-0.026	-0.025	-0.024
$D_{2,+2}$	0.052	0.052	0.049	0.035	0.019

Table 3.2: Determination of $D_{2,m}$ texture coefficients from the simulated amplitudes of Mössbauer lines based on the thin-sample approximation. Each column corresponds to coefficients extracted for a different thickness of the simulated scattering system. The deviation of the results from the simulated values increase with the increasing effective thickness.

3.5 Texture in NFS

As the time domain measurements are typically carried out using the linearly polarized incident radiation the texture description in NFS for this particular case will be provided. The time spectrum is given by formula (1.47), where the scattered radiation field $\vec{A}_{\text{sc}}(t)$ can be obtained by a Fourier transform of the energy domain field from (1.39)

$$\vec{A}_{\text{sc}}(t) = \mathcal{F}\left[\vec{A}_{\text{sc}}(E)\right] = \mathcal{F}\left[T - \mathbf{I}\right]\vec{A}_{\text{in}}. \tag{3.21}$$

The synchrotron radiation is linearly polarized in the plane of the accelerator storage ring and so the incident radiation field may be written as $\vec{A}_{\text{in}} = A_{\text{in}}\vec{\varepsilon}_{\sigma}$. The normalised form will be considered, where $I_{\text{in}} = |A_{\text{in}}|^2 = 1$. The scattered radiation field and the radiation intensity in the time domain can be thus written as

$$\vec{A}_{\text{sc}}(t) = \begin{pmatrix} \mathcal{F}\left[T_{\sigma\sigma} - 1\right] \\ \mathcal{F}\left[T_{\pi\sigma}\right] \end{pmatrix} A_{\text{in}}, \tag{3.22}$$

$$I_{\text{sc}}(t) = \vec{A}^{*}_{\text{sc}}(t) \cdot \vec{A}_{\text{sc}}(t) = \left|\mathcal{F}\left[T_{\sigma\sigma} - 1\right]\right|^2 + \left|\mathcal{F}\left[T_{\pi\sigma}\right]\right|^2. \tag{3.23}$$

For the sake of simplicity we will restrict ourselves only to the first-order approximation of $I_{\text{sc}}(t)$ in ξ. This is analogous to the previous approximation of the energy dependent radiation intensity using the Taylor expansion (see section 1.3.4). By applying the linearity of Fourier transform the approximated intensity follows the form

$$I^{(1)}_{\text{sc}}(t) = \xi^2\left(\left|\mathcal{F}\left[N_{\sigma\sigma}\right]\right|^2 + \left|\mathcal{F}\left[N_{\pi\sigma}\right]\right|^2\right). \tag{3.24}$$

In contrast to the Mössbauer spectroscopy, where the first-order approximation was linear in ξ, a quadratic dependence is obtained in NFS. In addition, the intensity depends on

the off-diagonal scattering length element $N_{\pi\sigma}$ even for a thin sample. The polarization mixing in NFS is reflected in measured time spectra for arbitrary effective thickness.

The explicit dependence of time spectra on the texture coefficients can be obtained by substituting formula (3.5) into (3.24)

$$I_{\mathrm{sc}}^{(1)}(t) = \xi^2 \sum_{\substack{l,m \\ l',m'}} \sum_{\substack{m_{\mathrm{g}},m_{\mathrm{e}} \\ m'_{\mathrm{g}},m'_{\mathrm{e}}}} \mathcal{F}\left[L_{m_{\mathrm{g}}}^{m_{\mathrm{e}}}(E)\right]^* \mathcal{F}\left[L_{m'_{\mathrm{g}}}^{m'_{\mathrm{e}}}(E)\right] \mathcal{N}_{l,m,l',m'}^{m_{\mathrm{g}},m_{\mathrm{e}},m'_{\mathrm{g}},m'_{\mathrm{e}}} D_{l,m} D_{l',m'}, \tag{3.25}$$

where

$$\mathcal{N}_{l,m,l',m'}^{m_{\mathrm{g}},m_{\mathrm{e}},m'_{\mathrm{g}},m'_{\mathrm{e}}} = \left[\left(n_{l,m}^{m_{\mathrm{g}},m_{\mathrm{e}}}\right)^*_{\sigma\sigma} \left(n_{l',m'}^{m'_{\mathrm{g}},m'_{\mathrm{e}}}\right)_{\sigma\sigma} + \left(n_{l,m}^{m_{\mathrm{g}},m_{\mathrm{e}}}\right)^*_{\pi\sigma} \left(n_{l',m'}^{m'_{\mathrm{g}},m'_{\mathrm{e}}}\right)_{\pi\sigma}\right]. \tag{3.26}$$

The Fourier transform of the Lorentzian functions gives non-zero values for $t > 0$, which is in agreement with the physical reality (scattered photons are detected after the incident radiation pulse that triggers the time measurement). The time dependence consists of a simple exponential decay with the lifetime of $\hbar/\Gamma$ and a sum of complex harmonic functions oscillating with the frequencies proportional to the energy differences between individual energy transitions

$$\begin{aligned} I_{\mathrm{sc}}^{(1)}(t) \propto \xi^2 \exp\left(-\frac{\Gamma t}{\hbar}\right) \sum_{\substack{l,m \\ l',m'}} \sum_{\substack{m_{\mathrm{g}},m_{\mathrm{e}} \\ m'_{\mathrm{g}},m'_{\mathrm{e}}}} \exp\left[i\,\frac{\left(\Delta E_{m_{\mathrm{g}},m_{\mathrm{e}}} - \Delta E_{m'_{\mathrm{g}},m'_{\mathrm{e}}}\right) t}{\hbar}\right] \\ \times\, \mathcal{N}_{l,m,l',m'}^{m_{\mathrm{g}},m_{\mathrm{e}},m'_{\mathrm{g}},m'_{\mathrm{e}}} D_{l,m} D_{l',m'}. \end{aligned} \tag{3.27}$$

Properties of $n_{l,m}^{m_{\mathrm{g}},m_{\mathrm{e}}}$ matrices can be used to expand the harmonic time dependence in simple trigonometric functions

$$I_{\mathrm{sc}}^{(1)}(t) \propto \xi^2 \exp\left(-\frac{\Gamma t}{\hbar}\right) \left(\mathcal{I}_1 + 2\mathcal{I}_2 - 2\mathcal{I}_3\right), \tag{3.28}$$

where

$$\mathcal{I}_1 = \sum_{\substack{l,m \\ l',m'}} \sum_{m_{\mathrm{g}},m_{\mathrm{e}}} \mathcal{N}_{l,m,l',m'}^{m_{\mathrm{g}},m_{\mathrm{e}},m_{\mathrm{g}},m_{\mathrm{e}}} D_{l,m} D_{l',m'}, \tag{3.29a}$$

$$\mathcal{I}_2 = \sum_{\substack{l,m \\ l',m' \\ (m_{\mathrm{g}},m_{\mathrm{e}}) \neq (m'_{\mathrm{g}},m'_{\mathrm{e}})}} \sum_{\substack{m_{\mathrm{g}},m_{\mathrm{e}} \\ m'_{\mathrm{g}},m'_{\mathrm{e}}}} \cos\left[\frac{\left(\Delta E_{m_{\mathrm{g}},m_{\mathrm{e}}} - \Delta E_{m'_{\mathrm{g}},m'_{\mathrm{e}}}\right) t}{\hbar}\right] \mathrm{Re}\left\{\mathcal{N}_{l,m,l',m'}^{m_{\mathrm{g}},m_{\mathrm{e}},m'_{\mathrm{g}},m'_{\mathrm{e}}}\right\} D_{l,m} D_{l',m'}, \tag{3.29b}$$

$$\mathcal{I}_3 = \sum_{\substack{l,m \\ l',m' \\ (m_{\mathrm{g}},m_{\mathrm{e}}) \neq (m'_{\mathrm{g}},m'_{\mathrm{e}})}} \sum_{\substack{m_{\mathrm{g}},m_{\mathrm{e}} \\ m'_{\mathrm{g}},m'_{\mathrm{e}}}} \sin\left[\frac{\left(\Delta E_{m_{\mathrm{g}},m_{\mathrm{e}}} - \Delta E_{m'_{\mathrm{g}},m'_{\mathrm{e}}}\right) t}{\hbar}\right] \mathrm{Im}\left\{\mathcal{N}_{l,m,l',m'}^{m_{\mathrm{g}},m_{\mathrm{e}},m'_{\mathrm{g}},m'_{\mathrm{e}}}\right\} D_{l,m} D_{l',m'}. \tag{3.29c}$$

The summations in $\mathcal{I}_2$ and $\mathcal{I}_3$ run only over different pairs of energy transitions.

Although an ideally thin sample was taken into considerations, a non-linear dependence on the texture coefficients was obtained. The situation in NFS is more similar to that of TMS applied to thick samples. The time spectrum contains information on all the nine $D_{l,m}$ coefficients. Basically, when applied to the same ideally thin scattering system, the NFS method is "more sensitive" to texture than TMS. The disadvantages are mainly the non-linearity and the necessity to extract the information in the time domain.

3.6 Concluding Remarks

Combination of the general scattering formalism with the texture description, using its coefficients in real spherical harmonics basis, allows to include the preferentially oriented electric or magnetic fields into a theoretical model of a scattering system. The results, as given in the previous sections, may be implemented into a software package for evaluating experimental data from energy or time domain measurements. Further efforts in selecting a suitable approach for the extraction of the texture coefficients is needed, mainly for TMS applied to thick samples and for the time-domain NFS. Major difficulties could be connected to the non-linear dependence of the Mössbauer lines and the time-domain patterns on the texture coefficients. One of the options can be the simultaneous fitting of the measured experimental data sets, where more sophisticated optimisation procedures (see section 1.3.5) might be considered.

The evaluation of NFS time spectra is complicated as the information contained in the energy absorption lines is delocalised in time. This can be seen in formula (3.28) and its expansion in the harmonic terms. For a thick sample the time dependence would become even more complicated due to a modulation by Bessel function [64, 65].

Except the simultaneous fitting of time spectra the harmonic dependence encourages a Fourier analysis for the texture extraction. Recently, the application of Fourier transform to time spectra has been successfully applied in NRS studies [92, 96]. Similar procedures to those developed in TMS could be used for the $D_{l,m}$ extraction, where the ratios of the lines obtained as a Fourier picture of the time signal could be evaluated.

4 ERNST Software Package

Currently, there are a number of different software packages available for evaluating the transmission Mössbauer spectra [63, 95, 97], NFS time spectra [98] or both [25, 99]. The development of a new software ERNST (Evaluation of Resonant Nuclear Scattering in energy and Time domain) was motivated by newly emerging demands on the data analysis, including those described in chapters 2 and 3. The basic information on the ERNST package and its current development status is reported in this chapter. Some specific software features and the future development are also discussed.

4.1 General Description

The software is developed in C programming language using Qt Creator development environment [100]. The C standard library and GSL (GNU Scientific Library) are used for the computation [101]. The code was written and tested on Linux operating system, but it can also be extended to Windows. ERNST works as a command line executable program. It reads the input data from an input ASCII file and, based on the chosen settings, creates an output file with the calculated data (Fig. 4.1).

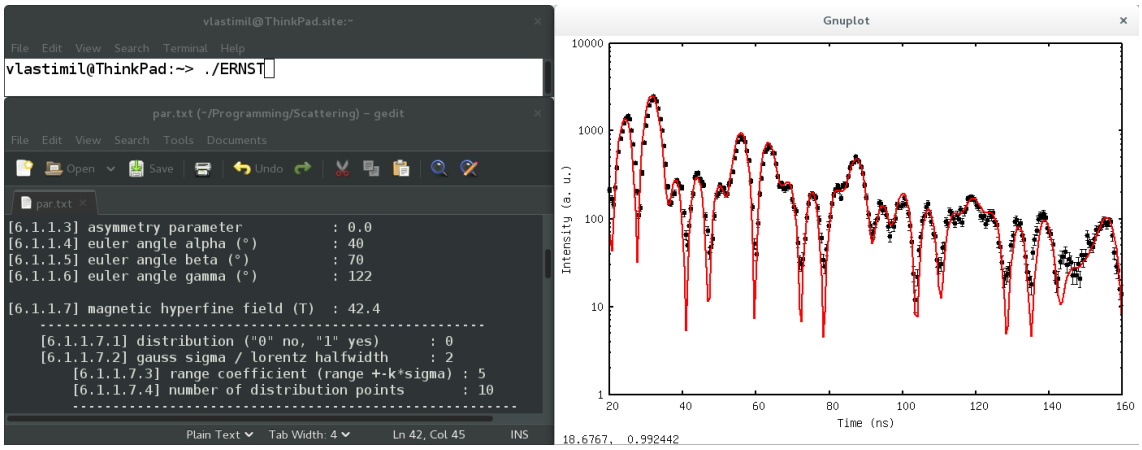

Figure 4.1: Screen of the ERNST software with a command line, an input ASCII file for setting parameters and a plot of results using the gnuplot software.

The magnetic dipole transition of ^{57}Fe nuclide is currently implemented in the software. The calculations of time and energy domain spectra are based on the theoretical formalism which was described in chapter 1. For each defined nuclear site the interaction Hamiltonian (1.17) is calculated and consequently diagonalised to obtain the corresponding eigenvalues and eigenvectors. The vector basis of the angular momentum operators $|j_g, m_g\rangle$ for the ground and $|j_e, m_e\rangle$ for the excited state of ^{57}Fe is used. The calculation is based on a full interaction Hamiltonian with combined electric and magnetic hyperfine interactions. The scattering lengths for individual nuclear sites are calculated according to (1.31). Depending on the chosen settings the scattering lengths can be computed for unidirectional or randomly oriented cases, with or without distributions of the hyperfine parameters. The program accounts for multilayered scattering systems. For the chosen number of layers the corresponding scattering matrices are calculated using the matrix

exponential (1.35). The Fourier transform is utilized for obtaining the data in the time domain. Finally, the radiation intensities $I_{\mathrm{tr}}(E)$ for TMS and $I_{\mathrm{sc}}(t)$ for TMS are calculated for given properties of the incident radiation. The calculated and experimental data can be compared and visualised using the gnuplot software package [102].

The input parameters used for the calculations are loaded from `par.txt` ASCII file. The parameters can be divided into four main groups: sample parameters, hyperfine parameters, radiation parameters and data parameters. To each parameter a specific number sequence `[W.X.Y.Z]` is assigned, where `W` number specifies the role of the parameter in the computation, `X` and `Y` label the system layer and nuclear site, respectivelly and `Z` is a number or a set of numbers that further specify the parameter. The corresponding numeric value, which is typed after the ":" symbol in the file, is then loaded by the program.

The sample parameters define the effective thickness of a sample, which depends on its real thickness, density of the resonant nuclei and the Lamb-Mössbauer factor. For a sample consisting of multilayers the parameters define the total number layers and their corresponding effective thicknesses. The number of nuclear sites in each layer is also defined within this group. An example of the sample parameters as given in `par.txt` input file is shown in Fig. 4.2.

```
====================
* SAMPLE PARAMETERS *
====================

[1] number of homogeneous sublayers : 2

[2.0] number of nuclear sites : 2
[3.0] sample thickness (μm) : 1.0
[4.0] 57Fe density (g/cm3) : 7.87
[5.0] Lamb-Mössbauer factor : 0.77

[2.1] number of nuclear sites : 1
[3.1] sample thickness (μm) : 0.5
[4.1] 57Fe density (g/cm3) : 7.87
[5.1] Lamb-Mössbauer factor : 0.77
```

Figure 4.2: Examples of the sample parameters from the `par.txt` file. The listed parameters define a two-layered model with two nuclear sites in the first and one nuclear site in the second layer.

The hyperfine parameters are defined for each nuclear site in each layer of the sample. In Fig. 4.3 a list of hyperfine parameters corresponding to the `X`-th layer and `Y`-th nuclear site in this layer is shown. Basic parameters are the relative weight of the nuclear site, the isomer shift, the quadrupole splitting and the hyperfine magnetic field. For the last three parameters a distribution of the values can be set by a group of additional parameters defining the type and properties of the distribution. If required, the applied distribution can be saved in a separate ASCII file which could be used for its visualization. The distributions settings will be described in a separate subsection. To define the orientation of the hyperfine magnetic field and the EFG tensor five angles are used (three Euler angles for the EFG and two angles for the hyperfine magnetic field). The magnetic field orientation is described with respect to the EFG coordination system (see Fig. 1.2). A deviation of the EFG from the axially symmetrical case can be described by the asymmetry parameter.

The last parameter is used to select if a unidirectional case defined by the five angles will be calculated or if an integrated scattering length with randomly oriented fields will be used.

```
========================
* HYPERFINE PARAMETERS *
========================
     ===========
     * LAYER X *
     ===========

     [6.X.Y.0] relative weight : 0.7

     [6.X.Y.1] isomer shift (mm/s) : 0.0
         ---------------------------------------------
         [6.X.Y.1.1] distribution ("0" no, "1" yes) : 0
         [6.X.Y.1.2] distribution width : 0
         [6.X.Y.1.3] range coefficient : 0
         [6.X.Y.1.4] number of distribution points : 0
         ---------------------------------------------

     [6.X.Y.2] quadrupole splitting (mm/s) : -0.2
         ---------------------------------------------
         [6.X.Y.2.1] distribution ("0" no, "1" yes) : 0
         [6.X.Y.2.2] distribution width : 0
         [6.X.Y.2.3] range coefficient : 0
         [6.X.Y.2.4] number of distribution points : 0
         ---------------------------------------------
     [6.X.Y.3] asymmetry parameter : 0.0
     [6.X.Y.4] Euler angle alpha (°) : 0.0
     [6.X.Y.5] Euler angle beta (°) : 0.0
     [6.X.Y.6] Euler angle gamma (°) : 0.0

     [6.X.Y.7] hyperfine magnetic field (T) : 30
         ---------------------------------------------
         [6.X.Y.7.1] distribution ("0" no, "1" yes) : 1
         [6.X.Y.7.2] distribution width : 1.5
         [6.X.Y.7.3] range coefficient : 3
         [6.X.Y.7.4] number of distribution points : 10
         ---------------------------------------------
     [6.X.Y.8] Bhf angle theta (°) : 0
     [6.X.Y.9] Bhf angle phi (°) : 0

     [6.X.Y.10] distribution type : 0
     [6.X.Y.11] print distribution ("0" no, "1" yes) : 1

     [6.X.Y.12] "polycrystalline" ("0" no, "1" yes) : 1
```

Figure 4.3: Examples of the hyperfine parameters corresponding to the Y-th nuclear site in the X-th layer of the sample. In the example a nuclear site with electric quadrupole and magnetic hyperfine interactions is defined. For the latter a distribution of the hyperfine magnetic field is set.

The radiation parameters are used to set the properties of the incident radiation and of the radiation detection. The radiation coordinate system can be rotated with respect to the laboratory reference frame. This is defined by the radiation Euler angles. The polarization type of the incident radiation may be set to the linear, right circular or left circular polarization. In the former, the plane of the linear polarization can also be rotated with respect to the horizontal polarization plane by an additional angle. Concerning the radiation detection, linear polarization filtering could be set, where the radiation passing through the sample could be detected either with the $\vec{\varepsilon}_\sigma$-filter or the $\vec{\varepsilon}_\pi$-filter. Finally, for NFS experiments the time delay between individual synchrotron radiation pulses needs to be set (see section 1.3.2). The data parameters influence the processing and comparison of the calculated and the experimental data. The minimum and maximum time values define the time range for the theoretical and experimental data comparison. An example of the radiation and the data parameters is presented in Fig. 4.4.

```
=======================
* RADIATION PARAMETERS *
=======================

[7] radiation Euler angle Phi (°) : 0
[8] radiation Euler angle Theta (°) : 0
[9] radiation Euler angle Psi (°) : 0

[10] polarization type ("-1" rcirc, "0" lin, "1" lcirc) : 0
[11] linear polarization angle (°) : 0
[12] polarized detection ("0" off, "1" sigma, "2" pi) : 0

[13] time delay of SR pulses (ns) : 173

===================
* DATA PARAMETERS *
===================

[14] time_min (ns) : 10
[15] time_max (ns) : 170
```

Figure 4.4: Examples of the radiation parameters and the data parameters.

4.2 Distributions of Hyperfine Parameters

ERNST enables a relatively simple setting of the hyperfine parameters distribution (see section 1.2.3) with a variety of different options. For each distribution the corresponding nuclear site is divided into individual "sub-sites" with their "sub-weights" given by a chosen distribution type. A separate interaction Hamiltonian and a scattering length are then affiliated to each sub-site.

There are currently three different distribution types: normal (Gaussian) distribution f_0, Cauchy (Lorentz) distribution f_1 and uniform (rectangular) distribution f_2. These distribution types are described by the following formulas

$$f_0(x) = \frac{1}{\sqrt{2\pi x_\mathrm{s}^2}} \exp\left[-\frac{(x - x_\mathrm{m})^2}{2x_\mathrm{s}^2}\right], \tag{4.1}$$

$$f_1(x) = \frac{1}{\pi} \frac{x_\mathrm{s}}{(x - x_\mathrm{m})^2 + x_\mathrm{s}^2}\,, \tag{4.2}$$

$$f_2(x) = \frac{1}{(x_\mathrm{m} + R_x x_\mathrm{s}) - (x_\mathrm{m} - R_x x_\mathrm{s})} = \frac{1}{2R_x x_\mathrm{s}}\,, \tag{4.3}$$

where x stands for a given hyperfine parameter (δ, Δ or B_hf). x_m represents a mean value of x and is defined by the value of `[6.X.Y.1]`, `[6.X.Y.2]` or `[6.X.Y.7]` depending on which hyperfine parameter distribution was chosen. The parameter x_s specifies the distribution width and its interpretation depends on the selected distribution type. For f_0 it is the distribution standard deviation, for f_1 it gives the half-width at half-maximum value (HWHM) and for f_2 the value of $2R_x x_\mathrm{s}$ defines the width of the rectangle (interval with the non-zero value). The three distribution types are shown in Fig. 4.5. Other applicable types could be easily included in the software if it was desirable.

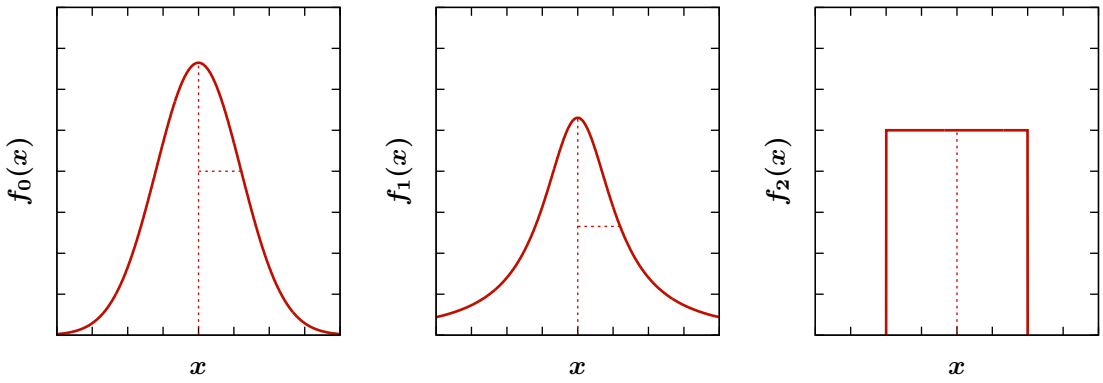

Figure 4.5: Examples of Gaussian (f_0), Lorentz (f_1) and rectangular (f_2) distribution types. The solid lines show the distributions, the vertical dashed lines show the positions of x_m and the horizontal lines in the f_0 and f_1 plots have the widths of x_s. The rectangle in the f_2 plot has the half-width of $R_x x_\mathrm{s}$.

The software takes only a finite number of x values to calculate the distribution. The total number of distribution points x_N together with the range parameter R_x give us the specific values of $x_j, j = 1, 2, \ldots, x_N$ as

$$x_j = x_\mathrm{m} - R_x x_\mathrm{s} + (j-1)\frac{2R_x x_\mathrm{s}}{x_N - 1}\,. \tag{4.4}$$

The corresponding distribution values $f_{0,1,2}(x_j)$ are normalized, so the sum $\sum_j f_{0,1,2}(x_j)$ equals to the weight of a given nuclear site. The x_j takes values in the range from $x_\mathrm{m} - R_x x_\mathrm{s}$ to $x_\mathrm{m} + R_x x_\mathrm{s}$ with the step of $2R_x x_\mathrm{s}/(x_N - 1)$ (see Fig. 4.6). For the computation to run successfully x_N must be greater than 1. The upper limit for x_N is not set but a potential user should keep in mind that more distribution points mean longer computing time, so usually a reasonable estimation of needed distribution points is required.

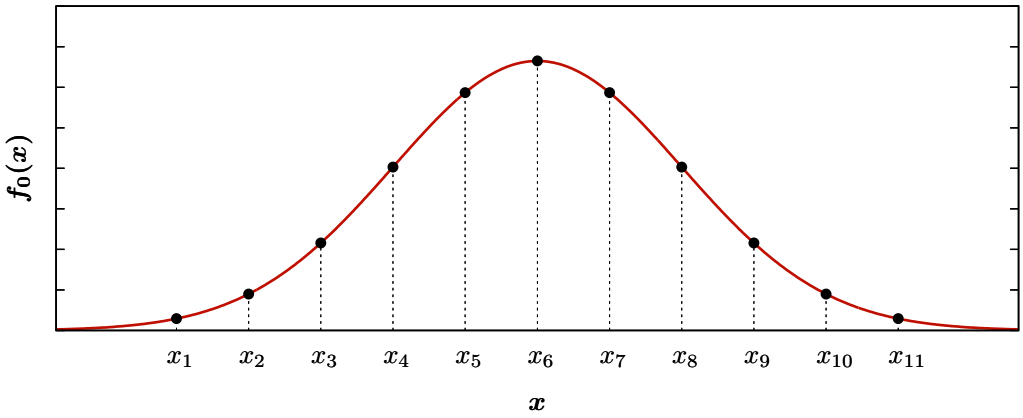

Figure 4.6: A Gaussian distribution with $x_N = 11$ points. The distribution is set so x_6 equals to the mean value x_m and x_8 is $x_\mathrm{m} + x_\mathrm{s}$. The range $R_x = 2.5$ and so the x_j values go from $x_\mathrm{m} - 2.5\,x_\mathrm{s}$ to $x_\mathrm{m} + 2.5\,x_\mathrm{s}$ with the step of $x_\mathrm{s}/2$.

ERNST also enables the use of multivariate distributions, i.e. simultaneous distributions of (δ, Δ), (δ, B), (Δ, B) or (δ, Δ, B). The two-dimensional or three-dimensional distributions $f^{(2)}_{0,1,2}$, $f^{(3)}_{0,1,2}$ are used, where (under the assumption of independent variables) these are given simply as multiplication of the corresponding one-dimensional distributions $f_{1,2,3}$. For example, the three-dimensional normal distribution of the hyperfine parameters $f^{(3)}_0(\delta, \Delta, B)$ is given as

$$f^{(3)}_0(\delta, \Delta, B) = f_0(\delta)\, f_0(\Delta)\, f_0(B) = \frac{\exp\left\{-\frac{1}{2}\left[\frac{(\delta-\delta_\mathrm{m})^2}{\delta_\mathrm{s}^2} + \frac{(\Delta-\Delta_\mathrm{m})^2}{\Delta_\mathrm{s}^2} + \frac{(B-B_\mathrm{m})^2}{B_\mathrm{s}^2}\right]\right\}}{(2\pi)^{3/2}\delta_\mathrm{s}\Delta_\mathrm{s}B_\mathrm{s}}\,. \quad (4.5)$$

4.3 Incoherent Time Spectra Summation

In NFS a measured time spectrum is given by a contribution of many scattered synchrotron radiation pulses. Assuming the time delay between two following pulses comparable to the lifetime of the ^{57}Fe excited state, the number of pulses detected per one minute is $\sim 10^8$. So far, the time spectra were described for a given steady state of a sample. Then each radiation pulse is scattered under the same sample conditions and contributes equally to the given time spectrum.

For studying a physical process (phase or structural transformation, magnetic transition, etc.) during which the time spectra are continuously acquired, the process must be slow enough with respect to the acquisition time of one time spectrum. Although the photon flux and the brilliance of the synchrotron radiation have been significantly increasing in the last decades, there could be cases where such condition is not satisfied. An example case is a dynamical experiment conducted on magnetic sample in a vicinity of its Curie temperature.

To evaluate time spectra acquired during fast changes of the measured samples, the following procedure has been added to ERNST software. Consider a fast process[7] with

[7]The process should still be slow enough with respect to the lifetime of the nuclei excited state, i.e. during the scattering of one synchrotron radiation pulse the state of the scattering system should be considered as static.

respect to the acquisition time of one time spectrum. Under such assumption the time spectrum should be considered as a sum of an appropriate number of sub-spectra, each describing a different state of the sample during its evolution (Fig. 4.7). If the i-th time sub-spectrum would be described by a normalized intensity $I_i(t)$, then the time spectrum $\widehat{I}(t)$ would be given as

$$\widehat{I}(t) = \sum_i v_i I_i(t), \tag{4.6}$$

where v_i are weight coefficients of $I_i(t)$, $\sum_i v_i = 1$. Each $I_i(t)$ and v_i reflect a state of the system described by a different set of hyperfine parameters. In contrast to the hyperfine interactions distributions, where the scattering lengths are being weighted (see section 1.2.3), here the fast process results in the distribution of the intensities. In such case the time sub-spectra are added "incoherently", i.e. the radiation intensities are summed.

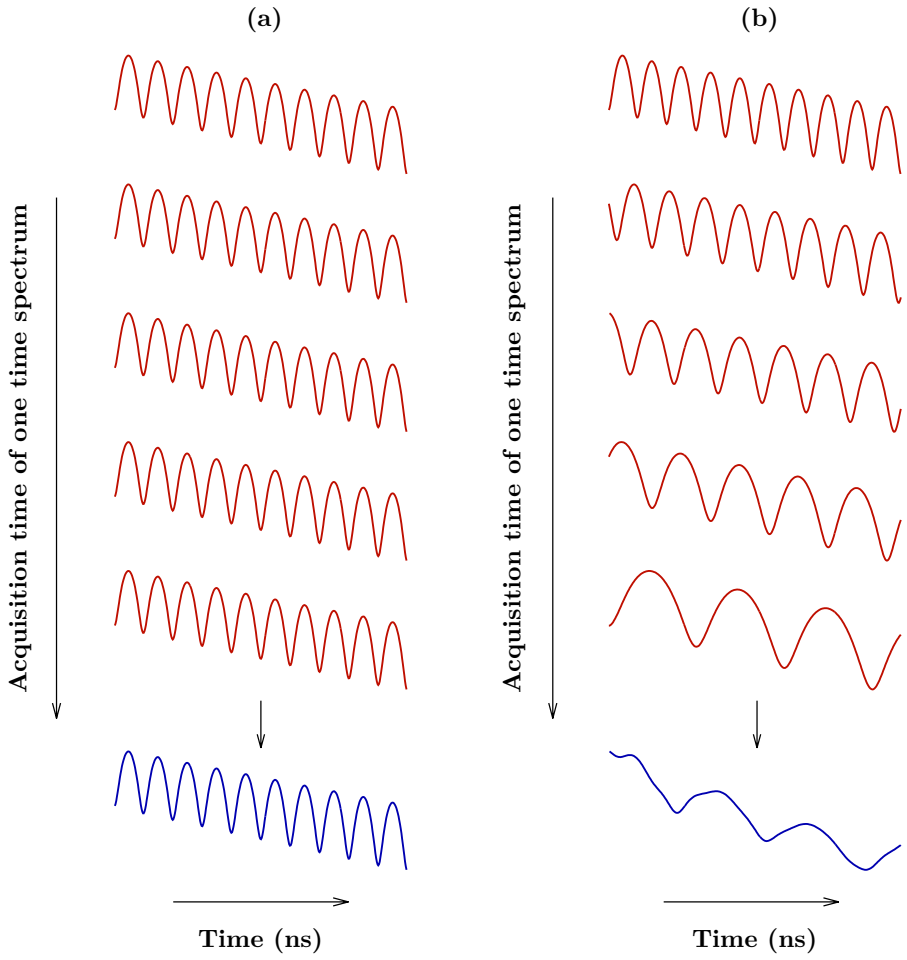

Figure 4.7: A schematic demonstration of a time spectrum acquisition, where the red lines show time sub-spectra collected during the acquisition time and the blue lines are the resulting time spectra. In (a) the spectrum is being collected in a static state. The (b) case demonstrates a process where the time sub-spectra are changing, which results in an incoherent sub-spectra summation.

To make the software settings as simple as possible, the incoherent time spectra $\widehat{I}(t)$ are set by the same parameters as the conventional distributions of the hyperfine parameters. Therefore v_j can be generated by the same distribution types $f_{0,1,2}$, $f^{(2)}_{0,1,2}$, $f^{(3)}_{0,1,2}$. From the user point of view, the only difference is in the interpretation of the distributions. The conventional distributions describe a system consisting of multiple nuclear sites, each with slightly different hyperfine parameters, but all of them present simultaneously in the sample. The distributions defined in this section describe a time evolution of hyperfine parameters of a given nuclear site during the time spectrum acquisition.

4.4 Development

The presented software package is under a continuous development as there are many topics in the nuclear resonant scattering data evaluation which deserve to be addressed. Here, we list some of the current goals to be solved in the near future for the software package to be a more versatile tool for the evaluation of the time and energy domain spectra.

Although ERNST was originally developed for the time domain NFS measurements, it may be also used for Mössbauer spectra analysis in the energy domain. To provide a proper comparison of the calculated spectra to the measured ones a convolution of the transmitted radiation intensity with the incident radiation source line (see section 1.3.1) must be performed. Depending on the shape of the source line, different techniques could be utilized. For a conventional transmission Mössbauer spectroscopy a single Lorentzian source line

$$L_{\mathrm{s}}(E) \propto \frac{\Gamma_{\mathrm{s}}}{\left(E - \Delta E_{\mathrm{s}}\right)^2 + \left(\Gamma_{\mathrm{s}}/2\right)^2} \tag{4.7}$$

is usually used. Γ_{s} is a linewidth (full-width at half-maximum FWHM) of the source line and ΔE_{s} is the source transition energy. Mössbauer spectroscopy can be also realized with the synchrotron Mössbauer source (SMS), where the spectrum is convoluted with $L_{\mathrm{s}}^2(E)$ [95]. In the resonant Mössbauer spectroscopy $L_{\mathrm{s}}(E)L_{\mathrm{d}}(E)$ is used in the convolution [103], where $L_{\mathrm{d}}(E)$ is the resonant detector absorption line, which could be defined analogously to the formula (4.7).

For an efficient evaluation of the experimental data by the developed software package an appropriate fitting procedure will be implemented. Several different approaches could be considered. Among them, the widely used procedure based on the least squares fitting and the minimization of the χ^2 could be a good candidate. However, an additional implementation of more advanced procedures could be desirable to help solving more complex problems with a large number of parameters. Several possibilities can be considered including those outlined in section 1.3.5. Furthermore, regarding the texture measurements or combined energy and time domain measurements, a simultaneous evaluation of several data sets might also be profitable.

Finally, the implementation of the texture into the software can be realized using the texture description from chapter 3 and appendix B. Mössbauer spectra and NFS time spectra could be calculated for an arbitrary combination of the texture coefficients. For reconstructing the coefficients from a set of nuclear resonant measurements an appropriate evaluation method or a set of methods need to be chosen, as discussed previously.

Conclusions

This thesis presented a theoretical description of the coherent elastic nuclear resonant scattering in the forward direction applied to inhomogeneous scattering systems. The results showed that the spatial inhomogeneities along the direction of the incoming photons can be measured by nuclear resonant methods, ensuring several conditions on the studied system and the used radiation source. A method for revealing inhomogeneously distributed hyperfine interactions from two sets of measurements was introduced. It is based on the violation of rotational invariance (VRI), experimentally observed as a difference in the detected radiation intensities caused by a rotation of the sample by 180 ° around one of the radiation polarization axes.

There is a significant connection between VRI and directional distributions of hyperfine interactions within a studied system. The intensity differences can be observed only if the system exhibits a texture (either as an inner property or externally induced). This is related to the polarization effects which accompany the VRI. The observation of VRI also requires a sufficiently high effective thickness of the sample. The non-invariance under the rotation arises from the multiple scattering of photons which exhibits a non-commutative nature.

A general description of the electric or magnetic texture was described in this work. The transmission Mössbauer spectra and NFS time spectra can be calculated for an arbitrary texture function, parametrized using the texture coefficients in the spherical harmonics basis. Regardless of the used method or the sample approximation the nuclear resonant scattering utilizing the ^{57}Fe magnetic dipole transition is affected only by the texture coefficients $D_{l,m}$ with $l \leq 2$. The amount of available information on the texture and the applicable evaluation procedures depend on the used method, the incident radiation polarization and the sample thickness.

The ERNST software package has been developed for treating both energy domain TMS and time domain NFS experiments. The theoretical data can be computed and compared to the measured spectra. More advanced procedures are gradually implemented into the software in order to react to increasing demands on the NRS evaluation.

In conclusion, the TMS and NFS experimental techniques can provide detailed information on the local properties of the resonant nuclei surroundings. They can be used for investigating highly complicated materials with an inhomogeneous spatial distribution of nuclear sites. The utilization of these methods constantly advances as both the experimental realization and the data analysis procedures develop. Consequently, the amount of information available from experiments, which become more and more sophisticated in time, increases.

References

[1] U. Gonser, *Mössbauer Spectroscopy*, Springer-Verlag Berlin Heidelberg, 1975.

[2] P. Gütlich, E. Bill and A. X. Trautwein, *Mössbauer Spectroscopy and Transition Metal Chemistry*, Springer-Verlag Berlin Heidelberg, 2011.

[3] R. Zbořil, M. Mashlan and D. Petridis, "Iron(III) oxides from thermal processes - synthesis, structural and magnetic properties, Mössbauer spectroscopy characterization, and applications," Chem. Matter. **14**, 969–982 (2002).

[4] E. Kuzmann, S. Nagy and A. Vertes, "Critical review of analytical applications of Mössbauer spectroscopy illustrated by mineralogical and geological examples (IUPAC technical report)," Pure Appl. Chem. **75**, 801–858 (2003).

[5] M. I. Oshtrakh, "Application of Mössbauer spectroscopy in biomedical research," Cell Biochem. Biophys. **77**, 15–32 (2019).

[6] P. Gütlich, "Fifty years of Mössbauer spectroscopy in solid state research - remarkable achievements, future perspectives," Z. Anorg. Allg. Chem. **638**, 15–43 (2012).

[7] J. J. Sakurai, *Modern Quantum Mechanics*, Rev. ed., Addison Wesley, 1994.

[8] W. N. Cottingham and D. A. Greenwood, *An Introduction to Nuclear Physics*, 2nd ed., Cambridge University Press, 2001.

[9] D. Craik, *Magnetism: Principles and Applications*, Wiley, 1995.

[10] B. Sedlák and R. N. Kuz'min, *Jaderné Resonanční Metody ve Fyzice Pevných Látek*, Praha: SPN, 1978.

[11] R. Röhlsberger, *Nuclear Condensed Matter Physics with Synchrotron Radiation: Basic Principles, Methodology and Applications*, Springer-Verlag Berlin Heidelberg, 2004.

[12] M. Blume, "Magnetic relaxation and asymmetric quadrupole doublets in the Mössbauer effect," Phys. Rev. Lett. **14**, 96–98 (1965).

[13] E. Bradford and W. Marshall, "Mössbauer absorption in the presence of electron spin relaxation," Proc. Phys. Soc. **87**, 731–747 (1966).

[14] N. N. Greenwood and T. C. Gibb, *Mössbauer Spectroscopy*, Chapman & Hall, 1971.

[15] C. J. Voyer and D. H. Ryan, "A complete solution to the Mössbauer problem, all in one place," Hyperfine Interact. **170**, 91–104 (2006).

[16] B. Sedlák and I. Štoll, *Elektřina a magnetismus*, Karolinum, 2012.

[17] P. Novak, M. Kolar, L. Machala, K. M. Siskova, F. Karlicky, M. Petr and R. Zboril, "Transformations of ferrates(IV,V,VI) in liquids: Mössbauer spectroscopy of frozen solutions," Phys. Chem. Chem. Phys. **20**, 30247–30256 (2018).

[18] M. A. Morrison and G. A. Parker, "A guide to rotations in quantum mechanics," Aust. J. Phys. **40**, 465–497 (1987).

[19] M. E. Rose, *Elementary Theory of Angular Momentum*, Wiley, 1957.

[20] A. Abragam, *Principles of Nuclear Magnetism*, Clarendon Press, 1961.

[21] C. P. Slichter, *Principles of Magnetic Resonance*, Harper & Row, 1963.

[22] E. E. Alp, W. Sturhahn, T. S. Toellner, J. Zhao, M. Hu and D. E. Brown, "Vibrational dynamics studies by nuclear resonant inelastic X-ray scattering," Hyperfine Interact. **144/145**, 3–20 (2002).

[23] M. Y. Hu, W. Sturhahn, T. S. Toellner, P. D. Mannheim, D. E. Brown, J. Zhao and E. E. Alp, "Measuring velocity of sound with nuclear resonant inelastic x-ray scattering," Phys. Rev. B **67**, 094304 (2003).

[24] N. Dauphas, M. Roskosz, E. E. Alp, D. R. Neuville, M. Y. Hu, C. K. Sio, F. L. H. Tissot, J. Zhao, L. Tissandier, E. Médard and C. Cordier, "Magma redox and structural controls on iron isotope variation in Earth's mantle and crust," Earth Planet. Sci. Lett. **398**, 127–140 (2014).

[25] W. Sturhahn, "CONUSS and PHOENIX: Evaluation of nuclear resonant scattering data," Hyperfine Interact. **125**, 149–172 (2000).

[26] R. L. Mössbauer, "Kernresonanzfluoreszenz von Gammastrahlung in Ir^{191}," Z. Phys. **151**, 124–143 (1958).

[27] W. A. Steyert and R. D. Taylor, "Lattice dynamical studies using absolute measurements of the Lamb-Mössbauer recoil-free fraction," Phys. Rev. **134**, A716–A722 (1964).

[28] K. Szymański, L. Dobrzyński, D. Satuła and W. Olszewski, "Recoilless fraction determination by internal standard," Nucl. Instr. Meth. Phys. Res. B **268**, 2815–2819 (2010).

[29] U. Bergmann, S. D. Shastri, D. P. Siddons, B. W. Batterman and J. B. Hastings, "Temperature dependence of nuclear forward scattering of synchrotron radiation in α-^{57}Fe," Phys. Rev. B **50**, 5957–5961 (1994).

[30] G. N. Belozerski, *Mossbauer Studies of Surface Layers*, Elsevier, 1993.

[31] W. Sturhahn, "Nuclear resonant spectroscopy," J. Phys.: Condens. Matter **16**, S497–S530 (2004).

[32] M. Blume and O. C. Kistner, "Resonant absorption in the presence of Faraday rotation," Phys. Rev. **171**, 417–425 (1968).

[33] H. Frauenfelder, D. E. Nagle, R. D. Taylor, D. R .F. Cochran and W. M. Visscher, "Elliptical polarization of Fe^{57} gamma rays," Phys. Rev. **126**, 1065–1075 (1962).

[34] W. Sturhahn, E. Gerdau, "Evaluation of time-differential measurements of nuclear-resonance scattering of x rays," Phys. Rev. B **49**, 9285–9294 (1994).

[35] J. P. Hannon and G. T. Trammell, "Coherent γ-ray optics," Hyperfine Interact. **123/124**, 127–274 (1999).

[36] D. E. Brown, "Nuclear dynamical diffraction using synchrotron radiation," Ph.D. thesis, Stanford University, 1993.

[37] R. M. Housley, R. W. Grant and U. Gonser, "Coherence and polarization effects in Mössbauer absorption by single crystals," Phys. Rev. **178**, 514–522 (1969).

[38] D. P. Siddons, U. Bergmann and J. B. Hastings, "Polarization effects in resonant nuclear scattering," Hyperfine Interact. **123/124**, 681–719 (1999).

[39] A. Q. R. Baron, "Resonant nuclear scattering of synchrotron radiation: Detector development and specular scattering from a thin layer of ^{57}Fe," Ph.D. thesis, Stanford University, 1995.

[40] C. L'abbé, R. Callens and J. Odeurs, "Time-integrated synchrotron Mössbauer spectroscopy," Hyperfine Interact. 135, 275–294 (2001).

[41] G. A. Pasquevich, P. Mendoza Zélis, A. Lencina, A. Veiga, M. B. Fernández van Raap and F. H. Sánchez, "Mössbauer magnetic scan experiments," Nucl. Instr. Meth. Phys. Res. B **328**, 48–58 (2014).

[42] I. Serdons, "Application of stroboscopic detection of nuclear forward scattered synchrotron radiation," Ph.D. thesis, Katholieke Universiteit Leuven, 2005.

[43] T. Zemčik, "Mössbauer spectroscopy and structural analysis of solids," Fresenius J. Anal. Chem. **349**, 26–31 (1994).

[44] L. Machala, J. Tuček and R. Zbořil, "Polymorphous transformations of nanometric iron(III) oxide: A review," Chem. Mater. **23**, 3255–3272 (2011).

[45] G. A. Sawatzky, F. Van Der Woude and A. H. Morrish, "Mössbauer study of several ferrimagnetic spinels," Phys. Rev. **187**, 747–757 (1969).

[46] M. Miglierini, J. Kohout, A. Lančok and K. Šafářová, "Magnetic hyperfine fields of Nanoperm alloys," Acta Phys. Pol. A **121**, 1263–1265 (2011).

[47] M. Miglierini, "Mössbauer-effect study of the hyperfine field distributions in the residual amorphous phase of Fe-Cu-Nb-Si-B nanocrystalline alloys," J. Phys.: Condens. Matter **6**, 1431–1438 (1994).

[48] "RITVERC GmbH radioisotope products," [online], [visited on 2019-06-10], Available from: http://ritverc.com/products/detail.php?ID=1691

[49] E. Kankeleit, "Feedback in Electromechanical Drive Systems," Ed. I. J. Gruverman, *Mössbauer Effect Methodology*, Springer US, 1965.

[50] K. Szymański, L. Dobrzyński, B. Prus and M. J. Cooper, "A single line circularly polarised source for Mössbauer spectroscopy," Nucl. Instr. Meth. Phys. Res. B **119**, 438–441 (1996).

[51] D. Satuła, K. Szymański and L. Dobrzyński, "A single line linearly polarized source for Mössbauer spectroscopy," Nucl. Instr. Meth. Phys. Res. B **269**, 2504–2508 (2011).

[52] H. Wiedemann, *Particle Accelerator Physics*, 3rd ed., Springer-Verlag Berlin Heidelberg, 2007.

[53] R. Rüffer and A. I. Chumakov, "Nuclear resonance beamline at ESRF," Hyperfine Interact. **97/98**, 589–604 (1996).

[54] O. Leupold, A. I. Chumakov, E. E. Alp, W. Sturhahn and A. Q. R. Baron, "Noniron isotopes," Hyperfine Interact. **123/124**, 611–631 (1999).

[55] G. T. Trammell and J. P. Hannon, "Quantum beats from nuclei excited by synchrotron pulses," Phys. Rev. B **18**, 165–172 (1978).

[56] E. Gerdau, R. Rüffer and R. Hollatz, "Quantum beats from nuclei excited by synchrotron radiation," Phys. Rev. Lett. **57**, 1141–1144 (1986).

[57] Such option is provided in the CONUSS software package.

[58] G. K. Shenoy and R. Röhlsberger, "Scientific opportunities in nuclear resonance spectroscopy from source-driven revolution," Hyperfine Interact. **182**, 157–172 (2008).

[59] M. Seto, "Condensed matter physics using nuclear resonant scattering," J. Phys. Soc. Jpn. **82**, 021016 (2013).

[60] G. Vogl and B. Sepiol, "Diffusion in crystalline materials," Hyperfine Interact. **123/124**, 595–609 (1999).

[61] M. Miglierini, M. Pavlovič, V. Procházka, T. Hatala, G. Schumacher and R. Rüffer, "Evolution of structure and local magnetic fields during crystallization of HITPERM glassy alloys studied by *in situ* diffraction and nuclear forward scattering of synchrotron radiation," Phys. Chem. Chem. Phys. **17**, 28239–28249 (2015).

[62] L. Machala, V. Procházka, M. Miglierini, V. K. Sharma, Z. Marušák, H. C. Wille and R. Zbořil, "Direct evidence of Fe(v) and Fe(iv) intermediates during reduction of Fe(vi) to Fe(iii): a nuclear forward scattering of synchrotron radiation approach," Phys. Chem. Chem. Phys. **17**, 21787–21790 (2015).

[63] Z. Klencsár, "Transmission integral analysis of Mössbauer spectra displaying hyperfine parameter distributions with arbitrary profile," AIP Conf. Proc. **1622**, 30–39 (2014).

[64] G. V. Smirnov, "General properties of nuclear resonant scattering," Hyperfine Interact. **123/124**, 31–77 (1999).

[65] Yu. Kagan, "Theory of coherent phenomena and fundamentals in nuclear resonant scattering," Hyperfine Interact. **123/124**, 83–126 (1999).

[66] Yu. V. Shvyd'ko, U. van Bürck, W. Potzel, P. Schindelmann, E. Gerdau, O. Leupold, J. Metge, H. D. Rüter and G. V. Smirnov, "Hybrid beat in nuclear forward scattering of synchrotron radiation," Phys. Rev. B **57**, 3552–3561 (1998).

[67] F. Susanto and P. de Souza, Jr., "Mössbauer spectral curve fitting combining fundamentally different techniques," Nucl. Instr. Meth. Phys. Res. B **385**, 40–45 (2016).

[68] Z. Klencsár, "Mössbauer spectrum analysis by Evolution Algorithm," Nucl. Instr. Meth. Phys. Res. B **129**, 527–533 (1997).

[69] H. Ahonen, P. de Souza, Jr. and V. K. Garg, "A genetic algorithm for fitting Lorentzian line shapes in Mössbauer spectra," Nucl. Instr. Meth. Phys. Res. B **124**, 633–638 (1997).

[70] N. Planckaert, J. Demeulemeester, B. Laenens, D. Smeets, J. Meersschaut, C. L'abbé, K. Temst and A. Vantomme, "Artificial neural networks applied to the analysis of synchrotron nuclear resonant scattering data," J. Synchrotron Rad. **17**, 86–92 (2010).

[71] M. Miglierini, V. Prochazka, S. Stankov, P. Svec, Sr., M. Zajac, J. Kohout, A. Lancok, D. Janickovic and P. Svec, "Crystallization kinetics of nanocrystalline alloys revealed by *in situ* nuclear forward scattering of synchrotron radiation," Phys. Rev. B **86**, 020202 (2012).

[72] V. Vrba, V. Procházka, D. Smrčka and M. Miglierini, "Advanced approach to the analysis of a series of *in-situ* nuclear forward scattering experiments," Nucl. Instr. Meth. Phys. Res. B **847**, 111-116 (2017).

[73] V. Vrba, V. Procházka, D. Smrčka and M. Miglierini, "Hubert: Software for efficient analysis of in-situ nuclear forward scattering experiments," AIP Conf. Proc. **1781**, 020013 (2016).

[74] V. Procházka, V. Vrba, D. Smrčka, R. Rüffer, P. Matúš, M. Mašláň and M. Miglierini, "Structural transformation of NANOPERM-type metallic glasses followed *in situ* by synchrotron radiation during thermal annealing in external magnetic field," J. Alloy. Compd. **638**, 398–404 (2015).

[75] H.-D. Pfannes and H. Fischer, "The texture problem in Mössbauer spectroscopy," Appl. Phys. **13**, 317–325 (1977).

[76] L. Deák, L. Bottyán, T. Fülöp, G. Kertész, D. L. Nagy, R. Rüffer, H. Spiering, F. Tanczikó and G. Vankó, "Switching reciprocity on and off in a magneto-optical X-ray scattering experiment using nuclear resonance of α-^{57}Fe foils," Phys. Rev. Lett. **109**, 237402 (2012).

[77] U. Atzmony, S. J. Norton, L. J. Swartzendruber and L. H. Bennet, "Mössbauer imaging: experimental result," Nature **330**, 153–154 (1987).

[78] J. D. Cashion, P. S. Weiser, A. C. McGrath, R. J. Pollard and T. F. Smith, "Imaging Mössbauer spectroscopy - a new technique for materials analysis," Hyperfine Interact. **58**, 2507–2512 (1990).

[79] P. R. Smith, J. D. Cashion and L. J. Brown, "Imaging Mössbauer spectroscopic measurements of an inhomogeneous sample," Hyperfine Interact. **71**, 1503–1506 (1992).

[80] A. Q. R. Baron, "Transverse coherence in nuclear resonant scattering of synchrotron radiation," Hyperfine Interact. **123/124**, 667–680 (1999).

[81] R. S. Preston, S. S. Hanna and J. Heberle, "Mössbauer effect in metallic iron," Phys. Rev. **128**, 2207–2218 (1962)

[82] M. Miglierini and M. Hasiak, "Ion irradiation induced structural modifications of $Fe_{81}Mo_8Cu_1B_{10}$," Phys. Status Solidi A **213**, 1138–1144 (2016).

[83] M. Miglierini, V. Procházka, **V. Vrba**, P. Švec, D. Janičkovič and P. Matúš, "Methods of *ex situ* and *in situ* investigations of structural transformations: The case of crystallization of metallic glasses," J. Vis. Exp. **136**, e57657 (2018).

[84] M. Hasiak and M. Miglierini, "Impact of ion-irradiation upon microstructure and magnetic properties of NANOPERM-type $Fe_{81}Mo_8Cu_1B_{10}$ metallic glass," Acta Phys. Pol. A **133**, 680–683 (2018).

[85] M. Miglierini and J. M. Greneche, "Mössbauer spectrometry of Fe(Cu)MB-type nanocrystalline alloys: I. The fitting model for the Mössbauer spectra," J. Phys.: Condens. Matter **9**, 2303–2319 (1997).

[86] M. Miglierini and J. M. Greneche, "Mössbauer spectrometry of Fe(Cu)MB-type nanocrystalline alloys: II. The topography of hyperfine interactions in Fe(Cu)ZrB alloys," J. Phys.: Condens. Matter **9**, 2321–2347 (1997).

[87] T. Liu, Z. X. Xu, J. Y. Ping and R. Z. Ma, "Mössbauer studies of magnetic texture in nanocrystalline $Fe_{73.5}Cu_1Nb_3Si_{13.5}B_9$ alloy," Hyperfine Interact. **180**, 401–411 (1997).

[88] K. Szymański, "Magnetic texture determination by means of the monochromatic circularly polarized Mössbauer spectroscopy," Nucl. Instr. Meth. Phys. Res. B **134**, 405–412 (1998).

[89] J. M. Greneche, M. Henry and F. Varret, "Internal stresses and spin texture in metglasses MB 2826 from Mössbauer experiments," J. Magn. Magn. Mater. **26**, 153–156 (1982).

[90] J. M. Greneche and F. Varret, "On the texture problem in Mössbauer spectroscopy," J. Phys. C: Solid State Phys. **15**, 5333–5344 (1982).

[91] R. Röhlsberger, J. Bansmann, V. Senz, K. L. Jonas, A. Bettac, O. Leupold, R. Rüffer, E. Burkel and K. H. Meiwes-Broer, "Perpendicular spin orientation in ultrasmall Fe islands on W(110)," Phys. Rev. Lett. **86**, 5597–5600 (2001).

[92] R. Röhlsberger, J. Bansmann, V. Senz, K. L. Jonas, A. Bettac, K. H. Meiwes-Broer and O. Leupold, "Nanoscale magnetism probed by nuclear resonant scattering of synchrotron radiation," Phys. Rev. B **67**, 245412 (2003). R. Röhlsberger, J. Bansmann, V. Senz, K. L. Jonas, A. Bettac, K. H. Meiwes-Broer and O. Leupold, "Publisher's note: Nanoscale magnetism probed by nuclear resonant scattering of synchrotron radiation," Phys. Rev. B **68**, 049901(E) (2003).

[93] R. Callens, C. L'abbé, J. Meersschaut, I. Serdons, W. Sturhahn and T. S. Toellner, "Determination of the magnetic spin direction from the nuclear forward-scattering line intensities," J. Synchrotron Rad. **14**, 366–371 (2007).

[94] R. Röhlsberger, O. Leupold, J. Metge, H. D. Rüter, W. Sturhahn and E. Gerdau, "Nuclear forward scattering of synchrotron radiation from unmagnetized α-^{57}Fe," Hyperfine Interact. **92**, 1107–1112 (1994).

[95] C. Prescher, C. McCammon and L. Dubrovinsky, "*MossA*: a program for analyzing energy-domain Mössbauer spectra from conventional and synchrotron sources," J. Appl. Crystallogr. **45**, 329–331 (2012).

[96] A. I. Rykov, I. A. Rykov, K. Nomura and X. Zhang, "Frequency spectra of quantum beats in nuclear forward scattering of ^{57}Fe: The Mössbauer spectroscopy with superior energy resolution," Hyperfine Interact. **163**, 29–56 (2005).

[97] T. Žák and Y. Jirásková, "CONFIT: Mössbauer spectra fitting program," Surf. Interface Anal. **38**, 710–714 (2006).

[98] Yu. V. Shvyd'ko, "MOTIF: Evaluation of time spectra for nuclear forward scattering," Hyperfine Interact. **125**, 173–188 (2000).

[99] H. Spiering, L. Deák and L. Bottyán, "EFFINO," Hyperfine Interact. **125**, 197–204 (2000).

[100] "Qt," [online], [visited on 2019-06-10], Available from: https://doc.qt.io/qtcreator/index.html

[101] "GSL - GNU Scientific Library," [online], [visited on 2019-06-08], Available from: https://www.gnu.org/software/gsl/doc/html/index.html

[102] "Gnuplot," [online], [visited on 2019-06-08], Available from: http://www.gnuplot.info/

[103] M. Mashlan, A. Kholmetskii, V. Yevdokimov, J. Pechousek, O. Verich, R. Zboril and R. Tsonchev, "Mössbauer spectrometer with resonant detector," Nucl. Instr. Meth. Phys. Res. B **243**, 241–246 (2006).

List of Symbols and Abbreviations

$\vec{A}$	radiation wave field
$\vec{b}$	$\vec{b} = \vec{k}_0 \times \vec{\varepsilon}$
$\vec{B}$	magnetic field
c	speed of light
C	$C = \cos\left[K\left(F_{+1} - F_{-1}\right)\right]$
$C(j_\mathrm{g} 1 j_\mathrm{e}; m_\mathrm{g} M)$	Clebsch-Gordan coefficients
d	thickness
d_eff	effective thickness
$D(\theta, \phi)$	texture function
$D_{l,m}$	texture coefficients
$\hat{\mathcal{D}}$	rotation operator
$\mathcal{D}^{(j)}_{m'm}$	Wigner matrix elements
$E, \mathcal{E}$	energy
ΔE	transition energy
f_LM	Lamb-Mössbauer factor
$f_{0,1,2}$	distribution functions
F_M	F_M factors
$\mathcal{F}$	Fourier transform
g	nuclear g-factor
$G_M^{n_\mathrm{g}, n_\mathrm{e}}$	$G_M^{n_\mathrm{g}, n_\mathrm{e}}$
$\hbar$	reduced Planck's constant
$H, \mathcal{H}$	Hamiltonian
I	intensity
$\mathcal{I}_1, \mathcal{I}_2, \mathcal{I}_3$	intensity contributions
j	nuclear spin quantum number
$\hat{J}$	magnitude of total nuclear angular momentum
$\hat{J}_z$	z-component of total nuclear angular momentum
$\vec{k}, \vec{k}_0$	wave vector and unit wave vector
K	$K = (3\xi)/(16\pi)$
L	number of data points
$L(E)$	Lorentzian function
m	nuclear magnetic quantum number
$\vec{m}_\mathrm{A}, \vec{m}_\mathrm{B}$	magnetic field unit vectors
M	multipole index
n	index of Hamiltonian eigenstates
$n^{n_\mathrm{g}, n_\mathrm{e}}$	$n^{n_\mathrm{g}, n_\mathrm{e}}$ matrices
N	scattering length
N_n	number of neutrons
$\mathcal{N}$	scattering length contribution
p	hyperfine parameter or a set of hyperfine parameters
q_0	elementary electric charge
q_n	total electric charge of a nucleus
Q	nuclear electric quadrupole moment value

$\hat{Q}_{xx}, \hat{Q}_{yy}, \hat{Q}_{zz}$	nuclear electric quadrupole moment diagonal elements
$\vec{r}$	position vector
R_x	range-specifying parameter
$\langle r_{\mathrm{n}}^2 \rangle$	root-mean-square radius of a nucleus
S	$S = \sin\left[K\left(F_{+1} - F_{-1}\right)\right]$
t	time
T	scattering matrix
$\vec{v}_{xx}, \vec{v}_{yy}, \vec{v}_{zz}$	unit vectors of the electric field gradient main axes
v	velocity
V_{ij}	electric field gradient tensor elements
v_i, w_i	weight factors
x	variable hyperfine parameter
$\langle x^2 \rangle$	atomic mean square vibrational amplitude
$\vec{Y}_M(\vec{k})$	vector spherical harmonics
$Y_{l,m}(\theta, \phi)$	real spherical harmonics
`W,X,Y,Z`	integers of a number sequence
$\vec{z}_0$	quantization axis unit vector
Z_{n}	number of protons
α, β, γ	rotation Euler angles
γ_{G}	gyromagnetic ratio
Γ	natural linewidth
$\delta_{m,n}$	Kronecker delta
Δ	quadrupole splitting
$\vec{\varepsilon}$	polarization vector
ε_0	vacuum permittivity
η	asymmetry parameter
θ	magnetic field polar angle
λ	wavelength
$\hat{\mu}$	magnitude of nuclear magnetic dipole moment
μ_{N}	nuclear magneton
$\hat{\mu}_z$	z-component of nuclear magnetic dipole moment
μ, ν, σ, π	polarization indexes
ξ	exponent constant
ρ	density matrix
ϱ	number density of resonant nuclei
σ_0	nuclear resonant effective cross-section
σ_l	standard deviation of the l-th experimental data point
τ	lifetime
ϕ	magnetic field azimuth angle
$\varphi(\vec{r})$	electric field potential
$\varphi_{m,n}, \psi_{m,n}$	eigenvector components
$\lvert\psi\rangle$	quantum state ket
$\lvert\psi(\vec{r})\rvert^2$	electronic probability density
χ^2	χ^2 parameter
Φ, Θ, Ψ	radiation Euler angles
Ω, Λ	orientation dependence

CEMS	conversion electron Mössbauer spectroscopy
CXMS	conversion X-ray Mössbauer spectroscopy
EFG	electric field gradient
ESRF	European Synchrotron Radiation Facility
ERNST	Evaluation of Resonant Nuclear Scattering in energy and Time domain
FWHM	full width at half maximum
GSL	GNU Scientific Library
HWHM	half width at half maximum
M1	magnetic dipole transition
NFS	nuclear forward scattering
NRIXS	nuclear resonant inelastic X-ray scattering
NRS	nuclear resonant scattering
SMS	synchrotron Mössbauer source
TMS	transmission Mössbauer spectroscopy
VRI	violation of rotational invariance

List of Publications

[I] V. Procházka, **V. Vrba**, D. Smrčka, R. Rüffer, P. Matúš, M. Mašláň and M. Miglierini, "Structural transformation of NANOPERM-type metallic glasses followed *in situ* by synchrotron radiation during thermal annealing in external magnetic field," J. Alloy. Compd. **638**, 398–404 (2015).

[II] **V. Vrba**, V. Procházka, D. Smrčka and M. Miglierini, "Hubert: Software for efficient analysis of in-situ nuclear forward scattering experiments," AIP Conf. Proc. **1781**, 020013 (2016).

[III] V. Procházka, **V. Vrba**, P. Šretrová, D. Smrčka and M. Miglierini, "Preferential magnetic orientation in amorphous alloys determined by NFS and Mössbauer spectroscopy," AIP Conf. Proc. **1781**, 020014 (2016).

[IV] D. Smrčka, V. Procházka, P. Novák, J. Kašlík and **V. Vrba**, "Iron oxalate decomposition process by means of Mössbauer spectroscopy and nuclear forward scattering," AIP Conf. Proc. **1781**, 020012 (2016).

[V] P. Novák, J. Pechoušek, V. Procházka, J. Navařík, L. Kouřil, P. Kohout, **V. Vrba** and L. Machala, "Time differential ^{57}Fe Mössbauer spectrometer with unique 4π YAP:Ce 122.06 keV gamma-photon detector," Nucl. Instr. Meth. Phys. Res. A **832**, 292–296 (2016).

[VI] **V. Vrba**, V. Procházka, D. Smrčka and M. Miglierini, "Advanced approach to the analysis of a series of *in-situ* nuclear forward scattering experiments," Nucl. Instr. Meth. Phys. Res. A **847**, 111–116 (2017).

[VII] M. Miglierini, V. Procházka, **V. Vrba**, P. Švec, D. Janičkovič and P. Matúš, "Methods of *ex situ* and *in situ* investigations of structural transformations: The case of crystallization of metallic glasses," J. Vis. Exp. **136**, e57657 (2018).

[VIII] **V. Vrba**, V. Procházka and M. Miglierini, "Identification of spatial magnetic inhomogeneities by nuclear forward scattering of synchrotron radiation," J. Synchrotron Rad. **26** (2019), Accepted for publication.

[IX] D. Smrčka, V. Procházka, **V. Vrba** and M. Miglierini, "Nuclear forward scattering analysis of crystallization processes in weakly magnetic metallic glasses," J. Alloys Compd. **793**, 672–677 (2019).

[X] D. Smrčka, V. Procházka, **V. Vrba** and M. Miglierini, "On the formation of nanocrystalline grains in metallic glasses by means of in-situ nuclear forward scattering of synchrotron radiation ," Nanomaterials **9**, 544 (2019).

Appendix A: Thickness Effect on VRI for Two Layers

Consider a scattering system consisting of two homogeneous layers with arbitrary (but significantly high) effective thickness $d_{\mathrm{eff,A}}$ for layer A and $d_{\mathrm{eff,B}}$ for layer B. The scattering matrices of the layers can be written as

$$T_{\mathrm{A}} = \mathrm{e}^{i\xi_{\mathrm{A}}N_{\mathrm{A}}} = \mathbf{1} + i\xi_{\mathrm{A}}N_{\mathrm{A}} - \frac{\xi_{\mathrm{A}}^2 N_{\mathrm{A}}^2}{2} - i\,\frac{\xi_{\mathrm{A}}^3 N_{\mathrm{A}}^3}{6} + \dots\,, \tag{A.1}$$

$$T_{\mathrm{B}} = \mathrm{e}^{i\xi_{\mathrm{B}}N_{\mathrm{B}}} = \mathbf{1} + i\xi_{\mathrm{B}}N_{\mathrm{B}} - \frac{\xi_{\mathrm{B}}^2 N_{\mathrm{B}}^2}{2} - i\,\frac{\xi_{\mathrm{B}}^3 N_{\mathrm{B}}^3}{6} + \dots\,, \tag{A.2}$$

where

$$\xi_{\mathrm{A}} = -\frac{\pi\Gamma d_{\mathrm{eff,A}}}{2}\,, \quad \xi_{\mathrm{B}} = -\frac{\pi\Gamma d_{\mathrm{eff,B}}}{2} \tag{A.3}$$

and the scattering lengths N_{A}, N_{B} are given by formula (1.31). The total scattering matrix of the system (see Fig. 2.6a for comparison) is given as

$$T = T_{\mathrm{B}}T_{\mathrm{A}} = \mathbf{1} + i\xi_{\mathrm{A}}N_{\mathrm{A}} + i\xi_{\mathrm{B}}N_{\mathrm{B}} - \frac{\xi_{\mathrm{A}}^2 N_{\mathrm{A}}^2}{2} - \xi_{\mathrm{A}}\xi_{\mathrm{B}}N_{\mathrm{B}}N_{\mathrm{A}} - \frac{\xi_{\mathrm{B}}^2 N_{\mathrm{B}}^2}{2} + \dots\,, \tag{A.4}$$

where the expansion terms up to the second order are explicitly shown. The terms which represent a mixed multiple scattering with photons being scattered on both system layers are marked in red. The scattering matrix T^{rot} of the system after its 180 ° rotation, e.g. around the $\vec{\varepsilon}_\pi$-axis, is then

$$\begin{aligned} T^{\mathrm{rot}} = T_{\mathrm{A}}^{\mathrm{rot}}T_{\mathrm{B}}^{\mathrm{rot}} = \mathbf{1} + i\xi_{\mathrm{A}}N_{\mathrm{A}}^{\mathrm{rot}} + i\xi_{\mathrm{B}}N_{\mathrm{B}}^{\mathrm{rot}} - \frac{\xi_{\mathrm{A}}^2 \left(N_{\mathrm{A}}^{\mathrm{rot}}\right)^2}{2} - \\ - \xi_{\mathrm{A}}\xi_{\mathrm{B}}N_{\mathrm{A}}^{\mathrm{rot}}N_{\mathrm{B}}^{\mathrm{rot}} - \frac{\xi_{\mathrm{B}}^2 \left(N_{\mathrm{B}}^{\mathrm{rot}}\right)^2}{2} + \dots\,. \end{aligned} \tag{A.5}$$

The comparison of (A.4) and (A.5) shows that the rotated and non-rotated quantities are related by substitutions $\xi_{\mathrm{A}}N_{\mathrm{A}} \to \xi_{\mathrm{B}}N_{\mathrm{B}}^{\mathrm{rot}}$ and $\xi_{\mathrm{B}}N_{\mathrm{B}} \to \xi_{\mathrm{A}}N_{\mathrm{A}}^{\mathrm{rot}}$, which will be used in the following part.

The transmitted radiation intensity I_{tr} before the rotation follows the general formula (1.43), where the Hermitian conjugate of T is given as

$$T^{\dagger} = \mathbf{1} - i\xi_{\mathrm{A}}N_{\mathrm{A}}^{\dagger} - i\xi_{\mathrm{B}}N_{\mathrm{B}}^{\dagger} - \frac{\xi_{\mathrm{A}}^2 \left(N_{\mathrm{A}}^{\dagger}\right)^2}{2} - \xi_{\mathrm{A}}\xi_{\mathrm{B}}N_{\mathrm{A}}^{\dagger}N_{\mathrm{B}}^{\dagger} - \frac{\xi_{\mathrm{B}}^2 \left(N_{\mathrm{B}}^{\dagger}\right)^2}{2} + \dots\,. \tag{A.6}$$

I_{tr} can be written as a sum $I_{\mathrm{tr},1} + I_{\mathrm{tr},2} + I_{\mathrm{tr},3} + \dots$, where the first contribution $I_{\mathrm{tr},1}$ includes the intensity terms which are at most linear in either ξ_{A} or ξ_{B}, the second contribution $I_{\mathrm{tr},2}$ includes the terms which are proportional to ξ_{A}^2, ξ_{B}^2 and $\xi_{\mathrm{A}}\xi_{\mathrm{B}}$, the third contribution $I_{\mathrm{tr},3}$ includes all the cubic terms, etc. The same expansion could be performed on the rotated intensity $I_{\mathrm{tr}}^{\mathrm{rot}}$.

Using the properties of a matrix trace, the first contribution to transmitted intensities before the rotation can be written as

$$I_{\mathrm{tr},1} = \mathrm{Tr}\left[\rho + i\rho\xi_{\mathrm{A}}N_{\mathrm{A}} - i\rho\xi_{\mathrm{A}}N_{\mathrm{A}}^{\dagger} + i\rho\xi_{\mathrm{B}}N_{\mathrm{B}} - i\rho\xi_{\mathrm{B}}N_{\mathrm{B}}^{\dagger}\right] \tag{A.7}$$

and the corresponding rotated contribution is

$$I_{\mathrm{tr},1}^{\mathrm{rot}} = \mathrm{Tr}\left[\rho + i\rho\xi_{\mathrm{A}} N_{\mathrm{A}}^{\mathrm{rot}} - i\rho\xi_{\mathrm{A}}\left(N_{\mathrm{A}}^{\mathrm{rot}}\right)^{\dagger} + i\rho\xi_{\mathrm{B}} N_{\mathrm{B}}^{\mathrm{rot}} - i\rho\xi_{\mathrm{B}}\left(N_{\mathrm{B}}^{\mathrm{rot}}\right)^{\dagger}\right]. \tag{A.8}$$

The linear terms in $I_{\mathrm{tr},1}$ and $I_{\mathrm{tr},1}^{\mathrm{rot}}$ may contribute to VRI only if the difference $\Delta I_{\mathrm{tr},1}$ given as $I_{\mathrm{tr},1} - I_{\mathrm{tr},1}^{\mathrm{rot}}$ is not a zero. Simplification of $\Delta I_{\mathrm{tr},1}$ leads to formula

$$\begin{aligned}\Delta I_{\mathrm{tr},1} = \mathrm{Tr}\Big[&i\rho\xi_{\mathrm{A}}\left(N_{\mathrm{A}} - N_{\mathrm{A}}^{\mathrm{rot}}\right) + i\rho\xi_{\mathrm{A}}\left(N_{\mathrm{A}} - N_{\mathrm{A}}^{\mathrm{rot}}\right)^{\dagger} + \\ &+ i\rho\xi_{\mathrm{B}}\left(N_{\mathrm{B}} - N_{\mathrm{B}}^{\mathrm{rot}}\right) + i\rho\xi_{\mathrm{B}}\left(N_{\mathrm{B}} - N_{\mathrm{B}}^{\mathrm{rot}}\right)^{\dagger}\Big].\end{aligned} \tag{A.9}$$

The individual differences in the round brackets are anti-diagonal (their diagonal elements equal zero), because the rotated scattering lengths follow relation (2.2) with respect to the non-rotated ones. For the considered cases of unpolarized or linearly ($\vec{\varepsilon}_{\sigma}$) polarized radiation the multiplication of the density matrix ρ with these anti-diagonal matrices gives also anti-diagonal matrices, thus the whole $\Delta I_{\mathrm{tr},1}$ equals zero. If the effective thickness of the layers was low enough, the higher intensity contributions would become negligible and the resulting spectrum would be invariant under the considered rotation.

The same procedure can now be applied to the second radiation intensity contribution

$$\begin{aligned}I_{\mathrm{tr},2} = \mathrm{Tr}\Big\{\rho\Big[&\xi_{\mathrm{A}}^2 N_{\mathrm{A}}^{\dagger} N_{\mathrm{A}} + \xi_{\mathrm{A}}\xi_{\mathrm{B}} N_{\mathrm{A}}^{\dagger} N_{\mathrm{B}} + \xi_{\mathrm{A}}\xi_{\mathrm{B}} N_{\mathrm{B}}^{\dagger} N_{\mathrm{A}} + \xi_{\mathrm{B}}^2 \rho N_{\mathrm{B}}^{\dagger} N_{\mathrm{B}} - \\ &- \frac{\xi_{\mathrm{A}}^2 N_{\mathrm{A}}^2}{2} - \frac{\xi_{\mathrm{A}}^2\left(N_{\mathrm{A}}^{\dagger}\right)^2}{2} - \frac{\xi_{\mathrm{B}}^2 N_{\mathrm{B}}^2}{2} - \frac{\xi_{\mathrm{B}}^2\left(N_{\mathrm{B}}^{\dagger}\right)^2}{2} - \xi_{\mathrm{A}}\xi_{\mathrm{B}} N_{\mathrm{B}} N_{\mathrm{A}} - \xi_{\mathrm{A}}\xi_{\mathrm{B}} N_{\mathrm{A}}^{\dagger} N_{\mathrm{B}}^{\dagger}\Big]\Big\}.\end{aligned} \tag{A.10}$$

The rotated intensity $I_{\mathrm{tr},2}^{\mathrm{rot}}$ is related to $I_{\mathrm{tr},2}$ by the same substitutions as for the first case. The terms in (A.10) which arise from the single scattering or the multiple scattering on the same layer (the terms in black) would find their corresponding rotated counterparts in the rotated intensity and the difference $\Delta I_{\mathrm{tr},2} = I_{\mathrm{tr},2} - I_{\mathrm{tr},2}^{\mathrm{rot}}$ would contain analogous terms to those in formula (A.9) which would result in anti-diagonal matrices giving a zero contribution to the intensity difference. On the other hand, the mixed terms (the terms in red) lead to the difference

$$\begin{aligned}\Delta I_{\mathrm{tr},2}^{\mathrm{rot}} = \mathrm{Tr}\Big\{\rho\Big[&- \xi_{\mathrm{A}}\xi_{\mathrm{B}} N_{\mathrm{B}} N_{\mathrm{A}} - \xi_{\mathrm{A}}\xi_{\mathrm{B}} N_{\mathrm{A}}^{\dagger} N_{\mathrm{B}}^{\dagger} + \\ &+ \xi_{\mathrm{A}}\xi_{\mathrm{B}} N_{\mathrm{A}}^{\mathrm{rot}} N_{\mathrm{B}}^{\mathrm{rot}} + \xi_{\mathrm{A}}\xi_{\mathrm{B}}\left(N_{\mathrm{B}}^{\mathrm{rot}}\right)^{\dagger}\left(N_{\mathrm{A}}^{\mathrm{rot}}\right)^{\dagger}\Big]\Big\},\end{aligned} \tag{A.11}$$

which is generally different from zero. Consequently, the second-order mixed multiple scattering terms already contribute to VRI.

The higher-order contributions to the transmitted radiation intensity could be analysed analogously. However, they are not treated here as the number of individual contributions to be analysed is relatively high, the calculations become complicated and are not very illustrative.

Concerning the scattered radiation and VRI in NFS time spectra, the calculations are complicated by the Fourier transform of the matrices. The VRI contributions could be illustrated for the intensity of the scattered radiation in the energy domain, as can be seen in Fig. 2.7 (left column). The intensity I_{sc} could then be evaluated using formulas (A.1–A.4) and

$$I_{\mathrm{sc}} = \mathrm{Tr}\Big[\,(T-\mathbf{1})\,\rho\,(T-\mathbf{1})^{\dagger}\,\Big]. \tag{A.12}$$

By repeating the procedure which was described for the transmitted radiation intensity the individual VRI contributions may be identified. It could be found that the intensity does not exhibit any first-order term. The second-order terms, which give the thin-sample approximation for NFS, would be anti-diagonal. The third-order terms already contain the mixed multiple scattering terms which contribute to VRI.

Appendix B: Scattering Length Expansion in Real Spherical Harmonics

The scattering length N of a nuclear site can be described by $n^{m_\mathrm{g},m_\mathrm{e}}$ matrices according to formulas (1.31–1.33). These matrices depend on the angles of the magnetic (or axially symmetrical electric) field, i.e. $n^{m_\mathrm{g},m_\mathrm{e}} = n^{m_\mathrm{g},m_\mathrm{e}}(\theta,\phi)$. They can be expanded using the real spherical harmonics $Y_{l,m}(\theta,\phi)$, where $l = 0, 1, 2, \ldots$ and $m = -l, -l+1, \ldots, l-1, l$. The spherical harmonic functions form an orthonormal basis reflected by formula

$$\int_0^{2\pi}\int_0^{\pi} Y_{l,m}(\theta,\phi)Y_{l',m'}(\theta,\phi)\sin\theta\,\mathrm{d}\theta\mathrm{d}\phi = \delta_{ll'}\delta_{mm'}\,. \tag{B.1}$$

The expansion of $n^{m_\mathrm{g},m_\mathrm{e}}(\theta,\phi)$ can be written as

$$n^{m_\mathrm{g},m_\mathrm{e}}(\theta,\phi) = \sum_{l=0}^{\infty}\sum_{m=-l}^{l} n_{l,m}^{m_\mathrm{g},m_\mathrm{e}}\,Y_{l,m}(\theta,\phi), \tag{B.2}$$

where the coefficient matrices $n_{l,m}^{m_\mathrm{g},m_\mathrm{e}}$ can be obtained by an integral

$$n_{l,m}^{m_\mathrm{g},m_\mathrm{e}} = \int_0^{2\pi}\int_0^{\pi} n^{m_\mathrm{g},m_\mathrm{e}}(\theta,\phi)Y_{l,m}(\theta,\phi)\sin\theta\,\mathrm{d}\theta\mathrm{d}\phi. \tag{B.3}$$

Once the $n_{l,m}^{m_\mathrm{g},m_\mathrm{e}}$ coefficient matrices are known the scattering length can be generally written as a sum

$$N(\theta,\phi) = \sum_{l=0}^{\infty}\sum_{m=-l}^{l}\sum_{m_\mathrm{g},m_\mathrm{e}} L_{m_\mathrm{g}}^{m_\mathrm{e}}(E)\,n_{l,m}^{m_\mathrm{g},m_\mathrm{e}}\,Y_{l,m}(\theta,\phi). \tag{B.4}$$

The dependence of $n^{m_\mathrm{g},m_\mathrm{e}}(\theta,\phi)$ on the field directions is contained in eigenvector components of the interaction Hamiltonian, see the $G_M^{m_\mathrm{g},m_\mathrm{e}}$ factors in (1.30). For the considered symmetrical case the eigenvector components are given by (1.23). It could be found that the specific angular dependences result in non-zero $n_{l,m}^{m_\mathrm{g},m_\mathrm{e}}$ only for $l \le 2$ and so the sum in (B.4) runs only over $l = 0, 1, 2$. The corresponding real spherical harmonics are explicitly given as [1]

$$\begin{aligned}
&Y_{0,0}(\theta,\phi) = \frac{1}{\sqrt{4\pi}}\,,\quad Y_{1,-1}(\theta,\phi) = -\sqrt{\frac{3}{4\pi}}\sin\theta\sin\phi\,,\\
&Y_{1,0}(\theta,\phi) = \sqrt{\frac{3}{4\pi}}\cos\theta\,,\quad Y_{1,1}(\theta,\phi) = -\sqrt{\frac{3}{4\pi}}\sin\theta\cos\phi\,,\\
&Y_{2,-2}(\theta,\phi) = \sqrt{\frac{15}{16\pi}}\sin^2\theta\sin 2\phi\,,\quad Y_{2,-1}(\theta,\phi) = -\sqrt{\frac{15}{16\pi}}\sin 2\theta\sin\phi\,,\\
&Y_{2,0}(\theta,\phi) = \sqrt{\frac{5}{16\pi}}\left(3\cos^2\theta - 1\right)\,,\quad Y_{2,1}(\theta,\phi) = -\sqrt{\frac{15}{16\pi}}\sin 2\theta\cos\phi\,,\\
&Y_{2,2}(\theta,\phi) = \sqrt{\frac{15}{16\pi}}\sin^2\theta\cos 2\phi\,.
\end{aligned} \tag{B.5}$$

The computation of $n_{l,m}^{m_g,m_e}$ was performed using Wolfram Mathematica software [2]. To verify the zero higher-order contributions and correctness of the calculations the coefficient matrices were determined for the l values going form 0 up to 6. As the angular dependence of $n^{m_g,m_e}(\theta,\phi)$ is not trivial the symbolic computations for higher orders become rather time consuming. The $n_{l,m}^{m_g,m_e}$ matrices for $l = 0, 1, 2$ and $m = -l, -l+1 \ldots, l-1, l$ are shown on the following pages for three selected transitions between the nuclear energy levels.

It might be noted that, physically, the integration in (B.3) does not reflect the rotation of the sample, but the directional distribution with respect to the laboratory reference frame. For rotating the sample with respect to the radiation coordinate system, the Euler angles of the radiation system can be utilized. In this appendix these angles are denoted as α, β, γ. Their usage for the sample rotation is based on the relation between the active rotation of the physical system and corresponding passive rotation of the (radiation) coordinate system [3]. Thus, for a chosen rotation of the sample the corresponding values of α, β, γ can be substituted into the $n_{l,m}^{m_g,m_e}$ matrices.

Matrix-form coefficients of $n^{m_{\mathrm{g}},m_{\mathrm{e}}}$ for $m_{\mathrm{g}}=-\frac{1}{2}$ and $m_{\mathrm{e}}=-\frac{3}{2}$:

$$n_{0,0}^{-\frac{1}{2},-\frac{3}{2}}=\begin{pmatrix}\frac{1}{4\sqrt{\pi}} & 0\\ 0 & \frac{1}{4\sqrt{\pi}}\end{pmatrix}$$

$$n_{1,-1}^{-\frac{1}{2},-\frac{3}{2}}=\begin{pmatrix}0 & \frac{1}{8}i\sqrt{\frac{3}{\pi}}\sin(\alpha)\sin(\beta)\\ -\frac{1}{8}i\sqrt{\frac{3}{\pi}}\sin(\alpha)\sin(\beta) & 0\end{pmatrix}$$

$$n_{1,0}^{-\frac{1}{2},-\frac{3}{2}}=\begin{pmatrix}0 & -\frac{1}{8}i\sqrt{\frac{3}{\pi}}\cos(\beta)\\ \frac{1}{8}i\sqrt{\frac{3}{\pi}}\cos(\beta) & 0\end{pmatrix}$$

$$n_{1,1}^{-\frac{1}{2},-\frac{3}{2}}=\begin{pmatrix}0 & \frac{1}{8}i\sqrt{\frac{3}{\pi}}\cos(\alpha)\sin(\beta)\\ -\frac{1}{8}i\sqrt{\frac{3}{\pi}}\cos(\alpha)\sin(\beta) & 0\end{pmatrix}$$

$$n_{2,-2}^{-\frac{1}{2},-\frac{3}{2}}=\begin{pmatrix}\frac{1}{8}\sqrt{\frac{3}{5\pi}}\left(\cos(\beta)\left(\cos(2\alpha)\sin(2\gamma)-\sin(2\alpha)\cos(\beta)\sin^2(\gamma)\right)+\sin(2\alpha)\cos^2(\gamma)\right) & -\frac{1}{8}\sqrt{\frac{3}{5\pi}}\cos(2\alpha)\cos(\beta)\\ -\frac{1}{8}\sqrt{\frac{3}{5\pi}}\cos(2\alpha)\cos(\beta) & -\frac{1}{8}\sqrt{\frac{3}{5\pi}}\left(\sin(2\alpha)\cos^2(\beta)\cos^2(\gamma)+\cos(2\alpha)\cos(\beta)\sin(2\gamma)-\sin(2\alpha)\sin^2(\gamma)\right)\end{pmatrix}$$

$$n_{2,-1}^{-\frac{1}{2},-\frac{3}{2}}=\begin{pmatrix}\frac{1}{4}\sqrt{\frac{3}{5\pi}}\sin(\beta)\sin(\gamma)(\cos(\alpha)\cos(\gamma)-\sin(\alpha)\cos(\beta)\sin(\gamma)) & -\frac{1}{8}\sqrt{\frac{3}{5\pi}}\cos(\alpha)\sin(\beta)\\ -\frac{1}{8}\sqrt{\frac{3}{5\pi}}\cos(\alpha)\sin(\beta) & -\frac{1}{4}\sqrt{\frac{3}{5\pi}}\sin(\beta)\cos(\gamma)(\sin(\alpha)\cos(\beta)\cos(\gamma)+\cos(\alpha)\sin(\gamma))\end{pmatrix}$$

$$n_{2,0}^{-\frac{1}{2},-\frac{3}{2}}=\begin{pmatrix}\frac{-3\cos(2(\beta-\gamma))-3\cos(2(\beta+\gamma))+6\cos(2\beta)+6\cos(2\gamma)+2}{64\sqrt{5\pi}} & 0\\ 0 & \frac{3\cos(2(\beta-\gamma))+3\cos(2(\beta+\gamma))+6\cos(2\beta)-6\cos(2\gamma)+2}{64\sqrt{5\pi}}\end{pmatrix}$$

$$n_{2,1}^{-\frac{1}{2},-\frac{3}{2}}=\begin{pmatrix}-\frac{1}{4}\sqrt{\frac{3}{5\pi}}\sin(\beta)\sin(\gamma)(\cos(\alpha)\cos(\beta)\sin(\gamma)+\sin(\alpha)\cos(\gamma)) & \frac{1}{8}\sqrt{\frac{3}{5\pi}}\sin(\alpha)\sin(\beta)\\ \frac{1}{8}\sqrt{\frac{3}{5\pi}}\sin(\alpha)\sin(\beta) & \frac{1}{4}\sqrt{\frac{3}{5\pi}}\sin(\beta)\cos(\gamma)(\sin(\alpha)\sin(\gamma)-\cos(\alpha)\cos(\beta)\cos(\gamma))\end{pmatrix}$$

$$n_{2,2}^{-\frac{1}{2},-\frac{3}{2}}=\begin{pmatrix}\frac{1}{8}\sqrt{\frac{3}{5\pi}}\left(\cos(2\alpha)\left(\cos^2(\gamma)-\cos^2(\beta)\sin^2(\gamma)\right)-4\sin(\alpha)\cos(\alpha)\cos(\beta)\sin(\gamma)\cos(\gamma)\right) & \frac{1}{8}\sqrt{\frac{3}{5\pi}}\sin(2\alpha)\cos(\beta)\\ \frac{1}{8}\sqrt{\frac{3}{5\pi}}\sin(2\alpha)\cos(\beta) & \frac{1}{8}\sqrt{\frac{3}{5\pi}}\left(\cos(2\alpha)\left(\sin^2(\gamma)-\cos^2(\beta)\cos^2(\gamma)\right)+\sin(2\alpha)\cos(\beta)\sin(2\gamma)\right)\end{pmatrix}$$

Matrix-form coefficients of $n^{m_{\rm g},m_{\rm e}}$ for $m_{\rm g}=-\frac{1}{2}$ and $m_{\rm e}=-\frac{1}{2}$:

$$n_{0,0}^{-\frac{1}{2},-\frac{1}{2}}=\begin{pmatrix}\frac{1}{6\sqrt{\pi}} & 0\\ 0 & \frac{1}{6\sqrt{\pi}}\end{pmatrix}$$

$$n_{1,-1}^{-\frac{1}{2},-\frac{1}{2}}=\begin{pmatrix}0 & 0\\ 0 & 0\end{pmatrix}$$

$$n_{1,0}^{-\frac{1}{2},-\frac{1}{2}}=\begin{pmatrix}0 & 0\\ 0 & 0\end{pmatrix}$$

$$n_{1,1}^{-\frac{1}{2},-\frac{1}{2}}=\begin{pmatrix}0 & 0\\ 0 & 0\end{pmatrix}$$

$$n_{2,-2}^{-\frac{1}{2},-\frac{1}{2}}=\begin{pmatrix}-\frac{\cos(\beta)\left(\cos(2\alpha)\sin(2\gamma)-\sin(2\alpha)\cos(\beta)\sin^2(\gamma)\right)+\sin(2\alpha)\cos^2(\gamma)}{2\sqrt{15\pi}} & \frac{\cos(2\alpha)\cos(\beta)}{2\sqrt{15\pi}}\\ \frac{\cos(2\alpha)\cos(\beta)}{2\sqrt{15\pi}} & \frac{\sin(2\alpha)\cos^2(\beta)\cos^2(\gamma)+\cos(2\alpha)\cos(\beta)\sin(2\gamma)-\sin(2\alpha)\sin^2(\gamma)}{2\sqrt{15\pi}}\end{pmatrix}$$

$$n_{2,-1}^{-\frac{1}{2},-\frac{1}{2}}=\begin{pmatrix}\frac{\sin(\beta)\sin(\gamma)(\sin(\alpha)\cos(\beta)\sin(\gamma)-\cos(\alpha)\cos(\gamma))}{\sqrt{15\pi}} & \frac{\cos(\alpha)\sin(\beta)}{2\sqrt{15\pi}}\\ \frac{\cos(\alpha)\sin(\beta)}{2\sqrt{15\pi}} & \frac{\sin(\beta)\cos(\gamma)(\sin(\alpha)\cos(\beta)\cos(\gamma)+\cos(\alpha)\sin(\gamma))}{\sqrt{15\pi}}\end{pmatrix}$$

$$n_{2,0}^{-\frac{1}{2},-\frac{1}{2}}=\begin{pmatrix}-\frac{-3\cos(2(\beta-\gamma))-3\cos(2(\beta+\gamma))+6\cos(2\beta)+6\cos(2\gamma)+2}{48\sqrt{5\pi}} & 0\\ 0 & -\frac{3\cos(2(\beta-\gamma))+3\cos(2(\beta+\gamma))+6\cos(2\beta)-6\cos(2\gamma)+2}{48\sqrt{5\pi}}\end{pmatrix}$$

$$n_{2,1}^{-\frac{1}{2},-\frac{1}{2}}=\begin{pmatrix}\frac{\sin(\beta)\sin(\gamma)(\cos(\alpha)\cos(\beta)\sin(\gamma)+\sin(\alpha)\cos(\gamma))}{\sqrt{15\pi}} & -\frac{\sin(\alpha)\sin(\beta)}{2\sqrt{15\pi}}\\ -\frac{\sin(\alpha)\sin(\beta)}{2\sqrt{15\pi}} & \frac{\sin(\beta)\cos(\gamma)(\cos(\alpha)\cos(\beta)\cos(\gamma)-\sin(\alpha)\sin(\gamma))}{\sqrt{15\pi}}\end{pmatrix}$$

$$n_{2,2}^{-\frac{1}{2},-\frac{1}{2}}=\begin{pmatrix}\frac{\cos(2\alpha)\left(\cos^2(\beta)\sin^2(\gamma)-\cos^2(\gamma)\right)+\sin(2\alpha)\cos(\beta)\sin(2\gamma)}{2\sqrt{15\pi}} & -\frac{\sin(2\alpha)\cos(\beta)}{2\sqrt{15\pi}}\\ -\frac{\sin(2\alpha)\cos(\beta)}{2\sqrt{15\pi}} & \frac{\cos(2\alpha)\left(\cos^2(\beta)\cos^2(\gamma)-\sin^2(\gamma)\right)-4\sin(\alpha)\cos(\alpha)\cos(\beta)\sin(\gamma)\cos(\gamma)}{2\sqrt{15\pi}}\end{pmatrix}$$

Matrix-form coefficients of $n^{m_{\rm g},m_{\rm e}}$ for $m_{\rm g}=-\frac{1}{2}$ and $m_{\rm e}=\frac{1}{2}$:

$$n_{0,0}^{-\frac{1}{2},\frac{1}{2}}=\begin{pmatrix}\frac{1}{12\sqrt{\pi}} & 0\\ 0 & \frac{1}{12\sqrt{\pi}}\end{pmatrix}$$

$$n_{1,-1}^{-\frac{1}{2},\frac{1}{2}}=\begin{pmatrix}0 & -\frac{i\sin(\alpha)\sin(\beta)}{8\sqrt{3\pi}}\\ \frac{i\sin(\alpha)\sin(\beta)}{8\sqrt{3\pi}} & 0\end{pmatrix}$$

$$n_{1,0}^{-\frac{1}{2},\frac{1}{2}}=\begin{pmatrix}0 & \frac{i\cos(\beta)}{8\sqrt{3\pi}}\\ -\frac{i\cos(\beta)}{8\sqrt{3\pi}} & 0\end{pmatrix}$$

$$n_{1,1}^{-\frac{1}{2},\frac{1}{2}}=\begin{pmatrix}0 & -\frac{i\cos(\alpha)\sin(\beta)}{8\sqrt{3\pi}}\\ \frac{i\cos(\alpha)\sin(\beta)}{8\sqrt{3\pi}} & 0\end{pmatrix}$$

$$n_{2,-2}^{-\frac{1}{2},\frac{1}{2}}=\begin{pmatrix}\frac{\cos(\beta)\left(\cos(2\alpha)\sin(2\gamma)-\sin(2\alpha)\cos(\beta)\sin^2(\gamma)\right)+\sin(2\alpha)\cos^2(\gamma)}{8\sqrt{15\pi}} & -\frac{\cos(2\alpha)\cos(\beta)}{8\sqrt{15\pi}}\\ -\frac{\cos(2\alpha)\cos(\beta)}{8\sqrt{15\pi}} & -\frac{\sin(2\alpha)\cos^2(\beta)\cos^2(\gamma)+\cos(2\alpha)\cos(\beta)\sin(2\gamma)-\sin(2\alpha)\sin^2(\gamma)}{8\sqrt{15\pi}}\end{pmatrix}$$

$$n_{2,-1}^{-\frac{1}{2},\frac{1}{2}}=\begin{pmatrix}\frac{\sin(\beta)\sin(\gamma)(\cos(\alpha)\cos(\gamma)-\sin(\alpha)\cos(\beta)\sin(\gamma))}{4\sqrt{15\pi}} & -\frac{\cos(\alpha)\sin(\beta)}{8\sqrt{15\pi}}\\ -\frac{\cos(\alpha)\sin(\beta)}{8\sqrt{15\pi}} & -\frac{\sin(\beta)\cos(\gamma)(\sin(\alpha)\cos(\beta)\cos(\gamma)+\cos(\alpha)\sin(\gamma))}{4\sqrt{15\pi}}\end{pmatrix}$$

$$n_{2,0}^{-\frac{1}{2},\frac{1}{2}}=\begin{pmatrix}\frac{-3\cos(2(\beta-\gamma))-3\cos(2(\beta+\gamma))+6\cos(2\beta)+6\cos(2\gamma)+2}{192\sqrt{5\pi}} & 0\\ 0 & \frac{3\cos(2(\beta-\gamma))+3\cos(2(\beta+\gamma))+6\cos(2\beta)-6\cos(2\gamma)+2}{192\sqrt{5\pi}}\end{pmatrix}$$

$$n_{2,1}^{-\frac{1}{2},\frac{1}{2}}=\begin{pmatrix}-\frac{\sin(\beta)\sin(\gamma)(\cos(\alpha)\cos(\beta)\sin(\gamma)+\sin(\alpha)\cos(\gamma))}{4\sqrt{15\pi}} & \frac{\sin(\alpha)\sin(\beta)}{8\sqrt{15\pi}}\\ \frac{\sin(\alpha)\sin(\beta)}{8\sqrt{15\pi}} & \frac{\sin(\beta)\cos(\gamma)(\sin(\alpha)\sin(\gamma)-\cos(\alpha)\cos(\beta)\cos(\gamma))}{4\sqrt{15\pi}}\end{pmatrix}$$

$$n_{2,2}^{-\frac{1}{2},\frac{1}{2}}=\begin{pmatrix}\frac{\cos(2\alpha)\left(\cos^2(\gamma)-\cos^2(\beta)\sin^2(\gamma)\right)-4\sin(\alpha)\cos(\alpha)\cos(\beta)\sin(\gamma)\cos(\gamma)}{8\sqrt{15\pi}} & \frac{\sin(2\alpha)\cos(\beta)}{8\sqrt{15\pi}}\\ \frac{\sin(2\alpha)\cos(\beta)}{8\sqrt{15\pi}} & \frac{\cos(2\alpha)\left(\sin^2(\gamma)-\cos^2(\beta)\cos^2(\gamma)\right)+\sin(2\alpha)\cos(\beta)\sin(2\gamma)}{8\sqrt{15\pi}}\end{pmatrix}$$

References

[1] K. Szymański, "Magnetic texture determination by means of the monochromatic circularly polarized Mössbauer spectroscopy," Nucl. Instr. Meth. Phys. Res. B **134**, 405–412 (1998).

[2] G. Baumann, *Mathematica for Theoretical Physics*, 2nd ed., Springer-Verlag New York, 2005.

[3] M. A. Morrison and G. A. Parker, "A guide to rotations in quantum mechanics," Aust. J. Phys. **40**, 465–497 (1987).

Department of Experimental Physics
Faculty of Science
Palacký University Olomouc

Summary of doctoral thesis

Nuclear resonant methods applied to inhomogeneous systems with texture

Author	Vlastimil Vrba
Supervisor	prof. RNDr. Miroslav Mašláň, CSc.
Study field	Applied Physics
Study form	full-time
Year	2019

I declare that I have written this thesis by myself using the cited sources and that the thesis has not been submitted, in whole or in part, in any previous application for an academic degree.

In Olomouc, ...
signature

Student: Vlastimil Vrba
Department of Experimental Physics
Faculty of Science
Palacký University Olomouc
Czech Republic

Supervisor: prof. RNDr. Miroslav Mašláň, CSc.
Department of Experimental Physics
Faculty of Science
Palacký University Olomouc
Czech Republic

Opponent: László Deák, Ph.D.
Institute for Particle and Nuclear Physics
Wigner Research Centre for Physics
Hungarian Academy of Sciences
Hungary

Opponent: Ing. Oldřich Schneeweiss, DrSc.
Institute of Physics of Materials
Czech Academy of Sciences
Czech Republic

Date and place of thesis defense:

.....

The doctoral thesis is available at the study department of Faculty of Science of Palacký University Olomouc, residing at the same address.

Abstract

The experimental techniques based on the nuclear resonant scattering provide a unique information on solid systems via modified energy levels of nuclei caused by their hyperfine interactions. The aim of this work is to provide a theoretical description of the nuclear resonant scattering applied to complex materials exhibiting spatial inhomogeneities of hyperfine interactions along the direction of the incident radiation. The thickness effects, polarization mixing and preferential orientations of present hyperfine fields (i.e. texture) play a crucial role in the scattering process, so a general theoretical formalism is required for a proper description and interpretation of measured data. A significant part of the work is also devoted to the texture description for thick samples measured in both the energy and the time domain. The theory was successfully applied for the analysis and interpretation of nuclear forward scattering experiments conducted on $Fe_{81}Mo_8Cu_1B_{10}$ metallic glass during the crystallization process. The work also includes a description of the developed software package.

Abstrakt

Experimentální techniky založené na jevu jaderného rezonančního rozptylu poskytují informace o pevných látkách prostřednictvím modifikovaných energetických hladin jader v důsledku hyperjemných interakcí. Cílem této práce je teoreticky popsat jaderný rezonanční rozptyl na materiálech vykazujících nehomogenní rozložení hyperjemných interakcí ve směru dopadajícího záření. Zásadní vliv na rozptyl má v tomto případě tloušťka vzorku, změny v polarizaci záření a preferenční orientace přítomných hyperjemných polí (textura). Pro správný popis a interpretaci naměřených dat je pak potřeba použít obecný teoretický formalismus zahrnující uvedené jevy. Významná část práce je vyhrazena právě popisu textury v tlustých vzorcích pro měření v energetické i časové doméně. Popsaná teorie byla úspěšně použita k interpretaci experimentů jaderného dopředného rozptylu provedených na kovovém skle o složení $Fe_{81}Mo_8Cu_1B_{10}$ v průběhu krystalizace. Součástí práce je také popis vyvíjeného softwaru.

Contents

Introduction

Experiments of nuclear resonant forward scattering can be conducted either in energy domain as the Mössbauer spectroscopy or in time domain as the nuclear forward scattering. Both techniques utilize an interaction of the electromagnetic radiation with atomic nuclei and provide a unique insight into the local electric and magnetic properties in a solid.

Iron-based metallic glasses exposed to an ion irradiation have recently been studied for their potential applications in accelerator devices. These materials may comprise spatially inhomogeneous regions, i.e. different hyperfine interactions in different parts of the system. To explore the inhomogeneities by the nuclear resonant methods, a general scattering formalism must be utilized for a proper analysis and interpretation of the measurements.

The aim of this thesis is to theoretically describe the nuclear resonant scattering in the forward direction for materials with the spatial inhomogeneities of their hyperfine interactions. The information on the inhomogeneities can be obtained from an experimentally observable violation of the rotational invariance. The described theory, based on the model of a multilayered scattering system, is applied to nuclear forward scattering experiments conducted on $Fe_{81}Mo_8Cu_1B_{10}$ metallic glass exposed to an irradiation by nitrogen ions. The differences between the measured data obtained under different geometrical arrangements of the sample allowed to identify the magnetic origin of the inhomogeneities.

The observed phenomena are strongly connected to directional preferences of hyperfine interactions, i.e. texture. This work introduces a generalized texture description for both Mössbauer spectroscopy and nuclear forward scattering. It uses spherical harmonics as an orthogonal basis for the directional distributions of electric or magnetic fields. This allows a relatively simple implementation of the texture into calculations of data in energy and time domains. The results obtained under different considerations regarding the sample thickness and the used experimental technique are directly compared.

Due to new demands on the data evaluation in the nuclear resonant methods a new software package has been developed. The software allows the computations for the homogeneous systems as well as for the multilayers, simulating the inhomogeneous systems.

1 Nuclear Resonant Methods

The experimental techniques based on the resonant absorption and emission of photons by atomic nuclei started to be developed very soon after the discovery of the Mössbauer effect [1]. Today, these techniques find a wide range of applications across many scientific fields [2]. One of the main advantages is the possibility to inspect the hyperfine splitting of nuclei energy levels in a solid. The splitting is characteristic for a given surrounding of nuclei and allows to study the interactions of the surrounding with the nuclear system. Thus, the information on the atomic valence and spin states, local structural arrangements and magnetic ordering within the studied systems can be obtained [3].

1.1 Hyperfine Interactions

The interactions of a nuclear system with its surroundings depend on the properties of given nuclei and on the local fields acting on them. Assuming the nuclei properties are known by selecting a particular nuclide the information on the energy levels is directly related to the studied surroundings described by corresponding hyperfine parameters. The theory will be demonstrated using ^{57}Fe nuclide.

A single nucleus can be treated as a quantum mechanical system of Z_n protons and N_n neutrons with a total angular momentum described by $j = 0, \frac{1}{2}, 1, \frac{3}{2}, \ldots$ and $m = -j, -j+1, \ldots, j-1, j$ quantum numbers [4,5]. Nuclei with a non-zero angular momentum also have a magnetic dipole moment [6]. The electric properties of a nucleus can be described by its total electric charge q_n and electric quadrupole moment tensor [7].

The real solid state samples are many-body systems of mutually interacting nuclei and electrons. The interactions can be described by the effective magnetic and electric fields interacting with the nuclei. The total interaction Hamiltonian $\hat{H}$ is the sum of the individual magnetic and electric contributions

$$\hat{H} = \hat{H}_\mathrm{I} + \hat{H}_\mathrm{Q} + \hat{H}_\mathrm{M}. \tag{1.1}$$

The magnetic interaction Hamiltonian $\hat{H}_\mathrm{M}$ can be described by an effective magnetic field $\vec{B}$ interacting with the magnetic dipole moment [8]. It includes the interactions with the orbital and spin angular momenta of the electrons around a nucleus, interactions with other electrons and

nuclei in the solid and also the interaction with an external magnetic field. The former plays a dominant role in magnetic materials and the corresponding magnetic field contribution is referred to as the hyperfine magnetic field $\vec{B}^{\mathrm{hf}}$ [9].

The electric interactions comprise the "monopole" interaction $\hat{H}_{\mathrm{I}}$ and quadrupole interaction $\hat{H}_{\mathrm{Q}}$. The former is related to the isomer shift parameter δ, which is widely used in chemical and materials applications where its determination allows to distinguish between compounds with different atomic valence states [10]. The latter depends on the elements of the electric field gradient (EFG) tensor described by two independent parameters, the quadrupole splitting parameter Δ and so called asymmetry parameter η [8, 9] and reflects the spatial charge distribution of electrons and atoms around a nucleus. Thus, it can be used for studying a local structural ordering.

To properly describe the absorption and emission of photons by the nuclear system the eigenvalues and eigenstates of the interaction Hamiltonian with an arbitrary EFG and $\vec{B}$ orientations in the laboratory reference frame (Fig. 1.1) can be obtained [11].

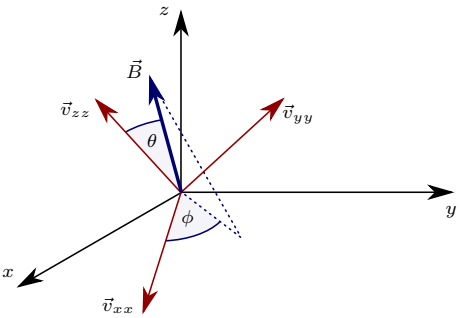

Figure 1.1: The EFG main axes given by the $\vec{v}_{xx}, \vec{v}_{yy}$ and $\vec{v}_{zz}$ vectors in the laboratory reference frame and the effective magnetic field $\vec{B}$ with angles θ and ϕ in the EFG coordinate system.

The eigenvalues of the interaction Hamiltonian provide information on the nuclear energy levels. In the absence of the hyperfine interactions the nuclear system exhibits degeneracy. Thanks to the hyperfine interactions the degeneracy is lifted and the hyperfine splitting of the nuclear energy levels occurs.

To extract the information on the hyperfine splitting, nuclear resonant methods based on the transitions between the individual nuclear energy levels have been developed. The principle of the methods is the application of an electromagnetic radiation of a proper energy. The absorption and consequent reemission of photons by nuclei is accompanied by the excitation-deexcitation of the nuclear energy levels. The Mössbauer spectroscopy and synchrotron radiation nuclear resonant scattering (NRS) methods utilize electromagnetic radiation in the 1–100 keV energy range. These energies belong to the hard X-ray and gamma radiation domain and are suitable for transitions between the ground and excited state energy levels. The transitions between the energy levels ($j_g \leftrightarrow j_e$) of ^{57}Fe nuclei exhibit an energy of 14.4 keV. The hyperfine splitting of the energy levels goes typically below 1 μeV.

The absorption and emission of photons generally proceeds with recoil. Part of the photon energy is transferred to the energy of atomic motion. As a result, the energy of the absorbed or emitted photons is not equal to the transition energy between the ground and excited states, but is shifted by the recoil energy. The information on the nuclear transition energies is then lost in the energy exchange with the lattice. New possibilities came with a recoilless absorption and emission of photons discovered by Rudolph Mössbauer in 1958. The experiment showed that absorption and emission of photons in a solid may occur without the recoil. This can be used to obtain the information on the split nuclear energy levels and the related hyperfine interactions. The relative number of recoilless events is expressed by the Lamb-Mössbauer factor f_{LM} [9].

1.2 Nuclear Resonant Scattering

The transmission Mössbauer spectroscopy (TMS) and nuclear forward scattering (NFS) methods are based on the scattering (absorption-emission) process which is coherent and elastic. Furthermore, the radiation is detected in the forward direction. The semi-classical theoretical formalism developed for the nuclear resonant coherent elastic scattering considers the solid system as a continuous optical medium described by an energy dependent index of refraction [12, 13]. The nuclear resonant contribution is given by the scattering length N, which reflects the probability amplitudes for the photons absorption and emission. The resonant

behaviour is described by Lorentzian functions $L_{n_\mathrm{g}}^{n_\mathrm{e}}(E)$ in the form

$$L_{n_\mathrm{g}}^{n_\mathrm{e}}(E) = \frac{1}{E - \Delta E_{n_\mathrm{g},n_\mathrm{e}} + i\Gamma/2}, \tag{1.2}$$

where E is the photon energy, $\Delta E_{n_\mathrm{g},n_\mathrm{e}}$ is the transition energy between the ground and excited state and Γ is the natural linewidth of the excited energy level. In the case of ^{57}Fe the magnetic dipole transition (M1) dominates [14]. A matrix formalism can be introduced to consider possible polarization changes. The scattering length is a 2×2 complex matrix, which can be written in the linear polarization basis (given by orthogonal unit vectors $\vec{\varepsilon}_\sigma$, $\vec{\varepsilon}_\pi$) as [12, 15]

$$N = \sum_{n_\mathrm{g},n_\mathrm{e}} L_{n_\mathrm{g}}^{n_\mathrm{e}}(E)\, n^{n_\mathrm{g},n_\mathrm{e}}, \tag{1.3}$$

i.e.

$$\begin{pmatrix} N_{\sigma\sigma} & N_{\sigma\pi} \\ N_{\pi\sigma} & N_{\pi\pi} \end{pmatrix} = \sum_{n_\mathrm{g},n_\mathrm{e}} L_{n_\mathrm{g}}^{n_\mathrm{e}}(E) \begin{pmatrix} n_{\sigma\sigma}^{n_\mathrm{g},n_\mathrm{e}} & n_{\sigma\pi}^{n_\mathrm{g},n_\mathrm{e}} \\ n_{\pi\sigma}^{n_\mathrm{g},n_\mathrm{e}} & n_{\pi\pi}^{n_\mathrm{g},n_\mathrm{e}} \end{pmatrix}. \tag{1.4}$$

The elements of the $n^{n_\mathrm{g},n_\mathrm{e}}$ matrices are

$$n_{\nu\mu}^{n_\mathrm{g},n_\mathrm{e}} = \sum_{M',M=-1}^{1} \left[\vec{\varepsilon}_\nu^{\,*} \cdot \vec{Y}_{M'}(\vec{k})\right] \left[\vec{Y}_M^{\,*}(\vec{k}) \cdot \vec{\varepsilon}_\mu\right] G_{M'}^{n_\mathrm{g},n_\mathrm{e}} \left(G_M^{n_\mathrm{g},n_\mathrm{e}}\right)^*, \tag{1.5}$$

where $\mu, \nu \in \{\sigma, \pi\}$ and the $G_M^{n_\mathrm{g},n_\mathrm{e}}$ factors depend on the interaction Hamiltonian eigenstates [15].

To quantitatively evaluate the rate of the multiple scattering in real solids the effective thickness d_eff is conventionally used [16]. All possible scattering paths (single scattering, double scattering, ...) including the case of no resonant interaction with the nuclear system are included in the resulting scattering matrix T, which takes the exponential form [12]

$$T = \mathrm{e}^{i\xi N}. \tag{1.6}$$

The constant ξ reflects the effective thickness of the system and for the ^{57}Fe transition it is given as

$$\xi = -\frac{\pi\Gamma d_\mathrm{eff}}{2}. \tag{1.7}$$

The application of the scattering matrix to the incident radiation field gives the transmitted radiation field in the forward direction

$$\vec{A}_{\mathrm{tr}} = T\vec{A}_{\mathrm{in}}. \tag{1.8}$$

The transmitted field can be understood as a superposition of the field $\vec{A}_{\mathrm{in}}$ (no resonant interaction with nuclei) and the scattered field [17]

$$\vec{A}_{\mathrm{tr}} = \vec{A}_{\mathrm{sc}} + \vec{A}_{\mathrm{in}}. \tag{1.9}$$

In the real samples a discrete or a continuous distribution of different nuclear sites (nuclei with different local surroundings) can occur. Each nuclear site may exhibit a different hyperfine splitting, which contributes to the resulting final form of the experimental data. The presence of more nuclear sites gives more possibilities for the interaction of photons with the nuclear system. The total scattering length is then given as a sum (or an integral) of individual partial scattering lengths. The continuous case is described by distributions of corresponding hyperfine parameters.

1.3 Coherent Elastic Forward Scattering

The information on the nuclear hyperfine splitting is coded in the scattering length N and can be potentially extracted from the measured intensities of the transmitted or the scattered radiation fields. The theoretical formalism outlined in the previous sections can be applied in both energy and time domain measurements.

1.3.1 Transmission Mössbauer Spectroscopy

The transmission Mössbauer spectroscopy utilizes a suitable radioactive material as a source of gamma photons. For example, the ^{57}Co radioactive nuclide built in a solid matrix is used as a source for excitation of ^{57}Fe energy levels.

Mössbauer transmission spectrum, measured as the transmitted radiation intensity $I_{\mathrm{tr}}(E)$, is obtained by modulating of the source emission energy and simultaneous detection of the transmitted photons. The modulation of the emission line is based on the Doppler effect, where the relative velocity v of the source is changing with respect to the measured sample [2]. The energy axis of measured spectra is conventionally displayed in the mm/s velocity units.

The density matrix formalism can be used to obtain transmission spectrum for mixed polarization states of the incident radiation [12, 13]. $I_{\mathrm{tr}}(E)$ can be written in a compact and normalised form

$$I_{\mathrm{tr}}(E) = \mathrm{Tr}\left\{T\rho T^{\dagger}\right\}, \tag{1.10}$$

where ρ is the density matrix describing the incident radiation. If the radiation is tuned to a resonance with respect to the sample transition energies then the coherent elastic nuclear resonant scattering becomes significant and the measured spectrum exhibits an intensity attenuation (see Fig. 1.2).

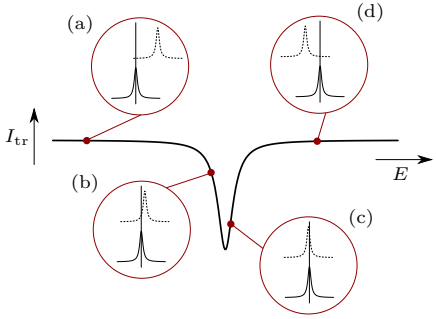

Figure 1.2: Illustration of a selected Mössbauer absorption line. The intensity of the transmitted radiation depends on the relative position of the source emission line (solid lines in the circles) with respect to a given transition energy line (dashed lines). In the resonance (b, c) there is a significant attenuation of the intensity with respect to the off-resonance case (a, d).

1.3.2 Nuclear Forward Scattering

NFS belongs to the group of experimental techniques that utilize modern synchrotron radiation sources. These sources are based on the radiation properties of charged particles accelerated to speed that approaches the speed of light [18].

In contrast to "single-line" radioactive sources the synchrotron radiation coming from the undulator exhibits a broad energy distribution of the emitted radiation. Another difference is that the synchrotron sources generate the radiation which exhibits a high degree of polarization. The radiation is linearly polarized in the plane of the accelerator storage ring (in NFS the $\vec{\varepsilon}_{\sigma}$ vector is conventionally chosen to lie in this plane, so the radiation is $\vec{\varepsilon}_{\sigma}$-polarized).

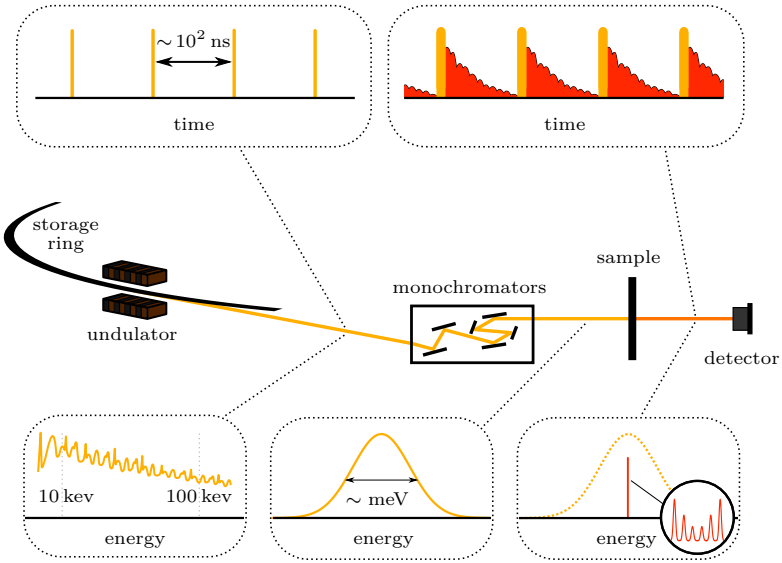

Figure 1.3: NFS experimental arrangement with the energy and time properties of the synchrotron radiation before/after monochromatization and after the scattering.

The movement of the charged particles in the storage ring can be realized in a bunch mode. The particles are grouped in several discrete bunches with a specific time separation between them (Fig. 1.3). When passing through the undulator, each bunch generates a separate synchrotron radiation pulse of $\sim$100 ps time duration. The time separation between individual pulses is usually $\sim 10^1$–10^2 ns.

The energy bandwidth of the radiation is in the meV or sub-meV range when the radiation leaves the system of monochromators. This is several orders more than the range of the nuclear transition energies. Instead of separate excitations of the individual nuclear energy levels as in the TMS, the synchrotron radiation pulses cause simultaneous coherent excitations of all the energy levels. During the subsequent deexcitation the radiation fields are emitted, with energies corresponding to differences between the individual ground and excited state energy levels. The superposition of these radiation fields gives the resulting scattered field whose intensity exhibits typical time interference patterns known as quantum beats [19].

The part of the radiation which does not interact resonantly with the nuclei leaves the scattering system in a very short time after the excitation by the radiation pulse. The time separation from the resonantly scattered part can be realized, where the time signal at the first several nanoseconds is not detected. The resulting time spectrum is given as the time dependence of the scattered radiation intensity $I_{\mathrm{sc}}(t)$. In agreement with (1.9) and (1.10) the normalised scattered radiation intensity is given by the general formula

$$I_{\mathrm{sc}}(t) = \mathrm{Tr}\left\{\mathcal{F}\left[T - \mathbf{1}\right]\rho\,\mathcal{F}^{\dagger}[T - \mathbf{1}]\right\}, \tag{1.11}$$

where $\mathcal{F}$ denotes Fourier transform [14].

In many aspects, the transmission Mössbauer spectra with absorption lines and the NFS time spectra featuring quantum beats provide equivalent information on the solid systems. The synchrotron radiation sources bring a big advantage over conventional Mössbauer sources regarding the intensity. The accumulated NFS time spectra consist of a very high number of contributions from individual synchrotron radiation pulses (coming with $\sim 10^2$ ns period). The brilliance of the synchrotron radiation [12] is significantly higher (by more than 10 orders) when compared to the radioactive sources.

The usage of synchrotron radiation has opened entirely new possibilities of hyperfine methods. An example is the use of NFS for the investigation of fast processes, including solid-state chemical reactions, structural re-ordering, diffusion or magnetic transformations [20–22]. Such studies are of a high importance from both the basic research perspective (exploring transformation kinetics and mechanisms, discovering temporary inter-phases, etc.) and the possible applications (altering transformation conditions to modify material properties). With the current radiation intensity one time spectrum could be accumulated in less than one minute.

Many efforts have also been given to the automation and fastening of the data evaluation. This becomes crucial in the NFS studies of fast processes, where one experiment may consist of hundreds of measured time spectra [23]. A sequential fitting procedure, based on connecting the neighbouring time spectra via their input and output parameter values, has been presented as a usable approach [24]. By connecting the conventional fitting software CONUSS with a specially developed

package Hubert the efficiency of the experimental data evaluation was considerably increased [25, 26].

1.3.3 Thickness Effects

The impact of the finite (effective) thickness of the scattering system on the measured Mössbauer and time spectra can be demonstrated by expanding the scattering matrix T of the system in a Taylor series

$$T = \mathrm{e}^{i\xi N} = \sum_{l=0}^{\infty} \frac{(i\xi N)^l}{l!} = \mathbf{1} + i\xi N + \frac{(i\xi N)^2}{2} + \frac{(i\xi N)^3}{6} + \dots . \quad (1.12)$$

The individual terms in the Taylor expansion correspond respectively to the non-resonant interaction, single scattering, double scattering, etc.

In TMS the transmitted intensity is given by formula (1.10), into which the expanded scattering matrix can be substituted. The intensity $I_{\mathrm{tr}}(E)$ can be expanded and divided according to the orders of the powers of ξ. The thin-sample approximation of the intensity is realized by taking only the terms up to the lowest present power of ξ, which in this case is the first order ξ^1. The second-order approximation would be realized by including the second-order terms, third-order approximation by including the third-order terms, etc. As the effective thickness increases the higher orders of $I_{\mathrm{tr}}(E)$ start to influence the Mössbauer spectrum, including the changes in the shapes and the relative amplitudes of the individual Mössbauer lines.

Thickness effects in time domain are strongly connected to the coherence of the scattering process [27]. Rather than scattering on a single nucleus the whole nuclear system is coherently excited. The following deexcitation then exhibits a speed-up effect, where the increasing effective thickness results in shorter deexcitation times. Even for the unsplit nuclear energy levels the photon emission does not follow the exponential decay with the lifetime of the excited state, as would be the case for the excitation of a single nucleus. The emission proceeds faster, the exponential time dependence is being pushed towards the lower times and exhibits beating patterns. These patterns are similar to the quantum beats, but arise from the multiple scattering and are referred to as dynamical beats. For the split energy levels the superposition of the dynamical beats with the quantum beats may occur, which results in a more complex time dependence described as the hybrid beats [28].

2 Violation of Rotational Invariance by Inhomogeneous Systems

A novel methodology for investigating the material inhomogeneities by nuclear resonant scattering techniques is presented in this chapter. The introduced approach is based on the rotational invariance and its violation, which was experimentally observed in the NFS experiments conducted for two different geometrical arrangements. Comparison of the obtained results allows to extract a unique information on the spatial distribution of nuclei featuring different hyperfine interactions, along the direction of the incident radiation.

Differences in the measured time spectra were observed upon a specific sample rotation. Similar phenomena were observed in the past within the studies of fundamental properties of scattering [13, 29], explored by ensuring well-conceived experimental conditions. This work focuses on the phenomenon of rotational invariance, whose violation was observed without any artificially introduced experimental conditions, solely as a result of the inner properties of the studied sample.

As an outcome, a simple method for identifying the presence of inhomogeneities in the bulk of a solid has been described. It is noteworthy that possibilities to experimentally observe bulk inhomogeneities of hyperfine interactions are limited [30, 31]. To the author's knowledge, such a similar observation on the real samples interpreted on the basis of rotational properties of NRS has not been reported in the literature. Despite exhibiting certain limitations regarding specific conditions imposed on the samples, the presented approach could be an inspiration for further developments. This might potentially lead to even more complex reconstruction of material inhomogeneities via an imaging technique.

2.1 Theoretical Description

2.1.1 Rotational Invariance and Homogeneous Systems

The concept of rotational invariance generally refers to situations in which the radiation intensity is not influenced by rotating the scattering system with respect to the radiation coordinate system. This work is specifically focused on the 180 ° rotation around one of the polarization axes defined by the unit vectors $\vec{\varepsilon}_\sigma$ and $\vec{\varepsilon}_\pi$ (see Fig. 2.1). We also assume

that the incident radiation is either unpolarized or fully linearly polarized along one of the polarization axes.

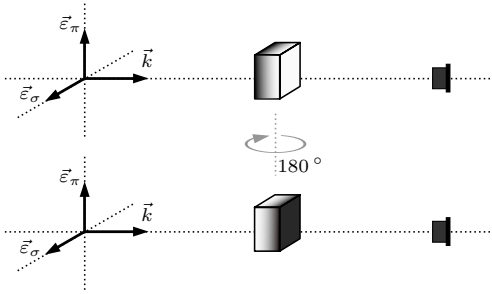

Figure 2.1: Geometrical arrangements used for the study of rotational invariance. The scattering system is rotated around one of the polarization axes (rotation around $\vec{\varepsilon}_\pi$-axis is illustrated in the figure) and experimental data obtained before and after the rotation are compared.

First, let us examine the rotational invariance for a scattering system with nuclear sites homogeneously distributed along the direction of the incident radiation. The scattering length of the system is given by formulas (1.3–1.5). The rotation of the system around the original $\vec{\varepsilon}_\pi$-axis by 180 ° transforms the scattering length N into the rotated scattering length N^{rot} according to the formula

$$N = \begin{pmatrix} N_{\sigma\sigma} & N_{\sigma\pi} \\ N_{\pi\sigma} & N_{\pi\pi} \end{pmatrix} \;\rightarrow\; N^{\mathrm{rot}} = \begin{pmatrix} N_{\sigma\sigma} & -N_{\sigma\pi} \\ -N_{\pi\sigma} & N_{\pi\pi} \end{pmatrix}. \qquad (2.1)$$

Moreover, the relation between N and N^{rot} defined by formula (2.1) holds for arbitrary powers of N and N^{rot}. Therefore, the scattering matrix T^{rot} transforms in the same way with respect to T and the 180 ° rotation changes only the sign of the off-diagonal scattering matrix elements. The identical results could be obtained for the rotation around $\vec{\varepsilon}_\sigma$-axis.

For the considered polarization states of the incident radiation the intensity of the transmitted (scattered) radiation depends only on the magnitudes of the scattering matrix elements. The changes in the phase of the off-diagonal matrix elements do not influence the intensity, which means that the rotational invariance is always satisfied for the case of

homogeneous scattering systems. Consequently, measuring the violation of rotational invariance (VRI) may potentially provide information on the system inhomogeneities. For example, it may reveal that the studied system is not fully homogeneous.

2.1.2 Scattering on Multilayers

The inhomogeneous spatial distribution of nuclear sites in a sample causes the total scattering length to be a general function of the sample depth along the radiation direction. For being able to demonstrate the role of inhomogeneities a system consisting of n separately homogeneous layers will be considered [12]. The spatial separation of the nuclear sites into individual layers described by ξ_i and N_i $(i = 1, 2, \ldots, n)$ allows to generalize the scattering matrix of the system and discuss the effects of rotation.

The construction of the scattering matrix can be demonstrated for an incident radiation $\vec{A}_{\mathrm{in}}$ in a pure polarization state. When the radiation passes through the first layer the transmitted radiation field is given as $\vec{A}_1 = T_1 \vec{A}_{\mathrm{in}}$, where $T_1 = \mathrm{e}^{i\,\xi_1 N_1}$ is the scattering matrix of the first layer. In general, each layer is described by its own scattering matrix $T_i = \mathrm{e}^{i\,\xi_i N_i}$. As the radiation $\vec{A}_1$ passes through the second layer it acts as an incident radiation on this layer and therefore $\vec{A}_2 = T_2 \vec{A}_1 = T_2 T_1 \vec{A}_{\mathrm{in}}$. The same procedure can be applied analogously for all remaining layers. After passing through the whole system, the transmitted radiation field is given as

$$\vec{A}_{\mathrm{tr}} = T_n T_{n-1} \ldots T_2 T_1 \vec{A}_{\mathrm{in}}. \tag{2.2}$$

This shows that the same theoretical description that was used for the homogeneous samples can be applied here, if the total scattering length T is taken as a multiplication of individual partial scattering matrices (Fig. 2.2).

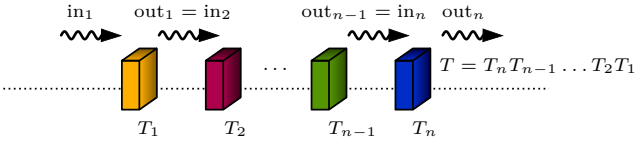

Figure 2.2: An illustration of a scattering system consisting of n layers.

Mathematically, the rotation of the multilayered system by 180 ° is equivalent to mutual interchanges of the layers followed by a separate rotation of each layer. The total scattering matrix of the rotated system takes the form

$$T^{\mathrm{rot}} = (T_n T_{n-1} \dots T_2 T_1)^{\mathrm{rot}} = T_1^{\mathrm{rot}} T_2^{\mathrm{rot}} \dots T_{n-1}^{\mathrm{rot}} T_n^{\mathrm{rot}}, \qquad (2.3)$$

where the T_i^{rot} matrices follow the same relation with respect to T_i which was given for homogeneous samples, see formula (2.1). Whether the system exhibits VRI or not depends on the relation between T and T^{rot}, which is, however, determined by relations between the scattering lengths of individual layers N_i, N_j $(i, j = 1, 2, \dots, n$ and $i \neq j)$. In this work the commutativity of the scattering lengths is chosen to analyse the properties of N_i and their connection to rotational properties of the scattering system.

We shall consider an illustrative example of a two-layered scattering system. If N_1 and N_2 satisfy the commutation relation $N_1 N_2 = N_2 N_1$ than the scattering matrices T_1 and T_2 follow the same relation, as their exponents commute. Therefore, the total scattering matrix can be written as a single exponential

$$T = \mathrm{e}^{i(\xi_1 N_1 + \xi_2 N_2)}, \qquad (2.4)$$

which is analogous to the scattering matrix of a system consisting of two homogeneously distributed nuclear sites. Furthermore, it could be found that the rotated scattering matrices T_1^{rot} and T_2^{rot} also commute and

$$T^{\mathrm{rot}} = \mathrm{e}^{i\left(\xi_1 N_1^{\mathrm{rot}} + \xi_2 N_2^{\mathrm{rot}}\right)}. \qquad (2.5)$$

The exponents in (2.4) and (2.5) differ only in the signs of their off-diagonal elements and so the same relation between T and T^{rot} as in the case of a homogeneous scattering system is obtained. Consequently, VRI cannot be observed if the individual scattering lengths mutually commute. In other words, noncommutativity of the scattering lengths is a necessary condition for VRI.

2.1.3 Texture and Multiple Scattering Effects

The physical meaning of the noncommutativity condition is closely related to rotational distributions of hyperfine parameters. For a multilayered system with all its layers exhibiting randomly oriented fields, the

scattering lengths N_i would be proportional to unit matrices. In such a case all the scattering lengths would commute and so the magnetically and electrically random layers cannot contribute to VRI. This brings up another physical condition on the scattering system, along with the inhomogeneous spatial distribution of nuclear sites. The observation of VRI is possible only if the inhomogeneous system exhibits a preferential orientation of the electric and/or magnetic field, i.e. texture.

The observation of VRI shows to be strongly related to thickness effects. This can be demonstrated using a two-layered magnetic system with specific orientations of the magnetic fields (Fig. 2.3). All the resonant nuclei in both layers, denoted as A and B, exhibit hyperfine magnetic fields of the same magnitude. The field directions for nuclei in layers A and B are given by unit vectors $\vec{m}_\mathrm{A}$ and $\vec{m}_\mathrm{B}$, respectively. Except for the field directions, the two layers are identical.

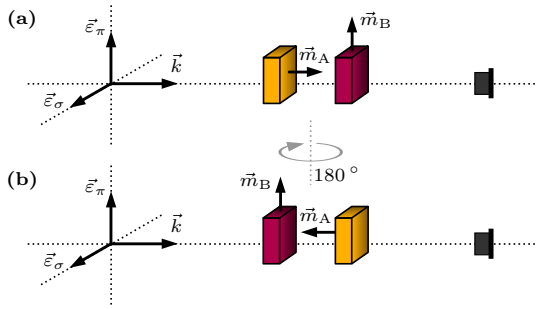

Figure 2.3: A two-layered scattering system with magnetic inhomogeneities introduced as different directions of the hyperfine magnetic field, given by unit vectors $\vec{m}_\mathrm{A}$ in layer A and $\vec{m}_\mathrm{B}$ in layer B.

The scattering lengths N_A and N_B of the layers before the rotation (Fig. 2.3a) are given as [12]

$$N_\mathrm{A} = \frac{3}{16\pi}\begin{pmatrix} F_{+1}+F_{-1} & i(F_{+1}-F_{-1}) \\ -i(F_{+1}-F_{-1}) & F_{+1}+F_{-1} \end{pmatrix}, \tag{2.6}$$

$$N_\mathrm{B} = \frac{3}{16\pi}\begin{pmatrix} 2F_0 & 0 \\ 0 & F_{+1}+F_{-1} \end{pmatrix}, \tag{2.7}$$

where

$$F_M = \sum_{m_\mathrm{g}=-j_\mathrm{g}}^{j_\mathrm{g}} \frac{C^2\,(j_\mathrm{g}1j_\mathrm{e}; m_\mathrm{g}M)}{E - \Delta E_{m_\mathrm{g},\,m_\mathrm{g}+M} + i\frac{\Gamma}{2}}\,, \quad M = -1, 0, +1\,. \tag{2.8}$$

The energy dependent F_M factors include the transition energies between the individual nuclear energy levels $\Delta E_{m_\mathrm{g},m_\mathrm{g}+M}$, the natural linewidth of the excited energy level Γ and the Clebsch-Gordan coefficients $C\,(j_\mathrm{g}1j_\mathrm{e}; m_\mathrm{g}M)$ [32].

The exponentials of N_A and N_B can be calculated analytically and the resulting scattering matrices of the layers are

$$T_\mathrm{A} = \mathrm{e}^{iK(F_{+1}+F_{-1})} \begin{pmatrix} C & -S \\ S & C \end{pmatrix}, \tag{2.9}$$

$$T_\mathrm{B} = \begin{pmatrix} \mathrm{e}^{i\,2KF_0} & 0 \\ 0 & \mathrm{e}^{iK(F_{+1}+F_{-1})} \end{pmatrix}, \tag{2.10}$$

with the constants $C = \cos\left[K(F_{+1} - F_{-1})\right]$, $S = \sin\left[K(F_{+1} - F_{-1})\right]$ and $K = (3\xi)/(16\pi)$. The total scattering matrix of the system is then

$$T = T_\mathrm{B}T_\mathrm{A} = \begin{pmatrix} C\mathrm{e}^{iK(F_{+1}+2F_0+F_{-1})} & -S\mathrm{e}^{iK(F_{+1}+2F_0+F_{-1})} \\ S\mathrm{e}^{i2K(F_{+1}+F_{-1})} & C\mathrm{e}^{i2K(F_{+1}+F_{-1})} \end{pmatrix}. \tag{2.11}$$

From the relation between rotated and non-rotated scattering lengths (and scattering matrices) given by formula (2.1), one can find out that $T_\mathrm{A}^\mathrm{rot}$ and $T_\mathrm{B}^\mathrm{rot}$ after the rotation (Fig. 2.3b) are given as a transpose of T_A and T_B, respectively. The rotated scattering matrix $T^\mathrm{rot} = T_\mathrm{A}^\mathrm{rot}\,T_\mathrm{B}^\mathrm{rot}$ is then also a transpose of T. As a result, there is a significant difference between T and T^rot which makes the measuring of VRI for such a two-layered system possible.

Fig. (2.4) shows the calculated intensities of the scattered radiation for the two-layered system. The data were simulated for fully $\vec{\varepsilon}_\sigma$-polarized incident radiation and they are presented in both the energy and the time domain. In addition to the two geometrical arrangements from Fig. 2.3 the third case representing a mixture of A and B into one homogeneous layer is shown for comparison. The parameters of α-Fe (with all nuclei being ^{57}Fe) at room temperature were used for the data simulations [33]. The intensities are compared for different total thicknesses ranging from $0.1\,\mu$m to $10\,\mu$m.

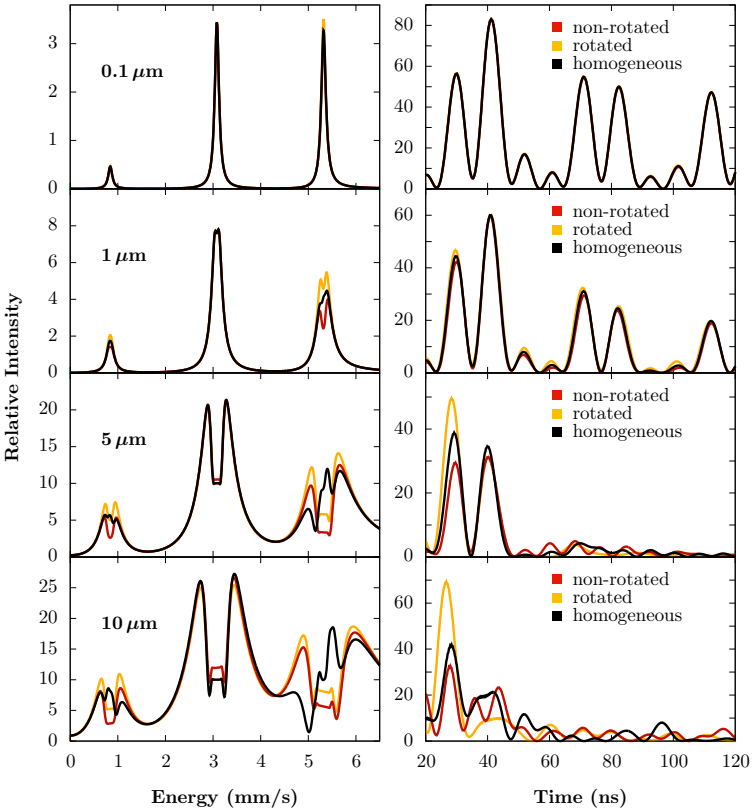

Figure 2.4: Simulated time spectra (on the right) and corresponding scattered radiation intensities in energy domain (on the left), corresponding to the three different arrangements of the considered two-layered system.

The simulations clearly demonstrate the role of thickness effects. The differences between the radiation intensities before and after the 180 ° rotation arise from the multiple-scattering terms which include the scattering on both system layers. Contributions from the single scattering or from the multiple scattering in only one of the layers are invariant under the given rotation of the system. For samples with a high effective thickness the non-invariant contributions are considerable. As the effective thickness decreases these contributions become negligible with re-

spect to the invariant ones. Consequently, those contributions to spectra which reflect the system inhomogeneities vanish in the thin-sample limit and the rotational invariance is satisfied.

2.2 Experiments of Nuclear Forward Scattering

The following part reports on the observation of VRI by NFS of synchrotron radiation. The experiments were conducted on an iron-based metallic glass, specially treated via a process of ion irradiation [34]. Investigation of such materials is of a high interest, for example, due to their possible use in radiofrequency cavities of accelerators. The knowledge on their influence by an irradiation exposure is important for a proper performance of these complex instruments. Exploring the mechanisms of the ion interactions in a solid is also interesting from the fundamental research perspective.

2.2.1 Experimental Arrangement

The composition of the studied metallic glass was $Fe_{81}Mo_8Cu_1B_{10}$ with around 50 % of the iron atoms being in the form of ^{57}Fe. The sample was prepared by a melt-spinning technique as approximately 20 μm thick and 1 mm wide ribbons [35]. The preparation conditions resulted in two physically and chemically different ribbon surfaces, also denoted as "wheel side" and "air side". The wheel side was in contact with the spinning wheel during the cooling of the melt, whereas the air side was in contact with the surrounding atmosphere [36].

The prepared ribbons in as-quenched state were irradiated by N^+ ions with the energy of 130 keV. In all the cases the sample was exposed to the N^+ ions from the air side. The experiments presented in this work were conducted on the ribbons which exhibited the ion irradiation fluency of $2.5 \cdot 10^{17}$ ions/cm^2. Despite the relatively low energy of ions the irradiation was sufficient for affecting the bulk magnetic properties of the sample [34].

The experiments were carried out at ID18 beamline in ESRF (European Synchrotron Radiation Facility). Synchrotron radiation beam with the mean energy of 14.4 keV and bandwidth of 1 meV was used. The radiation was linearly polarized in the plane of the storage ring ($\vec{\varepsilon}_\sigma$-polarized). During the NFS measurements the sample was fixed on a

stable vertical holder placed inside a vacuum furnace. For selecting the sample orientations with respect to the radiation coordinate system, distinguishing between the two sides of ribbons was important. The measurements were carried out for two orientations (air-side and wheel-side orientations) differing by the 180 ° rotation of the sample with respect to the $\vec{\varepsilon}_\pi$-axis (Fig. 2.5).

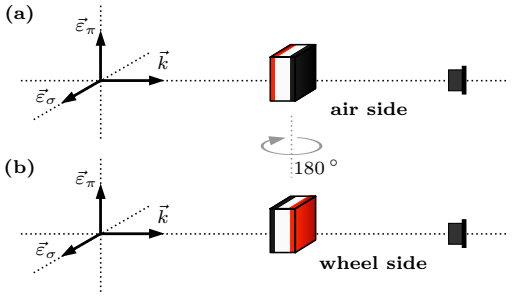

Figure 2.5: Two geometrical arrangements used for the NFS experiments. (a) Air-side orientation with the air side of the ribbon facing the detector. (b) Wheel-side orientation with the wheel side facing the detector and the air side oriented towards the incident radiation.

Each experiment consisted of three basic parts. First, one NFS time spectrum of the sample was measured for 5 minutes at room temperature, prior to any thermal treatment. After the room-temperature measurement the sample was heated within three minutes up to 300 °C. This temperature was kept for about one hour and during the isothermal annealing the time spectra were acquired for each three minutes. The sample was then spontaneously cooled to room temperature and another time spectrum was measured.

2.2.2 Identification of Magnetic Inhomogeneities

Fig. 2.6 shows the pair of time spectra measured at room temperature before the sample annealing, i.e. the time spectra measured under the same conditions for the air-side and the wheel-side orientation of the sample are compared. Both time spectra were normalized to unity area. Despite being qualitatively very similar, the time spectra exhibit

differences which are significantly higher than the uncertainties of the experimental points.

For the studied NANOPERM-type system two basic contributions to the measured time spectra can be distinguished. The first contribution originates from the original amorphous matrix, which is paramagnetic and exhibits only electric hyperfine interactions. It is typical by a broad distribution of the quadrupole splitting resulting in a distinctive doublet in the energy domain. The second contribution is given by nuclear sites in the sample which exhibit magnetic hyperfine interactions. These are connected to the formation of nanocrystalline grains in the amorphous matrix. The grains naturally take the structure and ferromagnetic ordering of α-Fe and exhibit hyperfine magnetic field of more than 30 T [26]. In addition to the crystalline magnetic phase, the ferromagnetic exchange interactions among the grains might influence the amorphous regions in the vicinity of the crystals, causing a magnetic splitting of ^{57}Fe energy levels at these regions [37]. Consequently, the magnetic contributions could be ascribed to both the crystalline and the amorphous magnetic phases in the sample.

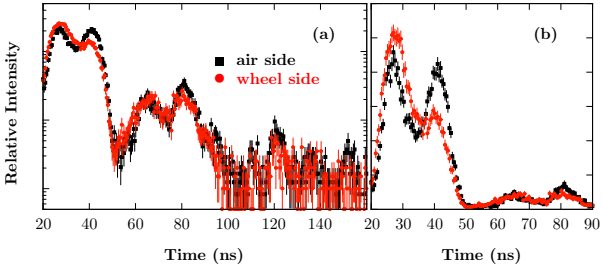

Figure 2.6: NFS time spectra of $Fe_{81}Mo_8Cu_1B_{10}$ measured at room temperature for the air-side (black squares) and the wheel-side (red-circles) orientation of the sample. The data are shown (a) on a conventional logarithmic scale in full time range and (b) on a linear scale between 20 ns and 90 ns to emphasize the measured VRI.

Although the transitions between the magnetically and electrically split energy levels could be generally coupled in the time domain into complex quantum beats, the measured time spectra of $Fe_{81}Mo_8Cu_1B_{10}$ allow to distinguish between the magnetic and the electric contributions. The electric contribution results in the "envelope" time patterns

occurring with the period of around 40 ns at room temperature, whereas the energy splitting of the magnetic contribution gives the low-periodic (high-frequency) beating with the room-temperature period of around 10–15 ns. They will be referred to as the low-frequency and the high-frequency (magnetic) quantum beats.

In Fig. 2.6 the low-frequency as well as the high-frequency quantum beats can be recognised. The magnetic part is present because of very small magnetic grains, that were formed in the sample during its preparation and could also be modified by the subsequent ion irradiation. VRI is clearly visible mainly between 20 ns and 50 ns (Fig. 2.6b) in the form of different ratios between the high-frequency quantum beats. On the basis of the theoretical analysis in section 2.1, it can be concluded that the measured metallic glass sample exhibits inhomogeneities. These inhomogeneities are of a magnetic (high-frequency) nature and can be therefore ascribed to the magnetic nuclear sites in the sample. In addition, the hyperfine magnetic field directions are not randomly distributed but exhibit texture.

Selected pairs of time spectra measured during the isothermal annealing of the sample are shown in Fig. 2.7. The time spectra measured immediately after the temperature raise to 300 °C exhibit dominantly the low-frequency contribution from the amorphous matrix (Fig. 2.7a, b). At the same time there is no significant difference between them. So the increase in temperature to 300 °C, which resulted in the suppression of high-frequency quantum beats, also caused the rotational invariance to be satisfied. This observation might be explained as a suppression of magnetic interactions in the amorphous regions which, at room temperature, were influenced by the exchange interactions among the nanocrystalline grains.

Few minutes later, new nanocrystalline grains started to form. This was accompanied by the appearance and evolution of the high-frequency quantum beats. As the new grains began to form in the sample, VRI became visible again (Fig. 2.7c, d) and further developed with time up to around 30 minutes of annealing (Fig. 2.7e, f).

The development of differences between the ratios of high-frequency quantum beats can be explained as a result of increasing amount of the crystalline magnetic phase in the sample. This is analogous to the example given in Fig. 2.4. VRI becomes more significant during the crystallization, where the amount of crystallites (and therefore the number

of ^{57}Fe nuclei that contribute to magnetic inhomogeneities) increases and enhances the role of multiple scattering. At this state, the magnetic inhomogeneities and texture can be ascribed to the newly formed nanocrystalline grains.

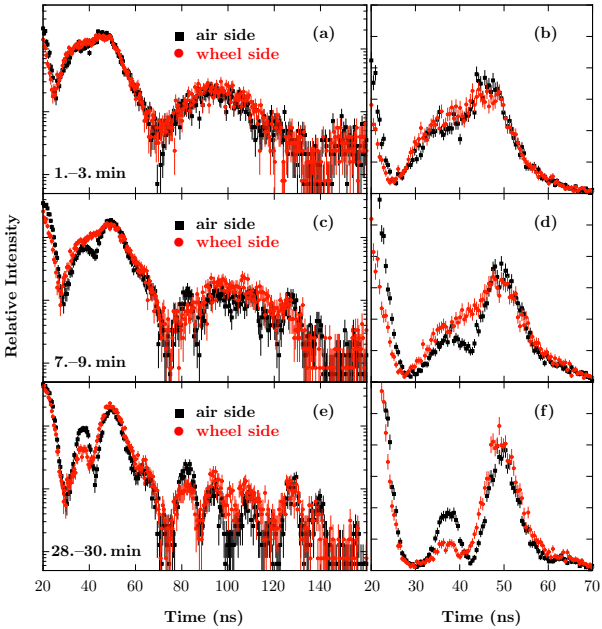

Figure 2.7: Time spectra of $Fe_{81}Mo_8Cu_1B_{10}$ measured at different times during the isothermal annealing at 300 °C. Differences in the time spectra develop and VRI becomes more significant with the increasing amount of nanocrystalline grains during the crystallization.

2.3 Discussion

The conducted experiments demonstrated a utilization of NFS for the investigation of materials exhibiting an inhomogeneous spatial distribution of hyperfine parameters. The presence of magnetic inhomogeneities along the direction of the incoming radiation was revealed in the $Fe_{81}Mo_8Cu_1B_{10}$ sample. This was achieved solely by the analysis based on considering the VRI effect. Additional information could also

be obtained by observing the evolution of VRI during the crystallization process.

To emphasize the uniqueness of the obtained information, the experimental techniques which are commonly used in solid-state studies do not allow any investigations of this type. For example, CEMS (conversion electron Mössbauer spectroscopy) can be used to obtain a surface-selective information (e.g. from the air side and the wheel side of the ribbons separately) on the hyperfine interactions. However, it allows measurements only to about 200 nm sample depths so the information on the sample volume is unavailable by this technique. On the other hand, the conventional techniques that allow to explore the bulk sample modifications (e.g. magnetization measurements) provide only an integral property over the whole measured system.

The information on the sample provided so far did not require any fitting of the time spectra. Nevertheless, for obtaining more information on the inhomogeneous regions (their thickness, hyperfine parameters, type of inhomogeneities, etc.) a detailed quantitative evaluation of the experimental data would be required. Creating such a complex fitting model solely on the basis of the conducted experiments is a challenging task. In addition to the inhomogeneities, the model would also need to reflect the time evolution of nuclear sites and their hyperfine parameters during the crystallization. Finally, a proper representation of the texture needs to be implemented for a correct evaluation of experimental data (see the following chapter). To the author's knowledge, such a general implementation of the inhomogeneities and texture has not been realized in any currently available fitting software. This implementation will be the subject of further research.

3 Texture Analysis

3.1 Introduction to Texture

Mössbauer samples may exhibit a preferential orientation of their effective electric and magnetic fields, i.e. a texture (Fig. 3.1). In other words, the directional distributions of hyperfine interactions in the solid system may deviate from the case of randomly oriented fields. Nuclear resonant scattering shows to be highly sensitive to the local fields orientations and can be used for reconstructing the information on the texture.

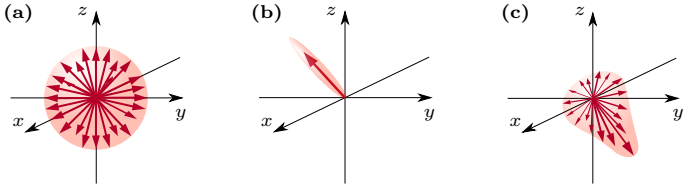

Figure 3.1: Illustration of the effective (e.g. magnetic) fields directional distributions, where more frequent orientations (more nuclei with a given magnetic field direction) are represented by bigger arrows. (a) A random case with equally distributed field directions. (b) An extreme example of the texture, where all the nuclei feel the magnetic field oriented in the same direction. (c) A general case of texture with some field directions being preferred over others.

To include the texture into the scattering formalism all the directional contributions must be included into a total scattering length

$$N = \int_{\Omega} N(\Omega)\, D(\Omega)\, \mathrm{d}\Omega, \tag{3.1}$$

where the partial scattering lengths $N(\Omega)$ from (1.3) are weighted by the distribution function $D(\Omega)$ which is called the texture function. Essentially, the main goal of the texture determination is to reconstruct the maximum possible information on the texture function.

To evaluate experimental data measured on samples with texture a parametrization of the texture function is needed. This has been treated for the special cases of (i) pure magnetic hyperfine interactions, (ii) pure axially symmetrical electric interactions or (iii) a collinear combination of the first two cases. A conventional approach is to expand the texture

function in the basis of real spherical harmonics [32]

$$D(\theta,\phi)=\sum_{l=0}^{\infty}\sum_{m=-l}^{l}D_{l,m}Y_{l,m}(\theta,\phi). \tag{3.2}$$

The angles θ, ϕ represent, for example, the direction of the effective magnetic field. The texture has been treated for TMS using the thin-sample approximation [38]. For ^{57}Fe the transmitted radiation intensity is linearly dependent on the texture coefficients $D_{l,m}$ for $l \leq 2$, but is independent of the higher-order coefficients. Consequently, only a limited information on the texture is obtainable by Mössbauer spectroscopy. A minimum texture $D_{\min}(\theta,\phi)$ defined as

$$D_{\min}(\theta,\phi)=\sum_{l=0}^{2}\sum_{m=-l}^{l}D_{l,m}Y_{l,m}(\theta,\phi) \tag{3.3}$$

is the closest experimentally available approximation of $D(\theta,\phi)$.

3.2 Scattering Formalism Applied to Texture

The scattering length $N(\theta,\phi)$ of a given nuclear site with the magnetic field orientation given by the angles θ and ϕ is described by formula (1.3). The general integral (3.1) takes the explicit form

$$N=\int_0^{2\pi}\int_0^{\pi}N(\theta,\phi)D(\theta,\phi)\sin\theta\,\mathrm{d}\theta\mathrm{d}\phi. \tag{3.4}$$

Formula (3.4) can be simplified by expanding both $N(\theta,\phi)$ and $D(\theta,\phi)$ in the real spherical harmonics basis.

The angular dependence is hidden in the $n^{m_\mathrm{g},m_\mathrm{e}}$ matrices of the scattering length as given by formulas (1.4) and (1.5). The expansion leads to the coefficients $n_{l,m}^{m_\mathrm{g},m_\mathrm{e}}$ which are also matrices. By substituting the expansions into (3.4) and using the orthogonality of real spherical harmonics the integral reduces to

$$N=\sum_{l=0}^{2}\sum_{m=-l}^{l}\sum_{m_\mathrm{g},m_\mathrm{e}}L_{m_\mathrm{g}}^{m_\mathrm{e}}(E)\,n_{l,m}^{m_\mathrm{g},m_\mathrm{e}}\,D_{l,m}. \tag{3.5}$$

The generalized scattering length N depends only on the first nine texture coefficients. Consequently, only the minimum texture (3.3) can be extracted from the nuclear resonant scattering, regardless of the applied method, the polarization of the incident radiation or the sample effective thickness. The individual experimental and sample conditions may, however, influence how much information on the texture is accessible and how sensitive the scattering/transmission is to the directional distribution of the magnetic field. This could also lead to various evaluation methods which might be suitable for different cases.

The thin-sample approximation in TMS can be obtained by expanding T in a Taylor series and restricting the intensity only to expressions which are at most linear in ξ (see section 1.3.3). The normalized transmitted radiation intensity in the first-order approximation with respect to ξ can be written using the sum of individual absorption Mössbauer lines. For the considered cases of linearly polarized and unpolarized incident radiation the sum runs only over the l values of 0 and 2. The contributions corresponding to $l = 1$ are zero. As a result the Mössbauer lines depend only on the trivial texture coefficient $D_{0,0}$ and the five texture coefficients $D_{2,-2}, D_{2,-1}, D_{2,0}, D_{2,+1}$ and $D_{2,+2}$.

Determination of the texture coefficients can be realized by evaluating the ratios of the amplitudes of the Mössbauer lines. The amplitudes are given as the values of the transmitted radiation intensities in resonances. It can be found that one measured Mössbauer spectrum provides only one independent amplitudes ratio, which is the ratio of the first and the second line amplitudes (in the ascending order of the lines resonant energies). To extract the five texture coefficients, five independent measurements for appropriate sample orientations are required.

The transmission through thick samples follows the same general formulas as in the thin-sample approximation. The expansion of the scattering matrix can be performed again. However, for a scattering system of arbitrary effective thickness the problem cannot be linearised, i.e. the exponential form of the matrix should be considered.

The first significant difference from the thin-sample approximation is that the terms containing $D_{l,m}$ with $l = 1$ are generally not zero. As a result, the amplitudes and their ratios depend on all the nine texture coefficients. In addition, the information on the texture coefficients can be extracted from two independent ratios. In contrast to the linear case, the ratio of the first and the third line amplitudes is no longer a

constant. Thus, we may obtain two independent equations from one measured spectrum. The amplitudes ratios now also depend on the effective thickness of the scattering system. Nevertheless, the effective thickness could either be taken as another variable or it could be determined in advance. Therefore, if proper orientations of the sample are selected, then the five measurements are again needed to extract the minimum texture.

With basically the same number of measurements as required for the thin-sample approximation, more information on the texture is available from the Mössbauer measurements when the thickness effects start to influence the spectra. As a drawback, the resulted dependencies on the texture coefficients are now non-linear. Selecting a suitable evaluation approach for extracting the texture coefficients for a general thickness would be an important point.

For the NFS method the synchrotron radiation is linearly polarized in the plane of the accelerator storage ring and so the incident radiation field may be written as $\vec{A}_{\mathrm{in}} = A_{\mathrm{in}}\vec{\varepsilon}_{\sigma}$. The normalised form will be considered, where $I_{\mathrm{in}} = |A_{\mathrm{in}}|^2 = 1$. The scattered radiation field and the radiation intensity in the time domain can be thus written as

$$\vec{A}_{\mathrm{sc}}(t) = \begin{pmatrix} \mathcal{F}\left[T_{\sigma\sigma} - 1\right] \\ \mathcal{F}\left[T_{\pi\sigma}\right] \end{pmatrix} A_{\mathrm{in}}, \tag{3.6}$$

$$I_{\mathrm{sc}}(t) = \vec{A}^{*}_{\mathrm{sc}}(t) \cdot \vec{A}_{\mathrm{sc}}(t) = \left|\mathcal{F}\left[T_{\sigma\sigma} - 1\right]\right|^2 + \left|\mathcal{F}\left[T_{\pi\sigma}\right]\right|^2. \tag{3.7}$$

The difference from TMS can be already seen in the thin-sample approximation. In contrast to the Mössbauer spectroscopy, where the approximated intensity was linear in ξ, a quadratic dependence is obtained in NFS. In addition, the intensity depends on the off-diagonal scattering length elements even for a thin sample. The polarization mixing in NFS is reflected in measured time spectra for arbitrary effective thickness.

The analysis showed that the situation in NFS is more similar to that of TMS applied to thick samples. The time spectrum contains information on all the nine $D_{l,m}$ coefficients. Basically, when applied to the same ideally thin scattering system, the NFS method is "more sensitive" to texture than TMS. The disadvantages are mainly the non-linearity and the necessity to extract the information in the time domain.

3.3 Concluding Remarks

Combination of the general scattering formalism with the texture description, using its coefficients in real spherical harmonics basis, allows to include the preferentially oriented electric or magnetic fields into a theoretical model of a scattering system. The results, as given in the previous sections, may be implemented into a software package for evaluating experimental data from energy or time domain measurements. Further efforts in selecting a suitable approach for the extraction of the texture coefficients is needed, mainly for TMS applied to thick samples and for the time-domain NFS. Major difficulties could be connected to the non-linear dependence of the Mössbauer lines and the time-domain patterns on the texture coefficients. One of the options can be the simultaneous fitting of the measured experimental data sets.

The evaluation of NFS time spectra is complicated as the information contained in the energy absorption lines is delocalised in time. Except the simultaneous fitting of time spectra the harmonic dependence encourages a Fourier analysis for the texture extraction. Recently, the application of Fourier transform to time spectra has been successfully applied in NRS studies [39, 40]. Similar procedures to those developed in TMS could be used for the $D_{l,m}$ extraction, where the ratios of the lines obtained as a Fourier picture of the time signal could be evaluated.

4 ERNST Software Package

The development of a new software ERNST (Evaluation of Resonant Nuclear Scattering in energy and Time domain) was motivated by newly emerging demands on the data analysis in the fields of TMS and NFS (including those described in chapters 2 and 3).

The software is developed in C programming language using Qt Creator development environment [41]. The C standard library and GSL (GNU Scientific Library) are used for the computation [42]. The code was written and tested on Linux operating system, but it can also be extended to Windows. ERNST works as a command line executable program. It reads the input data from an input ASCII file and, based on the chosen settings, creates an output file with the calculated data (Fig. 4.1).

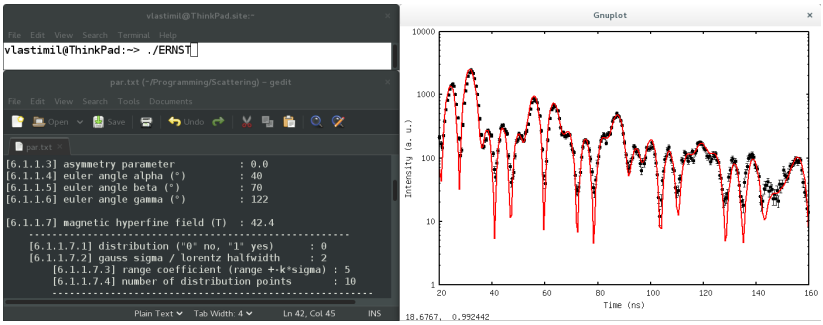

Figure 4.1: Screen of the ERNST software with a command line, an input ASCII file for setting parameters and a plot of results using the gnuplot software.

The magnetic dipole transition of ^{57}Fe nuclide is currently implemented in the software. The calculations of time and energy domain spectra are based on the theoretical formalism which was described in chapter 1. The radiation intensities $I_{\mathrm{tr}}(E)$ for TMS and $I_{\mathrm{sc}}(t)$ for TMS can be calculated. The theoretical and experimental data can be compared and visualised using the gnuplot software package [43]. The presented software package is under a continuous development as there are many topics in the nuclear resonant scattering data evaluation which deserve to be addressed.

Conclusions

This thesis presented a theoretical description of the coherent elastic nuclear resonant scattering in the forward direction applied to inhomogeneous scattering systems. The results showed that the spatial inhomogeneities along the direction of the incoming photons can be measured by nuclear resonant methods, ensuring several conditions on the studied system and the used radiation source. A method for revealing inhomogeneously distributed hyperfine interactions from two sets of measurements was introduced. It is based on the violation of rotational invariance (VRI), experimentally observed as a difference in the detected radiation intensities caused by a rotation of the sample by 180 ° around one of the radiation polarization axes.

There is a significant connection between VRI and directional distributions of hyperfine interactions within a studied system. The intensity differences can be observed only if the system exhibits a texture (either as an inner property or externally induced). This is related to the polarization effects which accompany the VRI. The observation of VRI also requires a sufficiently high effective thickness of the sample. The non-invariance under the rotation arises from the multiple scattering of photons which exhibits a non-commutative nature.

A general description of the electric or magnetic texture was described in this work. The transmission Mössbauer spectra and NFS time spectra can be calculated for an arbitrary texture function, parametrized using the texture coefficients in the spherical harmonics basis. Regardless of the used method or the sample approximation the nuclear resonant scattering utilizing the ^{57}Fe magnetic dipole transition is affected only by the texture coefficients $D_{l,m}$ with $l \leq 2$. The amount of available information on the texture and the applicable evaluation procedures depend on the used method, the incident radiation polarization and the sample thickness.

The ERNST software package has been developed for treating both energy domain TMS and time domain NFS experiments. The theoretical data can be computed and compared to the measured spectra. More advanced procedures are gradually implemented into the software in order to react to increasing demands on the NRS evaluation.

Shrnutí v českém jazyce

V dizertační práci je teoreticky popsán koherentní elastický jaderný rezonanční rozptyl v dopředném směru a jeho využití ke studiu nehomogenních materiálů. Dosažené výsledky ukazují, že při splnění podmínek týkajících se studovaného systému a použitého záření lze jaderné rezonanční metody využít k měření nehomogenního rozložení hyperjemných interakcí ve směru dopadajícího záření. V práci je představena metoda pro určení přítomnosti nehomogenit ve vzorku. Tato metoda je založena na porušení rotační invariance, jenž lze experimentálně pozorovat jako rozdíl v intenzitě detekovaného záření při rotaci vzorku o 180 ° kolem polarizační osy záření.

Porušení rotační invariance úzce souvisí se směrovými vlastnostmi hyperjemných interakcí. Pozorování tohoto jevu je možné pouze, pokud studovaný systém vykazuje preferenční orientace lokálních magnetických či elektrických polí, tj. texturu. V takovém případě je pozorovaný rozdíl doprovázen změnou polarizace záření. Další podmínkou pro pozorování porušení rotační invariance je dostatečně velká efektivní tloušťka vzorku. Invariance přestává být splněna v důsledku mnohonásobného rozptylu fotonů, jenž vykazuje nekomutativní chování.

Práce dále obsahuje obecný popis textury v jaderných rezonančních metodách. Parametrizace texturní funkce pomocí reálných sférických harmonických funkcí umožňuje výpočet transmisních Mössbauerovských spekter i časových spekter jaderného dopředného rozptylu. V případě rezonančního rozptylu na jádrech ^{57}Fe lze získat informaci o texturních koeficientech $D_{l,m}$ pouze pro $l \leq 2$, a to nezávisle na použité experimentální metodě nebo aproximaci tloušťky studovaného vzorku. Použitá metoda, vlastnosti dopadajícího záření a tloušťka vzorku nicméně ovlivňují množství informace, jenž lze o textuře získat a vhodný postup vyhodnocení naměřených dat.

Pro efektivní analýzu experimentálních dat byl vyvinut softwarový balíček ERNST, který umožňuje provádět výpočty jak pro Mössbauerovu spektroskopii v energetické doméně, tak i pro jaderný dopředný rozptyl v časové doméně. Software umožňuje výpočet teoretických spekter a jejich srovnání s naměřenými daty.

References

[1] U. Gonser, *Mössbauer Spectroscopy*, Springer-Verlag Berlin Heidelberg, 1975.

[2] P. Gütlich, E. Bill and A. X. Trautwein, *Mössbauer Spectroscopy and Transition Metal Chemistry*, Springer-Verlag Berlin Heidelberg, 2011.

[3] P. Gütlich, "Fifty years of Mössbauer spectroscopy in solid state research - remarkable achievements, future perspectives," Z. Anorg. Allg. Chem. **638**, 15–43 (2012).

[4] J. J. Sakurai, *Modern Quantum Mechanics*, Rev. ed., Addison Wesley, 1994.

[5] W. N. Cottingham and D. A. Greenwood, *An Introduction to Nuclear Physics*, 2nd ed., Cambridge University Press, 2001.

[6] D. Craik, *Magnetism: Principles and Applications*, Wiley, 1995.

[7] B. Sedlák and R. N. Kuz'min, *Jaderné Resonanční Metody ve Fyzice Pevných Látek*, Praha: SPN, 1978.

[8] C. J. Voyer and D. H. Ryan, "A complete solution to the Mössbauer problem, all in one place," Hyperfine Interact. **170**, 91–104 (2006).

[9] N. N. Greenwood and T. C. Gibb, *Mössbauer Spectroscopy*, Chapman & Hall, 1971.

[10] P. Novak, M. Kolar, L. Machala, K. M. Siskova, F. Karlicky, M. Petr and R. Zboril, "Transformations of ferrates(IV,V,VI) in liquids: Mössbauer spectroscopy of frozen solutions," Phys. Chem. Chem. Phys. **20**, 30247–30256 (2018).

[11] M. A. Morrison and G. A. Parker, "A guide to rotations in quantum mechanics," Aust. J. Phys. **40**, 465–497 (1987).

[12] R. Röhlsberger, *Nuclear Condensed Matter Physics with Synchrotron Radiation: Basic Principles, Methodology and Applications*, Springer-Verlag Berlin Heidelberg, 2004.

[13] M. Blume and O. C. Kistner, "Resonant absorption in the presence of Faraday rotation," Phys. Rev. **171**, 417–425 (1968).

[14] W. Sturhahn, E. Gerdau, "Evaluation of time-differential measurements of nuclear-resonance scattering of x rays," Phys. Rev. B **49**, 9285–9294 (1994).

[15] J. P. Hannon and G. T. Trammell, "Coherent γ-ray optics," Hyperfine Interact. **123/124**, 127–274 (1999).

[16] C. L'abbé, R. Callens and J. Odeurs, "Time-integrated synchrotron Mössbauer spectroscopy," Hyperfine Interact. 135, 275–294 (2001).

[17] I. Serdons, "Application of stroboscopic detection of nuclear forward scattered synchrotron radiation," Ph.D. thesis, Katholieke Universiteit Leuven, 2005.

[18] H. Wiedemann, *Particle Accelerator Physics*, 3rd ed., Springer-Verlag Berlin Heidelberg, 2007.

[19] G. T. Trammell and J. P. Hannon, "Quantum beats from nuclei excited by synchrotron pulses," Phys. Rev. B **18**, 165–172 (1978).

[20] G. Vogl and B. Sepiol, "Diffusion in crystalline materials," Hyperfine Interact. **123/124**, 595–609 (1999).

[21] M. Miglierini, M. Pavlovič, V. Procházka, T. Hatala, G. Schumacher and R. Rüffer, "Evolution of structure and local magnetic fields during crystallization of HITPERM glassy alloys studied by *in situ* diffraction and nuclear forward scattering of synchrotron radiation," Phys. Chem. Chem. Phys. **17**, 28239–28249 (2015).

[22] L. Machala, V. Procházka, M. Miglierini, V. K. Sharma, Z. Marušák, H. C. Wille and R. Zbořil, "Direct evidence of Fe(v) and Fe(iv) intermediates during reduction of Fe(vi) to Fe(iii): a nuclear forward scattering of synchrotron radiation approach," Phys. Chem. Chem. Phys. **17**, 21787–21790 (2015).

[23] M. Miglierini, V. Prochazka, S. Stankov, P. Svec, Sr., M. Zajac, J. Kohout, A. Lancok, D. Janickovic and P. Svec, "Crystallization kinetics of nanocrystalline alloys revealed by *in situ* nuclear forward scattering of synchrotron radiation," Phys. Rev. B **86**, 020202 (2012).

[24] V. Vrba, V. Procházka, D. Smrčka and M. Miglierini, "Advanced approach to the analysis of a series of *in-situ* nuclear forward scattering experiments," Nucl. Instr. Meth. Phys. Res. B **847**, 111-116 (2017).

[25] V. Vrba, V. Procházka, D. Smrčka and M. Miglierini, "Hubert: Software for efficient analysis of in-situ nuclear forward scattering experiments," AIP Conf. Proc. **1781**, 020013 (2016).

[26] V. Procházka, V. Vrba, D. Smrčka, R. Rüffer, P. Matúš, M. Mašláň and M. Miglierini, "Structural transformation of NANOPERM-type metallic glasses followed *in situ* by synchrotron radiation during thermal annealing in external magnetic field," J. Alloy. Compd. **638**, 398–404 (2015).

[27] G. V. Smirnov, "General properties of nuclear resonant scattering," Hyperfine Interact. **123/124**, 31–77 (1999).

[28] Yu. V. Shvyd'ko, U. van Bürck, W. Potzel, P. Schindelmann, E. Gerdau, O. Leupold, J. Metge, H. D. Rüter and G. V. Smirnov, "Hybrid beat in nuclear forward scattering of synchrotron radiation," Phys. Rev. B **57**, 3552–3561 (1998).

[29] L. Deák, L. Bottyán, T. Fülöp, G. Kertész, D. L. Nagy, R. Rüffer, H. Spiering, F. Tanczikó and G. Vankó, "Switching reciprocity on and off in a magneto-optical X-ray scattering experiment using nuclear resonance of α-^{57}Fe foils," Phys. Rev. Lett. **109**, 237402 (2012).

[30] U. Atzmony, S. J. Norton, L. J. Swartzendruber and L. H. Bennet, "Mössbauer imaging: experimental result," Nature **330**, 153–154 (1987).

[31] J. D. Cashion, P. S. Weiser, A. C. McGrath, R. J. Pollard and T. F. Smith, "Imaging Mössbauer spectroscopy - a new technique for materials analysis," Hyperfine Interact. **58**, 2507–2512 (1990).

[32] M. E. Rose, *Elementary Theory of Angular Momentum*, Wiley, 1957.

[33] U. Bergmann, S. D. Shastri, D. P. Siddons, B. W. Batterman and J. B. Hastings, "Temperature dependence of nuclear forward scattering of synchrotron radiation in α-^{57}Fe," Phys. Rev. B **50**, 5957–5961 (1994).

[34] M. Miglierini and M. Hasiak, "Ion irradiation induced structural modifications of $Fe_{81}Mo_8Cu_1B_{10}$," Phys. Status Solidi A **213**, 1138–1144 (2016).

[35] M. Miglierini, V. Procházka, **V. Vrba**, P. Švec, D. Janičkovič and P. Matúš, "Methods of *ex situ* and *in situ* investigations of structural transformations: The case of crystallization of metallic glasses," J. Vis. Exp. **136**, e57657 (2018).

[36] M. Hasiak and M. Miglierini, "Impact of ion-irradiation upon microstructure and magnetic properties of NANOPERM-type $Fe_{81}Mo_8Cu_1B_{10}$ metallic glass," Acta Phys. Pol. A **133**, 680–683 (2018).

[37] M. Miglierini and J. M. Greneche, "Mössbauer spectrometry of Fe(Cu)MB-type nanocrystalline alloys: II. The topography of hyperfine interactions in Fe(Cu)ZrB alloys," J. Phys.: Condens. Matter **9**, 2321–2347 (1997).

[38] H.-D. Pfannes and H. Fischer, "The texture problem in Mössbauer spectroscopy," Appl. Phys. **13**, 317–325 (1977).

[39] R. Röhlsberger, J. Bansmann, V. Senz, K. L. Jonas, A. Bettac, K. H. Meiwes-Broer and O. Leupold, "Nanoscale magnetism probed by nuclear resonant scattering of synchrotron radiation," Phys. Rev. B **67**, 245412 (2003). R. Röhlsberger, J. Bansmann, V. Senz, K. L. Jonas, A. Bettac, K. H. Meiwes-Broer and O. Leupold, "Publisher's note: Nanoscale magnetism probed by nuclear resonant scattering of synchrotron radiation," Phys. Rev. B **68**, 049901(E) (2003).

[40] A. I. Rykov, I. A. Rykov, K. Nomura and X. Zhang, "Frequency spectra of quantum beats in nuclear forward scattering of ^{57}Fe: The Mössbauer spectroscopy with superior energy resolution," Hyperfine Interact. **163**, 29–56 (2005).

[41] "Qt," [online], [visited on 2019-06-10], Available from: https://doc.qt.io/qtcreator/index.html

[42] "GSL - GNU Scientific Library," [online], [visited on 2019-06-08], Available from: https://www.gnu.org/software/gsl/doc/html/index.html

[43] "Gnuplot," [online], [visited on 2019-06-08], Available from: http://www.gnuplot.info/

List of Publications

[I] V. Procházka, **V. Vrba**, D. Smrčka, R. Rüffer, P. Matúš, M. Mašláň and M. Miglierini, "Structural transformation of NANOPERM-type metallic glasses followed *in situ* by synchrotron radiation during thermal annealing in external magnetic field," J. Alloy. Compd. **638**, 398–404 (2015).

[II] **V. Vrba**, V. Procházka, D. Smrčka and M. Miglierini, "Hubert: Software for efficient analysis of in-situ nuclear forward scattering experiments," AIP Conf. Proc. **1781**, 020013 (2016).

[III] V. Procházka, **V. Vrba**, P. Šretrová, D. Smrčka and M. Miglierini, "Preferential magnetic orientation in amorphous alloys determined by NFS and Mössbauer spectroscopy," AIP Conf. Proc. **1781**, 020014 (2016).

[IV] D. Smrčka, V. Procházka, P. Novák, J. Kašlík and **V. Vrba**, "Iron oxalate decomposition process by means of Mössbauer spectroscopy and nuclear forward scattering," AIP Conf. Proc. **1781**, 020012 (2016).

[V] P. Novák, J. Pechoušek, V. Procházka, J. Navařík, L. Kouřil, P. Kohout, **V. Vrba** and L. Machala, "Time differential ^{57}Fe Mössbauer spectrometer with unique 4π YAP:Ce 122.06 keV gamma-photon detector," Nucl. Instr. Meth. Phys. Res. A **832**, 292–296 (2016).

[VI] **V. Vrba**, V. Procházka, D. Smrčka and M. Miglierini, "Advanced approach to the analysis of a series of *in-situ* nuclear forward scattering experiments," Nucl. Instr. Meth. Phys. Res. A **847**, 111–116 (2017).

[VII] M. Miglierini, V. Procházka, **V. Vrba**, P. Švec, D. Janičkovič and P. Matúš, "Methods of *ex situ* and *in situ* investigations of structural transformations: The case of crystallization of metallic glasses," J. Vis. Exp. **136**, e57657 (2018).

[VIII] **V. Vrba**, V. Procházka and M. Miglierini, "Identification of spatial magnetic inhomogeneities by nuclear forward scattering of synchrotron radiation," J. Synchrotron Rad. **26** (2019), Accepted for publication.

[IX] D. Smrčka, V. Procházka, **V. Vrba** and M. Miglierini, "Nuclear forward scattering analysis of crystallization processes in weakly magnetic metallic glasses," J. Alloys Compd. **793**, 672–677 (2019).

[X] D. Smrčka, V. Procházka, **V. Vrba** and M. Miglierini, "On the formation of nanocrystalline grains in metallic glasses by means of in-situ nuclear forward scattering of synchrotron radiation," Nanomaterials **9**, 544 (2019).